

Universität Stuttgart

Germany

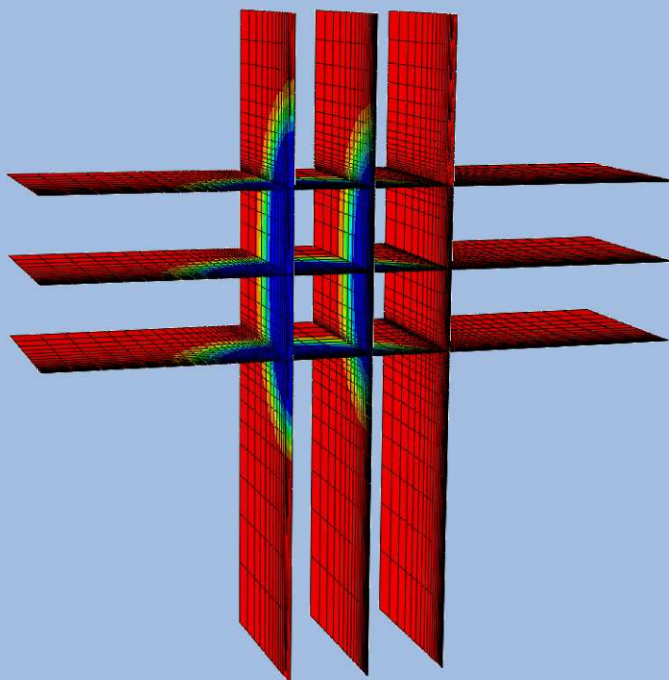
Institut für Mechanik (Bauwesen)

Lehrstuhl für Kontinuumsmechanik

Prof. Dr.-Ing. W. Ehlers

Thermomechanical Modelling of Non-isothermal Porous Materials with Application to Enhanced Geothermal Systems

David Koch



Report No.: II-31 (2016)

Thermomechanical Modelling of Non-isothermal Porous Materials with Application to Enhanced Geothermal Systems

Von der Fakultät Bau- und Umweltingenieurwissenschaften
der Universität Stuttgart zur Erlangung der Würde
eines Doktor-Ingenieurs (Dr.-Ing.)
genehmigte Abhandlung

von

Dipl.-Ing. David Koch

aus

Göppingen

Hauptberichter: Prof. Dr.-Ing. Wolfgang Ehlers

Mitberichter: apl. Prof. Dr.-Ing. Joachim Bluhm

Tag der mündlichen Prüfung: 7. November 2016

Institut für Mechanik (Bauwesen) der Universität Stuttgart

Lehrstuhl für Kontinuumsmechanik

Prof. Dr.-Ing. W. Ehlers

2016

Report No. II-31
Institut für Mechanik (Bauwesen)
Lehrstuhl für Kontinuumsmechanik
Universität Stuttgart, Germany, 2016

Editor:

Prof. Dr.-Ing. W. Ehlers

© David Koch
Institut für Mechanik (Bauwesen)
Lehrstuhl für Kontinuumsmechanik
Universität Stuttgart
Pfaffenwaldring 7
70569 Stuttgart, Germany

All rights reserved. No part of this publication may be reproduced, stored in a retrieval system, or transmitted, in any form or by any means, electronic, mechanical, photocopying, recording, scanning or otherwise, without the permission in writing of the author.

ISBN 978-3-937399-31-7
(D 93 – Dissertation, Universität Stuttgart)

Acknowledgements

The work presented in this doctoral thesis was carried out between the years 2009 and 2016 when I was a teaching assistant and a research associate at the Institute of Applied mechanics (Civil Engineering), Chair of Continuum Mechanics, University of Stuttgart, Germany. Numerous people contributed in many ways to the realisation of this work - all their support is most gratefully acknowledged. First of all, I would like to thank my supervisor and teacher, Professor Wolfgang Ehlers, for giving me the opportunity to work at his institute. This allowed me to participate in his profound knowledge in the field of continuum mechanics that forms the important foundation for this work. I am also particularly grateful to Professor Joachim Bluhm for taking the first co-chair in my dissertation procedure.

I want to thank all my fellow colleagues at the institute for the friendly atmosphere and the constant willingness to share their experiences and knowledge with me. In Particular, I am very thankful to Dr.-Ing. Arndt Wagner for the many fruitful discussions we had on various topics which often went far beyond any topics of our research, and to Maik Schenke, Sami Bidier, Kai Häberle, Patrick Schröder, Lukas Eurich, Davina Fink, Chenyi Luo, Dr.-Ing. Thomas Heidlauf and all other colleagues for the always friendly and positive atmosphere. I am grateful to Dr.-Ing. Said Jamei for his permanent and selfless willingness to support me in every situation. Our countless conversations and discussions have given me new perspectives and insights and have ultimately provided a great contribution on this work. I would also like to thank Arzu Avci, Dr.-Ing. Ayhan Acartürk, Dr.-Ing. Hans-Uwe Rempler, Dr.-Ing. Irina Komarova, Dr.-Ing. Joffrey Mabuma, Dr.-Ing. Michael Sprenger, Dr.-Ing. Nils Karajan, Dr.-Ing. Okan Avci, Dr.-Ing. Tobias Graf and Dr.-Ing. Yousef Heider. They have already left the institute before me, but have often supported me with their knowledge and experience during our time together. In addition, I would like to thank Christine Klee, Katrin Michel and Nicole Karich for their ongoing and uncomplicated support and cooperation.

My special thanks go to my wonderful parents as they have created the initial and a large part of the boundary conditions of my life, which after all led me to this point. Finally, I would like to thank the most important people in my life: my admirable wife Jessica, who always supports me, and I know that I can always rely on her even in exhausting situations, and my great children Jana, Felix and Lisa, who have been so incredibly understanding in the past few years. You make me very happy.

Stuttgart, February 2017

David Koch

*Science is more than a body of knowledge.
It's a way of thinking,
a way of sceptically interrogating the universe.*
Carl Sagan (1934 – 1996)

Contents

Deutschsprachige Zusammenfassung	III
Nomenclature	VII
1 Introduction and overview	1
1.1 Motivation	1
1.2 Scope, aims, state of the art	2
1.3 Outline of the thesis	6
2 Geothermal energy	9
2.1 The Earth as a source of energy	9
2.1.1 Structure of the Earth	9
2.1.2 Usage of geothermal energy	10
2.2 Composition and functions of enhanced geothermal systems	13
2.2.1 Preparation of boreholes and implementation of wells	14
2.2.2 Hydraulic stimulation and the creation of a geothermal reservoir	15
2.2.3 The European geothermal test site in Soultz-sous-Forêts	16
3 Theoretical fundamentals of the Theory of Porous Media	23
3.1 Homogenisation and volume fractions	23
3.2 Kinematical relations	24
3.2.1 Motion functions	24
3.2.2 Deformation and strain measures	26
3.3 External loads and stress measures	27
3.4 Balance relations	28
4 Constitutive modelling	35
4.1 Preliminary model assumptions	35
4.2 Evaluation of the entropy inequality	36
4.2.1 Thermodynamical principles	36
4.2.2 The saturation condition and the effective stress principle	38
4.2.3 Thermodynamical restrictions	39
4.3 The fluid constituent	42
4.3.1 Direct momentum production and Darcy's fluid flow	42
4.3.2 Helmholtz free energy and entropy	43

4.4	The solid constituent	44
4.4.1	Helmholtz free energy and entropy	44
4.5	Thermal conditions	46
4.5.1	Heat exchange between the solid and the fluid constituent	46
4.5.2	Heat flux	46
4.6	Balance relations of the non-isothermal biphasic model	46
4.6.1	Mass balance of the fluid	47
4.6.2	Momentum balance of the overall aggregate	47
4.6.3	Energy balance of the fluid	48
4.6.4	Energy balance of the solid	49
5	Numerical treatment	51
5.1	Finite-element method	51
5.1.1	Weak forms of the governing equations	51
5.1.2	Spatial discretisation	53
5.1.3	Temporal discretisation and solution strategy	55
5.2	Stabilisation techniques for convection dominated transport problems	56
5.2.1	Stabilisation approaches	60
6	Numerical examples	65
6.1	Material parameters and initial conditions	65
6.1.1	Fluid parameters	65
6.1.2	Solid parameters	66
6.1.3	Heat transfer between solid and fluid	67
6.2	Evaluation of the stabilisation approaches	67
6.3	Simulation of the subsurface of a geothermal power plant	72
6.3.1	Set-up of the IBVP	72
6.3.2	Results of the long-term simulation	78
7	Summary and Outlook	85
7.1	Summary	85
7.2	Outlook	86
	Bibliography	89
	Curriculum Vitae	103

Deutschsprachige Zusammenfassung

Im Laufe der letzten Jahrzehnte erfuhren die erneuerbaren Energien eine beständig wachsende Aufmerksamkeit. Diese Entwicklung wird einerseits getrieben durch die limitierte Verfügbarkeit und die Risiken der bislang primär eingesetzten fossilen Energieträger und Kernbrennstoffe und andererseits durch das große Potential der regenerativen Energieträger selbst. Neben Energie aus Wind, Sonne, Wasserkraft und Biomasse zählt auch die Geothermie zur Gruppe der erneuerbaren Energien. Im Rahmen der geothermischen Energiegewinnung wird dem Erdinneren Wärme entzogen und entweder direkt oder nach Umwandlung als elektrische Energie zur Verfügung gestellt. Abhängig von der Tiefe, aus der die Wärme entnommen wird, werden Anlagen als oberflächennahe oder als tiefe Geothermie bezeichnet. Für oberflächennahe Geothermie werden Tiefen bis wenige hundert Meter erschlossen, wohingegen bei der tiefen Geothermie die Wärme teilweise aus mehreren Kilometern Tiefe entnommen wird. Kleinere Anlagen, vor allem im oberflächennahen Bereich, werden in erster Linie zur Bereitstellung von Wärme eingesetzt. Bei den erwartungsgemäß höheren Temperaturen der tiefen Geothermie, kann auch die Umwandlung der Wärme in elektrische Energie wirtschaftlich sein. Je nach Durchlässigkeit und damit meist korrelierendem natürlichem Vorkommen an Thermalwasser lassen sich bei der tiefen Geothermie hydrothermale und petrothermale Systeme unterscheiden. Während der große Vorrat an natürlichem Thermalwasser der hydrothermalen Systeme im allgemeinen direkt entnommen werden kann, muss bei petrothermalen Systemen aufgrund der geringen Permeabilität zunächst durch hydraulische und teilweise chemische Stimulation ein entsprechendes Reservoir erschlossen werden. Das Resultat hierbei ist ein praktisch geschlossenes System, dem nun durch Injektion von Wasser durch einen Injektionsbrunnen und Entnahme des Wassers durch einen Produktionsbrunnen Wärme entzogen werden kann. Die Modellierung dieses Vorgangs der Energieentnahme ist Gegenstand der vorliegenden Arbeit, wobei der Schwerpunkt auf der Betrachtung der Temperaturentwicklung im Erdinneren liegt und dem damit einhergehenden Wärmetransport und -austausch. Die Simulation des Betriebs eines Reservoirs orientiert sich dabei an den Messungen und Ergebnissen eines Zirkulationsversuch der Forschungsanlage in Soultz-sous-Forêts.

Als mathematische Grundlage der Modellierung dient die Theorie Poröser Medien, die auf Basis eines kontinuumsmechanischen Ansatzes sehr gut geeignet ist, um thermomechanische Vorgänge in porösen Medien abzubilden (vgl. de Boer [17, 18], Bowen [22, 23, 24] und Ehlers [38, 40, 41, 42]). Ein geothermisches Reservoir stellt ein solches poröses Medium dar, wobei der Fels als poröser Festkörper von Wasser durchströmt wird. Für die Konstituierenden lassen sich ausgehend von den Axiomen der Massen-, Impuls- und Energieerhaltung Bestimmungsgleichungen aufstellen. Durch konstitutive Annahmen können die Materialeigenschaften der einzelnen Komponenten berücksichtigt werden, wobei die Grenzen der möglichen Annahmen durch die Bedingung der thermodynamischen Konsistenz vorgegeben sind. Das aus den Bestimmungsgleichungen resultierende System von partiellen Differentialgleichungen wird mit Hilfe der Finite-Elemente-Methode monolithisch gelöst. Dabei werden für die räumliche Diskretisierung Hexaederelemente verwendet

und die differential-algebraischen Gleichungen mit Hilfe des impliziten Euler-Verfahrens (Rückwärts-Euler) gelöst. Zur Implementierung und Berechnung wird hier das Programmpaket PANDAS verwendet (Ehlers & Ellsiepen [44, 45], Ellsiepen [50]).

Es zeigt sich im Verlauf der Arbeit, dass die verwendeten Materialparameter und Randbedingungen zu einer stark konvektionsdominierten Wärmeströmung im Fluid führen. Im Rahmen eines Standard-Galerkin-Verfahrens verursacht dies bekanntermaßen Oszillationen, falls die räumliche Diskretisierung, in Form des Netzes, nicht fein genug gewählt wird (Zienkiewicz *et al.* [122]). Da eine ausreichend feine Vernetzung aufgrund der geometrischen Dimensionen des gewählten Anfangsrandwertproblems nicht möglich ist, muss die Lösung numerisch stabilisiert werden. Für diese Problemstellung gibt es verschiedene Ansätze, die zum Beispiel von Donea & Huerta [32] beschrieben wurden. Im Rahmen der vorliegenden Arbeit wird die Idee der zusätzlichen Diffusion verfolgt, wobei drei Spielarten dieser Methode implementiert und verglichen werden. Jede der implementierten Stabilisierungen ist zwar in der Lage, die Oszillationen auf ein Minimum zu reduzieren, jedoch muss stets berücksichtigt werden, dass diese Glättung auf Kosten der Genauigkeit vor den im Bereich tatsächlich auftretenden größeren Gradienten geschieht. Die drei implementierten Stabilisierungsmethoden bauen aufeinander auf, und es zeigt sich, dass mit der zweiten und dritten Variante der negative Einfluss der numerischen Stabilisierung jeweils weiter reduziert werden kann.

Wie bereits erwähnt, werden für die Simulation eines tatsächlichen Reservoirs die Randbedingungen eines Zirkulationsversuchs der Geothermieanlage in Soultz-sous-Forêts verwendet. Dabei kamen je ein Injektions- und ein Produktionsbrunnen zum Einsatz. Ausgehend von einer hohen Temperatur innerhalb des Reservoirs wird durch Pumpen eine Druckdifferenz zwischen den Brunnen aufgebracht. Infolgedessen fließt kälteres Wasser vom Injektionsbrunnen in den Untergrund und strömt dort entlang des Druckgradienten zum Produktionsbrunnen, während es sich an den Kontaktflächen mit dem Fels erwärmt. Am Produktionsbrunnen verlässt das Wasser das Reservoir wieder. Aus dem Zirkulationsversuch sind der Druck an den Brunnenköpfen und die zugehörige Durchflussrate bekannt. In einer ersten Simulation wird mit dieser Information die effektive, durchschnittliche Permeabilität des Untergrunds bestimmt. Unter Verwendung des zuvor bestimmten Wertes wird anschließend das Verhalten des Reservoirs über einen Zeitraum von 50 Jahren simuliert. Da der numerische Aufwand zur Simulation des Reservoirs sehr groß ist, wird die Berechnung mit Hilfe des parallelen Löser von Abaqus durchgeführt. Um hierbei für die Berechnung der Elementsteifigkeitsmatrizen weiterhin das Programmpaket PANDAS verwenden zu können, wird dieses als Bibliothek kompiliert und über eine Schnittstelle in Abaqus eingebunden (Schenke [105], Schenke & Ehlers [106]).

In den Ergebnissen zeigt sich deutlich die Ausbreitungsfront des kälteren Wassers und wie diese nach etwa 25 Jahren, zumindest teilweise, den Produktionsbrunnen erreicht und dadurch die mittlere Entnahmetemperatur des Wassers absenkt. Als Konsequenz sinkt auch die entnommene thermische Bruttoleistung des Systems ab diesem Zeitpunkt kontinuierlich. Es wird darüber hinaus klar, dass der Wärmeübergang vom Fels auf das Wasser mit Hilfe des gewählten Ansatzes abgebildet werden kann. In den Ergebnissen weisen die Temperaturen der Konstituierenden lokal nur sehr geringe Unterschiede auf, woraus sich folgern lässt, dass die Annahme lokal gleicher Temperaturen wohl sehr ähnliche Ergeb-

nisse liefern würde. Die Randbedingungen des Beispiels wurden so gewählt, dass Wärme durch Wärmeleitung prinzipiell von der Unterseite über den Fels in das Reservoir eingetragen werden kann. Es zeigt sich jedoch in den Simulationsergebnissen, dass dieser Effekt so klein ist, dass er von anderen physikalischen Phänomenen wie der Wärmeentstehung durch Dissipation infolge Reibung zwischen Wasser und Fels überlagert wird. Durch die Berücksichtigung des Verschiebungsfeldes des Felses wird erkennbar, dass die lokalen Verzerrungen infolge der Injektion des Wassers sehr klein sind. Durch die großen Abmessungen des betrachteten Gebiets summieren sich diese Verzerrungen jedoch zu einer merklichen Anhebung am oberen Rand auf.

Gliederung der Arbeit

In **Kapitel 1** werden die Motivation, der Stand der Forschung und die Ziele der Arbeit dargelegt.

In **Kapitel 2** werden die Grundlagen beschrieben, die für das weitere Verständnis der Geothermie nötig sind. Dabei werden sowohl die thermischen Bedingungen in der Erde, als auch verschiedene Techniken, die zur Nutzung dieser Wärme angewandt werden, erläutert. Anschließend wird am Beispiel der Versuchsanlage in Soultz-sous-Forêts die Struktur eines tiefen geothermischen Kraftwerks dargestellt, wobei der Prozess der Erschließung des Reservoirs und die beteiligten Komponenten detailliert beschrieben werden.

Die kontinuumsmechanischen Grundlagen der Theorie Poröser Medien, die zur Beschreibung des geothermischen Untergrunds nötig sind, werden in **Kapitel 3** geschildert. Hierbei folgt auf die Beschreibung der kinematischen Beziehungen sowie der Verzerrungs- und Spannungsmaße, die Einführung der Massen-, Impuls-, Energie- und der Entropiebilanzen. Diese Bilanzen dienen entweder als Bestimmungsgleichungen des Modells oder, wie im Fall der Entropiebilanz, als Einschränkung für die konstitutiven Annahmen.

In **Kapitel 4** werden die konstitutiven Annahmen getroffen, die für die Charakterisierung der Konstituierenden notwendig sind. Dabei müssen stets die Einschränkungen, welche aus der Auswertung der Entropieungleichung resultieren, berücksichtigt werden. Dies führt schließlich zu einem System aus vier gekoppelten Gleichungen: der Massenbilanz des Fluids, der Impulsbilanz des Gesamttaggregats sowie den Energiebilanzen für den Festkörper und das Fluids.

Eine knappe Einführung in die verwendeten numerischen Verfahren wird in **Kapitel 5** gegeben. Dabei wird nach Umformulierung der Bestimmungsgleichungen in ihre schwachen Formen die räumliche und zeitliche Diskretisierung beschrieben. Anschließend werden verschiedene Methoden zur numerischen Stabilisierung von konvektionsgetriebenen Problemen diskutiert.

In **Kapitel 6** werden zunächst die benötigten Materialparameter aus entsprechender Literatur identifiziert. Anschließend werden die zuvor eingeführten Stabilisierungsmethoden anhand von einfachen Anfangsrandwertproblemen verglichen und die Ergebnisse ausgewertet. Schließlich wird das Verhalten eines geothermischen Reservoirs während des Betriebs simuliert, und die resultierenden Ergebnisse werden vorgestellt.

Abschließend werden in **Kapitel 7** die Vorteile und Einschränkungen des vorgestellten

Modells zusammengefasst. Außerdem werden einige Aspekte genannt, deren weitere Untersuchung von Interesse sein könnte.

Nomenclature

In this monograph, the common notation of modern tensor calculus is used, cf. Ehlers [39] and de Boer [16]. Moreover, the choice of symbols is based in particular on the established nomenclature, cf. e. g. de Boer [17] and Ehlers [40, 42].

Conventions

Kernel conventions

(\cdot)	place holder for arbitrary quantities
a, b, \dots or ϕ, ψ, \dots	scalars (zero-order tensors)
$\mathbf{a}, \mathbf{b}, \dots$ or $\boldsymbol{\phi}, \boldsymbol{\psi}, \dots$	vectors (first-order tensors)
$\mathbf{A}, \mathbf{B}, \dots$ or $\boldsymbol{\Phi}, \boldsymbol{\Psi}, \dots$	second-order tensors

Index and suffix conventions

i, j, k, \dots	indices as super- or subscripts that indicate the location of a quantity in a set
$(\cdot)_\alpha$	subscripts indicate kinematical quantities of a constituent within porous-media or mixture theories
$(\cdot)^\alpha$	superscripts indicate non-kinematical quantities of a constituent within porous-media or mixture theories
$(\cdot)_{0S}$	initial value of a quantity with respect to the referential configuration of the solid
$(\cdot)'_\alpha$	material time derivative following the motion of a constituent α with the solid and fluid constituents $\alpha = \{S, F\}$
$d(\cdot)$	differential operator
$\partial(\cdot)$	partial derivative operator
$\delta(\text{PV})$	test function of the PV
$(\bar{\text{P}}\bar{\text{V}})$	prescribed PV at the boundary Γ_D^{PV}
$(\cdot)^h$	spatially discretised quantity
$(\cdot)_n, (\cdot)_{n+1}$	temporal discretised quantity
$(\cdot)^*$	place holder for terms belonging to the fluid energy balance

List of symbols

Greek letters

Symbol	Unit	Description
α		constituent identifier in super- and subscript
α^F	[1/K]	linear thermal expansion coefficient
α_V^F	[1/K]	volumetric thermal expansion coefficient
Γ		surface of the spatial domain Ω of the IBVP
$\Gamma_D^{PV}, \Gamma_N^{PV}$		Dirichlet and Neumann boundaries for a certain PV
ϵ_{tol}		tolerance of the Newton solver
$\varepsilon, \varepsilon^\alpha$	[J/kg]	mass-specific internal energy of φ and φ^α
$\hat{\varepsilon}^\alpha$	[J/m ³ s]	volume-specific direct energy production of φ^α
$\hat{\zeta}^\alpha$	[J/K m ³ s]	volume-specific direct entropy production of φ^α
η, η^α	[J/K kg]	mass-specific entropy of φ and φ^α
$\hat{\eta}, \hat{\eta}^\alpha$	[J/K m ³ s]	volume-specific total entropy production of φ and φ^α
θ, θ^α	[K]	absolute Kelvin's temperature of φ and φ^α
ρ	[kg/m ³]	density of the overall aggregate φ
$\rho^\alpha, \rho^{\alpha R}$	[kg/m ³]	partial and material (realistic) density of φ^α
$\hat{\rho}^\alpha$	[kg/m ³ s]	volume-specific mass production of φ^α
σ, σ^α		scalar-valued supply of mechanical quantities
$\boldsymbol{\sigma}, \boldsymbol{\sigma}^\alpha$		vector-valued supply of mechanical quantities
$\sigma_\eta, \sigma_\eta^\alpha$	[J/K m ³ s]	volume-specific external entropy supply of φ and φ^α
$\boldsymbol{\tau}^\alpha$	[N/m ²]	Kirchhoff stress tensor of φ^α
$\Upsilon, \mathbf{\Upsilon}$		scalar- and vector-valued arbitrary field function
φ, φ^α		entire aggregate and particular constituent of the model
$\boldsymbol{\phi}, \boldsymbol{\phi}^\alpha$		vector-valued efflux of mechanical quantities
ϕ	[·]	scalar-valued variable
$\boldsymbol{\phi}_\eta, \boldsymbol{\phi}_\eta^\alpha$	[J/K m ² s]	entropy efflux of φ and φ^α
$\boldsymbol{\phi}_{PV}^j, \boldsymbol{\phi}_{PV}^j$	[-]	global basis functions of the PV
$\boldsymbol{\Phi}, \boldsymbol{\Phi}^\alpha$		general tensor-valued mechanical quantity
$\boldsymbol{\chi}_\alpha, \boldsymbol{\chi}_\alpha^{-1}$		motion and inverse motion functions of the constituents φ^α
ψ^α	[J/kg]	mass-specific Helmholtz free energy of φ^α
Ψ, Ψ^α	[·/m ³]	volume-specific densities of scalar mechanical quantities
$\boldsymbol{\Psi}, \boldsymbol{\Psi}^\alpha$	[·/m ³]	volume-specific densities of vectorial mechanical quantities
$\hat{\Psi}, \hat{\Psi}^\alpha$	[·/m ³]	volume-specific productions of scalar mechanical quantities
$\hat{\boldsymbol{\Psi}}, \hat{\boldsymbol{\Psi}}^\alpha$	[·/m ³]	volume-specific productions of vectorial mechanical quantities
ω	[m ² /m ³]	interfacial area per volume

Ω	spatial domain of the IBVP
Ω_e	spatial domain of a finite element

Latin letters

Symbol	Unit	Description
a_Γ	[m ²]	interfacial area between rock and water
A_{PW}	[m ²]	surface area of the PW
\mathbf{A}_α	[-]	Almansiian strain tensor of φ^α
\mathbf{B}_α	[-]	left Cauchy-Green deformation tensor of φ^α
$\mathcal{B}, \partial\mathcal{B}$		superimposed aggregate body and its surface
\mathbf{C}_α	[-]	right Cauchy-Green deformation tensor of φ^α
d	[m ² /s]	diffusivity in the 1-d convection-diffusion equation
\bar{d}	[m ² /s]	additional diffusivity in the 1-d convection-diffusion equation
\tilde{d}	[m ² /s]	scalar-valued additional diffusivity in the 3-d convection-diffusion equation
\tilde{d}_{θ^F}	[m ² /s]	scalar-valued additional diffusivity in the fluid energy balance
\mathbf{d}_α	[m/s]	diffusion velocity of φ^α
$da,$	[m ²]	actual area element
$d\mathbf{a},$	[m ²]	oriented actual area element
$d\mathbf{A}_\alpha,$	[m ²]	oriented reference area element of φ^α
$dm^\alpha,$	[kg]	local mass element of φ^α
dv, dv^α	[m ³]	actual volume element of φ and φ^α
dV_α	[m ³]	reference volume element of φ^α
$d\mathbf{x},$	[m]	actual line element
$d\mathbf{X}_\alpha,$	[m]	reference line element of φ^α
$\mathbf{d}(\mathbf{y}, \mathbf{y}')$		generalised damping vector
\mathbf{D}	[m ² /s]	diffusivity tensor in the 3-d convection-diffusion equation
$\bar{\mathbf{D}}$	[m ² /s]	additional diffusivity tensor in the 3-d convection-diffusion equation
\mathbf{D}_α	[1/s]	symmetric deformation velocity tensor of φ^α
\mathcal{D}	[J/(m ³ s)]	dissipation part of the entropy inequality
\hat{e}^α	[J/m ³ s]	volume-specific total energy production of φ^α
\mathbf{E}_α	[-]	Green-Lagrangean strain tensor of φ^α
\mathcal{E}	[Nm]	internal energy of a body \mathcal{B}
\mathbf{f}		generalised force vector
F		identifier for the fluid constituent φ^F

\mathbf{F}_α	[-]	material deformation gradient of φ^α
\mathbf{F}_S	[-]	material deformation gradient of the solid
\mathcal{F}		system of equations
$D\mathcal{F}_{n+1}^k$		global residual tangent at the current Newton step
\mathbf{g}	[m/s ²]	constant gravitation vector
\mathcal{G}_{PV}		weak formulation of a governing equation related to a PV
h	[m]	element size
\mathbf{H}^α	[W/(m K)]	heat conductivity tensor of φ^α
$H^{\alpha R}$	[W/(m K)]	scalar-valued real heat conductivity of φ^α
$\mathbf{H}^{\alpha R}$	[W/(m K)]	real heat conductivity tensor of φ^α
$\mathcal{H}^1(\Omega)$		Sobolev space
\mathbf{I}	[-]	identity tensor (second-order fundamental tensor)
J_α	[-]	Jacobian determinate of φ^α
k_θ^ε	[W/(m ³ K)]	volume-specific heat transfer coefficient
$k_\theta^{\varepsilon I}$	[W/(m ² K)]	interface heat transfer coefficient between φ^S and φ^F
$\mathbf{k}^\alpha, \mathbf{k}_V^\alpha, \mathbf{k}_{\partial V}^\alpha$	[N]	total, volume and contact force applied on φ^α
$\mathbf{k}(\mathbf{y})$		generalised stiffness vector
\mathcal{K}	[N m]	kinetic energy of a body \mathcal{B}
L	[m]	length of the 1-d BVP
\mathbf{L}_α	[1/s]	spatial velocity gradient of φ^α
\mathcal{L}	[N m/s]	external mechanical power of a body \mathcal{B}
\bar{m}	[kg/(m ² s)]	fluid mass flux over the boundary Γ_N^{pFR}
M	[kg]	mass of the overall aggregate φ
\bar{M}	[kg/s]	overall outflow of mass through the PW
\mathbf{n}	[-]	outward-oriented unit surface normal vector
n^α	[-]	volume fraction of φ^α
n^F, n^S	[-]	volume fraction of φ^F (porosity) and φ^S (solidity)
\mathcal{N}		total number of finite element nodes
\mathcal{O}		origin of a coordinate system
p	[N/m ²]	pore pressure
p^{FR}	[N/m ²]	effective pore pressure
$\hat{\mathbf{p}}^\alpha$	[N/m ³]	volume-specific direct momentum production of φ^α
P	[W]	gross power production
P^j		nodal points of the finite element mesh
\mathbf{P}^α	[N/m ²]	first Piola-Kirchhoff stress tensor of φ^α
Pe	[-]	Péclet number for the 1-d convection-diffusion equation
$\tilde{P}e$	[-]	Péclet number for the 3-d convection-diffusion equation

$\tilde{P}e_{\theta F}$	[-]	Péclet number for the fluid energy balance
\mathcal{P}^α		material points of φ^α
\bar{q}^α	[J/m ² s]	heat flux over the boundaries $\Gamma_N^{\theta^\alpha}$
$\mathbf{q}, \mathbf{q}^\alpha$	[J/m ² s]	heat influx vector (convection) of φ and φ^α
\mathcal{Q}	[N m/s]	external non-mechanical power of a body \mathcal{B}
r, r^α	[J/kg s]	mass-specific external heat supply of φ and φ^α
s	[·/s]	source term in the 1-d convection-diffusion equation
$\hat{\mathbf{s}}^\alpha$	[N/m ³]	volume-specific total momentum production of φ^α
S		identifier for the solid constituent φ^S
\mathbf{S}^α	[N/m ²]	second Piola-Kirchhoff stress tensor of φ^α
\mathcal{S}^{PV}		trial space of PV
t, t_0	[s]	actual and initial time
Δt	[s]	temporal distance between the current and the previous time
$\bar{\mathbf{t}}$	[N/m ²]	external load vector acting on the boundary $\Gamma_N^{\mathbf{u}_S}$
\mathbf{t}^α	[N/m ²]	surface traction vector on φ^α
T	[s]	final time of an evaluated time interval
$\mathbf{T}, \mathbf{T}^\alpha$	[N/m ²]	Cauchy stress tensor of φ and φ^α
\mathcal{T}^{PV}		test space of PV
\mathbf{u}_S	[m]	solid displacement
v	[m/s]	velocity in the 1-d convection-diffusion equation
\mathbf{v}	[m/s]	velocity in the 3-d convection-diffusion equation
V	[m ³]	volume of the body \mathcal{B}
\mathbf{w}_F	[m/s]	seepage velocity
\mathbf{W}_α	[1/s]	skew-symmetric spin tensor of φ^α
\mathbf{x}	[m]	actual position vector of φ^α
$\dot{\mathbf{x}}, \dot{\mathbf{x}}_\alpha$	[m/s]	velocity of the aggregate φ and the constituent φ^α
$\ddot{\mathbf{x}}, \ddot{\mathbf{x}}_\alpha$	[m/s ²]	acceleration of the aggregate φ and the constituent φ^α
$\mathbf{X}_\alpha = \mathbf{x}_{0\alpha}$	[m]	reference position vector of \mathcal{P}^α
\mathbf{y}		solution vector
\mathbf{y}^j		nodal solution vector
$\Delta \mathbf{y}_{n+1}^k$		vector of stage increments at the current Newton step

List of acronyms

Acronym	Description
1-d	one-dimensional
3-d	three-dimensional
BHT	bottom hole temperature
BVP	boundary-value problem
$C_6H_8O_7$	citric acid
CO_2	carbon dioxide
DOF	degrees of freedom
EGS	enhanced geothermal system
ESP	electric submersible pump
FEM	finite-element method
GRD	geothermal radial drilling
HF_4	fluoroboric acid
HCl	hydrochloric acid
HF	hydrofluoric acid
IAD	isotropic artificial diffusion
IBVP	initial-boundary-value problem
IW	injection well
LSP	line-shaft pump
Moho	Mohorovičić discontinuity
Na_3NTA	trisodium nitrilotriacetate
NH_4Cl	ammonium chloride
OCA	organic clay acid
ORC	Organic Rankine Cycle
PANDAS	porous media adaptive nonlinear finite element solver based on differential algebraic systems
PDE	partial differential equations
PV	primary variable
PW	production well
REV	representative element volume
SU	streamline upwind
SUPG	streamline upwind Petrov-Galerkin
TM	Theory of Mixtures
TPM	Theory of Porous Media
TVD	true vertical depth

Chapter 1:

Introduction and overview

1.1 Motivation

Reliable supply of energy has always been a fundamental prerequisite for the mankind to enhance the living conditions of the individual and the development of the whole society. At least since it was possible to use large amounts of mechanical energy provided by steam engines during the industrial revolution, it is clear that the progress of the society depends heavily on the supply of energy. From this point on, further energy sources and energy carriers were discovered and developed to satisfy the increasing demand of energy.

From year to year, the worldwide energy consumption increases such that it has almost doubled between 1973 and 2011 (International Energy Agency (IEA)[79]). In addition to wood, wind, the sun and water, which are used for hundreds of years to gain energy, mainly oil, natural gas and coal have established themselves as primary energy sources in the last century. A lot of money was also invested in the construction and operation of nuclear power plants in the recent decades. However, because the fossil fuels are limited and a sustainable disposal of the nuclear waste is still unsolved, renewable energy sources are becoming more and more important. A very promising renewable energy source is the geothermal heat. In particular, the deep geothermal energy has a great potential to carry a large part of the base load power supply in the future.

Geothermal heat is the energy stored in the Earth. One part of this energy, the so-called primordial heat, is still there since the accretion, when the Earth was created about 4.6 billion years ago. Another, nowadays significantly larger proportion is produced continuously by the radioactive decay. Near the surface, the temperature is considerably influenced by the sunlight. Nevertheless, in the depth of a few metres, the temperature remains approximately constant throughout the year. With the aid of a heat pump, this temperature difference to the outdoor temperature can be used to heat up during the winter and to cool down in the summer. Moreover, the geothermal energy can be considered inexhaustibly over any reasonable time frame. The higher temperatures of greater depths can be used to generate electricity and district heating.

To use the geothermal heat in an economical way, temperatures of at least 80 to 100 degrees Celsius are necessary. Depending on the geological conditions, the geothermal gradient, that is the change of temperature relative to the depth, has a large range from one up to hundreds degrees Celsius per hundred metres. Due to geological anomalies in some regions, a sufficiently high temperature can be already reached at a depth of only several hundred metres. These conditions are often associated with volcanism. In other areas, it is necessary to drill to a depth of several kilometres to find the sufficiently high temperature.

There are three different ways for heat recovery in high depths, namely the downhole heat

exchanger, hydrothermal systems and enhanced geothermal systems (EGS). To choose one of these options among others primarily depends on the geological conditions. A downhole heat exchanger is composed of a closed system of one or more U-tubes filled with a carrier fluid. The thermal interaction with the surroundings are restricted to the comparatively small surfaces of the tubes. Therefore, they usually cannot be operated economically in greater depths. In hydrothermal systems, water is directly extracted out of the highly permeable, water-bearing formation. Hydrothermal systems are open systems, because the flow in the reservoir is not limited by boundaries. For an enhanced geothermal system (EGS), the permeability of the low-porosity rock usually has to be increased. This is commonly done by hydraulic stimulations. To operate an EGS, at least two wells must be drilled. After stimulation and, consequently, creation of the reservoir, the cold water is pumped down through the injection well (IW) into the subsurface. It flows through the porous rock and is, thereby, heated at the contact surfaces with the hot rock. Subsequently, the heated water is delivered back to the surface through the production well (PW), where the heat energy of the water can be used directly for heating applications, or can be converted into electricity. Finally, returning the cooled water into the IW closes the loop. Although the system is supplied continuously from the lower layers with heat, the temperature of the reservoir eventually decreases and, thus, the productivity of the reservoir diminishes in the course of years. In order to make predictions about the development of a reservoir in advance, not only the properties of the water and the rock must be accurately described, but also the propagation of heat, in particular the transition of heat from the rock to the water, must be taken into account.

1.2 Scope, aims, state of the art

The process of enhancing the network of cracks within the subsurface by a massive injection of high-pressure water is known as fracking. Fracking is usually employed in order to increase the permeability of the solid rock within the subsurface of geothermal power plants. The resulting water-filled cracks have different dimensions, in length and in thickness. Thus, the subsurface consists of two components, namely the fractured rock and the water in the cracks. Driven by a pressure gradient, the water flows through the cracks. There are different mechanisms how the heat propagates within the reservoir. Depending on the temperature difference between the components and according to the second law of thermodynamics, the heat exchange takes place at the contact surfaces with the rock. Furthermore, a heterogeneous temperature distribution in each component results in a heat flow by conduction along the temperature gradient in the rock as well as in the water. Moreover, the heat is transported by the flow of water, thus, convectively. The system is further supplied with heat from deeper layers via conduction.

In order to describe the complex reality in a sufficiently detailed model, reasonable simplifications and assumptions must be made in the framework of an appropriate methodology. Basically, the model needs to be capable to describe the mechanical behaviour of the components, which is determined by the deformation of the rock due to a mechanical load, the flow velocity of the water within the cracks and the mechanical interaction between

the components. Moreover, and this is supposed to be the main focus here, the temperatures of the components are different in general and must, therefore, necessarily be considered individually. Thus, the thermo-mechanical coupling, the heat transfer based on conduction within the components, the convection because of the flow of water, and the heat exchange between the constituents have to be considered. Note that despite the high temperature far beyond 100 °C, the water always remains liquid because of the high pressure within the EGS. Therefore, there is no need to consider any gaseous phase in the model. As it was already mentioned, an increase of the pressure in the IW causes the water to flow along the pressure gradient to a PW. As the rock outside the pre-stimulated region is almost impermeable, an EGS can be considered as a quasi-closed system, where almost no additional water has to be supplied during operation. In order to operate the system economically, the flow rate must exceed a minimum value, which depends on the actual temperature of the extracted water. However, at too high flow rates, there is a risk that the reservoir cools down too fast and a long-term energy extraction is, therefore, no longer possible. Moreover, for higher flow rates a higher pressure gradient is necessary, which, in turn, demands more energy for the pumps.

As the water is pumped from the outside into the system, its basic mechanical and thermal properties can be determined in advance. However, these properties may slightly change due to different substances such as minerals and salts that dissolve in the water during the operation. Furthermore, the rock is, apart from smaller samples from the borehole, inaccessible for direct investigation. Therefore, it is necessary for a successful modelling to consider how far it is possible to determine actual conditions in the underground from indirect observations. In particular, the size and networking of the cracks are unknown, two factors which significantly determine the permeability of the reservoir. There are different approaches to draw conclusions on the permeability. The lower end of the well is usually permeable for the water over several hundred metres. By a piecewise sealing of the well, water can be pressed locally into the ground. This procedure makes it possible to draw conclusions on the permeability in the vicinity of the well dependent on the depth, by measuring the respective pressure and flow rate, see, e. g., Evans *et al.* [53]. A further possibility is the seismic observation of the subsurface during the hydraulic stimulation. When the high pressure causes new cracks in the rock, these microseismic events can be localised in the three-dimensional (3-d) space (Evans [52]). This map of newly created cracks may also be an indicator for the shape of the reservoir and, therefore, for local permeabilities. The volume of the water which is introduced during the stimulation may be considered as the starting point to make assumptions about the porosity in the reservoir. Moreover, the map of the microseismic events might be an indicator for the porosity distribution throughout the reservoir. The heat exchange between the water and the rock takes place at the interface between the components. Therefore, it is also important to have information about the local size of the interface. In case that the local size of interface is assumed to be heterogeneous, also here the map of the microseismic events could act as a suggestion. It is interesting to note that one can also use statistical approaches in order to describe the geological and parametric uncertainties of the geological subsurface, see, e. g., Refsgaard *et al.* [101] and Nowak *et al.* [93] for more details.

Since the time, when it was possible to gain geothermal energy from deeper layers, at-

tempts were made to simulate and predict the development of the reservoir due to the extraction of energy. As was described by O’Sullivan *et al.* [95], the first works on the modelling of geothermal reservoirs appeared in 1973 by Cheng & Lau [28] and Mercer Jr. & Pinder [90]. Over time, the models and the corresponding software implementation became more and more sophisticated. As an example, the software tool TOUGH2¹ allows for a flow-temperature simulation, where, in addition to water, the consideration of other components such as carbon dioxide (CO₂), tracer, radionuclides and more are as well possible. However, the majority of available models are limited to the simulation of fluid flow and heat transfer without considering the deformation of the solid skeleton, cf., e. g., Pruess [99]. Some authors, such as Arihara *et al.* [2] and Williamson [120], use double porosity models to describe fractured porous media. In some approaches, such as in Durst & Vuataz [36], chemical processes are also integrated. So far, there are only a few works, such as Lewis *et al.* [84], that consider the deformation of the solid due to the varying fluid pressure. A more detailed state of the art of the geothermal reservoir simulation is given by O’Sullivan *et al.* [95].

In order to describe the behaviour of a geothermal reservoir during the production with the postulated characteristics, it is convenient to establish the model based on a profound and reliable theory. Within this work, the Theory of Porous Media (TPM) is used that allows the consideration of the solid displacement in addition to the fluid flow and the heat propagation. The development of the TPM is briefly introduced in the following. After Biot [14] developed a rather intuitive theory of porous materials based on the consolidation theory of Terzaghi [110], Truesdell & Toupin [115] formed the modern continuum theory based on simple principles and axioms of thermodynamics. The Theory of Mixtures (TM) was finally formulated by Bowen [22] with its currently valid statements. Later, Bowen [23, 24] expanded the TM to the TPM by inventing the concept of volume fractions. In contrast to the TM, which is limited to miscible components, it is possible within the TPM to also consider immiscible constituents, which, in turn, may consist of miscible components. Thus, the TPM is particularly suitable for the description of fluid flow through deformable porous solids. Subsequently, the TPM has been expanded, primarily by de Boer [18], de Boer & Ehlers [20] and Ehlers [38, 40, 41, 42]. For more information on the history and development of the TPM, the interested reader is referred to de Boer [17] and Ehlers [43].

It is the aim of this contribution to derive a biphasic, thermodynamically consistent porous-media model, where a viscous fluid, namely water, flows through the pores of the elastic and incompressible solid skeleton, namely the rock, while both constituents are under non-isothermal conditions. On the one hand, the model is intended to be as simple as possible but, on the other hand, the properties and behaviour need to be taken into account with a sufficient precision. The continuum-mechanical model is embedded in the framework of the TPM, where the rock and the water are respectively represented by a porous solid and a pore fluid. To achieve this goal, in addition to the kinematic relationships, which directly result from the spatial configurations and their changes over

¹TOUGH2: (Earth Sciences Division, Lawrence Berkeley National Laboratory, Berkeley, USA) is a numerical simulator for non-isothermal flows of multicomponent, multiphase fluids in porous and fractured media.

time, the balances of mass, linear momentum and energy are axiomatically introduced. These balance relations build a system of partial differential equations (PDE), which must be closed by means of constitutive assumptions. The constitutive assumptions have to satisfy the constraints arising from the evaluation of the entropy inequality. It ensures the thermodynamically consistency of the formulation. Within this work, the evaluation is done according to Coleman & Noll [29]. Furthermore, the primary variables (PV) for the solution of the PDE system are considered to be the solid displacement, the pore-fluid pressure, and the fluid and solid temperatures.

To describe the materially incompressible solid, an elastic material behaviour is assumed. Due to the fact that the deformations of the solid are relatively small, it is sufficient to consider linearised stress and strain tensors. Furthermore, as it will be discussed in section 4.1, the thermal expansion of the solid constituent can be neglected within the occurring temperature ranges. The viscous fluid is also considered materially incompressible, but its density changes dependent on the temperature. Moreover, quasi-static conditions are considered, because of negligible accelerations of the constituents and of the overall aggregate. The consequences for a model resulting from the assumption of compressible constituents are described, e. g., by Bluhm [15].

The numerical implementation of the model is achieved via utilisation of the finite-element method (FEM), using the FE-Tool PANDAS², cf. Ehlers & Ellsiepen [44, 45] and Ellsiepen [50]. In the context of geothermal systems, the heat transfer via convection is usually dominant. The numerical treatment of a convection-dominant problem may lead to numerical oscillations, see Zienkiewicz *et al.* [122]. It results in the necessity of the application of a proper stabilisation technique. To overcome this issue, different techniques were implemented and their performance was investigated. Furthermore, the demands on the computing capacity at bigger problems make a parallelisation of the simulation inevitable. Therefore, according to Schenke [105] and Schenke & Ehlers [106], an interface was used to combine the material model of PANDAS and the parallel solver of Abaqus³. Using this interface, it is also even possible to carry out the PANDAS element evaluations in parallel.

In summer 2008, a geothermal power plant near Soultz-sous-Forêts in the Upper Rhine Graben (France) was put into operation, which, in contrast to all previous geothermal power plants, is not reliant on natural deposits of hot water or steam. Instead, the fractures in 5 000 metres depth were extended by hydraulic fracking, which led to a local geothermal reservoir, a big geothermal heat exchanger. The Upper Rhine Graben, in particular Soultz-sous-Forêts, is very well suited for this type of energy production due to its high geothermal gradient. With the help of the three existing 5 000 metre deep wells, it is currently possible to extract water with a temperature of about 160°C (cf. Genter *et al.* [61]). The drilling of the boreholes and the stimulation of the reservoir were accompanied by many research projects. To get information about the properties of the granite, Dezayes *et al.* [30] and Hooijkaas *et al.* [74] studied samples from one of the boreholes. They also correlated their results to logs from Ultrasonic Borehole Imager (UBI), spectral

²Porous media Adaptive Nonlinear finite-element solver based on Differential Algebraic Systems.

³Abaqus (Dassault Systèmes, Vélizy-Villacoublay, France) is a software suite for finite-element analysis and computer-aided engineering, cf. www.simulia.com.

gamma-rays, drilling parameters like the rate of penetration, caliper measurements⁴, inflow/outflow of drilling fluid and temperature measurements. The hydraulic stimulation of the reservoir has been observed with seismic instruments from the surface, as well as from the bottom of several already existing, more shallow boreholes, see, e. g., Dorbath *et al.* [34]. The arising 3-d map with the position of newly created cracks provided an idea about the geometry of the reservoir, which allowed a placement of further wells directly at the boundary of the stimulated region. After the hydraulic stimulation, chemical stimulations were performed with various acids, see, e. g., Nami *et al.* [92]. Weidler *et al.* [119] and Tischner *et al.* [112] showed that there is a significantly higher permeability for the reservoir after the hydraulic and chemical stimulation. During a six-week circulation test in autumn 2011, the power plant provided a mean electrical gross power of 500 kW_{el} and a thermal power of 8.5 MW_{th} (cf. Genter *et al.* [61]). A good overview of the project is given by the final reports for the first phase [111] and the second phase [60] for the German BMUB⁵ and the EU, respectively. Moreover, the new scientific insights were summarised in the “best practice handbook” [51].

The principal structure of the considered IBVP is based on the circulation test, which was conducted in Soultz-sous-Forêts in summer 2006. At this time, one IW and one PW was used. and, therefore, consists of one IW and one PW. Before the actual simulation of the reservoir could start, the appropriate initial conditions must be created as part of pre-computations. Therein, the consolidation of the domain as a consequence of the weight of the subsurface is calculated. Afterwards, starting from the fully saturated hot subsurface, with a pressure difference between the wells, the temperature of the injected fluid at the IW is decreased. During the course of the simulation, which covers a period of almost 50 years, the continuous cooling of the reservoir can be observed. In addition, further results are studied, such as the produced thermal power and the impact of the consideration of individual temperatures. The evaluation of the results concludes with an examination of the occurring solid displacements that result from the injection of the fluid.

1.3 Outline of the thesis

In **Chapter 2**, the necessary basics for an understanding of the geothermal energy are described. Therein the focus is firstly on the structure of the Earth. Following that, the thermal conditions are addressed and different techniques for using the geothermal energy are discussed. Afterwards, using the example of the pilot plant in Soultz-sous-Forêts, the composition of an EGS is explained, and the components and the process of installation are detailed.

Continuum-mechanical fundamentals of the TPM which are required to describe the EGS are given in **Chapter 3**. After providing the kinematical relations, strain and stress

⁴Caliper measurement is the recording of the shape, and here particularly the diameter, of the well as a function of depth.

⁵Bundesministerium für Umwelt, Naturschutz, Bau und Reaktorsicherheit (Federal Ministry for the Environment, Nature Conservation, Building and Nuclear Safety).

measures, the balances of mass, linear momentum, energy and entropy are introduced. These balance relations build the governing equations for the model or, in the case of the entropy balance, a restriction for the constitutive assumptions.

In **Chapter 4**, the constitutive assumptions required for characterising the constituents are made, where the restrictions resulting from the evaluation of the entropy inequality are strictly followed. This process leads to the final set of the four governing equations: the mass balance of the fluid, the linear momentum balance of the overall aggregate and the energy balances of the solid and the fluid.

A brief introduction of the numerical treatment is presented in **Chapter 5**. Therein, starting from the weak forms of the governing equations, the spatial and temporal discretisation strategies are described. Following this, several stabilisation methods for convection-driven problems are discussed.

In **Chapter 6**, firstly, the required material parameters are identified. Afterwards, the previously introduced stabilisation methods are firstly compared and, by means of the results found for simple initial-boundary-value problems (IBVP), their performances are examined. Eventually, the operation of an EGS with real dimensions is simulated and the upcoming results are evaluated.

Finally, in **Chapter 7**, the advantages and limitations of the presented model are summarised and a couple of aspects of feasible future work in this direction are addressed.

Chapter 2:

Geothermal energy

2.1 The Earth as a source of energy

About 4.5 billion years ago, along with the other planets of our solar system, the Earth was created by the gravity-driven compaction of the solar nebula, a mixture of gas and dust. The rising mass of the early Earth due to the massive bombardment with asteroids led to a higher gravity, and the resulting higher densities of the components caused an increasing temperature. In addition, the released kinetic energy of the asteroid alongside the radioactive decay contributed to a further warming of the Earth. As a consequence of the high temperatures, some components of the Earth melted and, as a result, they were sorted by gravity according to their respective density. Even today, a part of the existing heat in the Earth originates from that period. However, nowadays, the predominant part results from the continuous radioactive decay. Further effects, such as the tidal dissipation, playing only minor roles.

2.1.1 Structure of the Earth

There are two established reference models for the description of the internal structure of the Earth, the PREM¹, presented by Dziewonski & Anderson [37], and the IASP91 invented by Kennett & Engdahl [83]. The latter is the standard model of the International Association of Seismology and Physics of the Earth's Interior (IASPEI). Both models structure the interior of the Earth due to spatially varying propagation velocities of seismic waves. The spherical pattern is structured by discontinuities, which can be identified with jumps in velocity and by reflections. The models differ mainly in details, which will, however, not be discussed further at this point. The two most distinctive discontinuities are the core-mantle boundary between the core and the mantle, and the Mohorovičić discontinuity (Moho), which separates the mantle from the crust. Further discontinuities also divide the core into an inner and an outer, and the mantle into an upper and a lower part, see also Figure 2.1.

With an average thickness of only 35 kilometres, Earth's crust is the thinnest layer and is underlain by the mantle. With time, the tectonic plates were shifted due to the convective currents in the mantle. This is the main reason for earthquakes, mountain formation and emergence of new crust. Earth's crust can be divided into two strongly different types. The oceanic crust that is formed when tectonic plates drift apart, and the magma that rises to the surface solidifies. With about 3 g/cm^3 , the oceanic crust has a relatively high density, but, with usually five to seven kilometres height, it is rather thin. In addition to oxygen, the main components of the oceanic crust are silicon and magnesium. The

¹Preliminary Reference Earth Model.

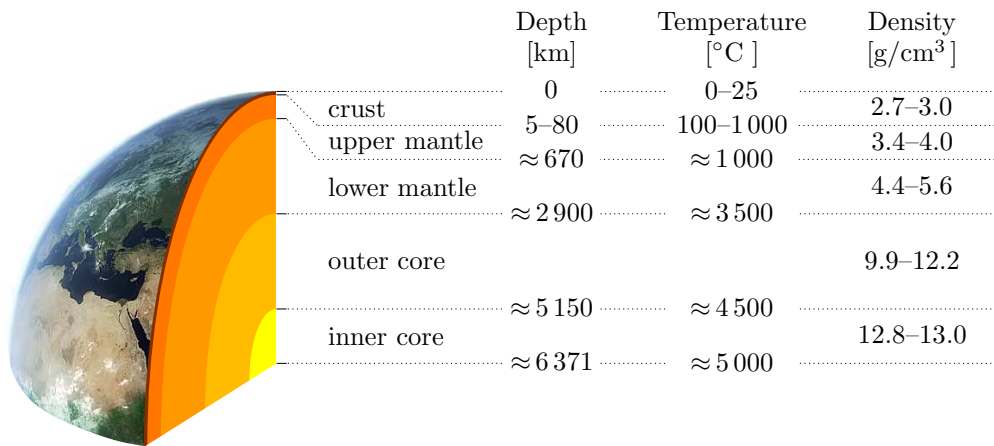


Figure 2.1: *The inner structure of the Earth.*

continental crust is formed over time, when lighter material from deeper layers rose up. This is also the reason for the relatively low density of about 2.7 g/cm^3 . Thereby, the main components are oxygen, silicon and aluminium. With a thickness of usually between 30 and 60 km, the continental crust is significantly thicker than the oceanic crust.

In contrast to the mantle, where much of the heat is transported by convection, in the crust the heat almost exclusively propagates by conduction driven by the temperature gradient corresponding to Fourier's law. The local geothermal gradient is typically measured by determining the bottom hole temperature (BHT) after borehole drilling. Although this method causes a lot of effort and high costs, it is the only way to obtain reliable data. Away from tectonic boundaries, the geothermal gradient in the upper part of the crust is about $25\text{--}30 \text{ }^\circ\text{C}$ for every kilometre. Maximum temperatures from 200 to $1\,000 \text{ }^\circ\text{C}$, which are suspected at the base of the continental crust (cf. Fridleifsson *et al.* [58]), together with big differences in the thermal conductivity lead to large fluctuations in the temperature distribution. In regions with geological faults and rifts, particularly in the vicinity of volcanic activity and boundaries of tectonic plates, very high temperatures can occur near to the Earth's surface. Depending on the temperature and the prevailing pressure, water may be present here in liquid form or as vapour.

2.1.2 Usage of geothermal energy

A necessary condition to generally use thermal energy is a temperature gradient. Thereby, the energy yield rises with the temperature difference. The majority of today's production of geothermal energy is used for the heating of buildings and the preparation of hot water. If locally much more geothermal heat is available, also other, more exceptional fields of application are possible like the heating of pavements and roads to remove snow and ice during the winter. This practice is mainly encountered in Iceland, where the prevailing geological conditions lead to very high temperatures in shallow depths. Beside the direct use of geothermal heat, a conversion into other forms of energy is possible. This is usually done with a steam-driven turbine. The generated mechanical energy can either be used directly, or converted into electrical energy using a generator.

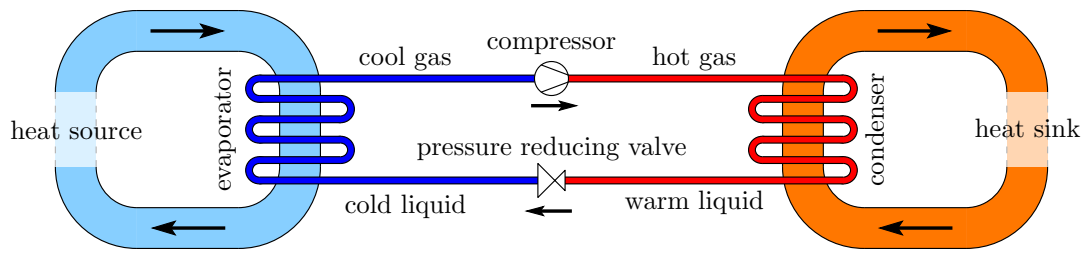


Figure 2.2: Schematic illustration of a mechanical heat pump.

In the case that the required temperature difference is not already achieved, it is possible to increase it by use of a heat pump. However, to this end, it is necessary that the system is supplied with additional energy. The effect of a heat pump is a heat transfer in the opposite direction of spontaneous heat flow, which consequently leads to a higher temperature difference. The probably most well-known applications for heat pumps are refrigerators and air conditioners, where they are used to increase the temperature difference between the cool inside and the warm environment. The commonly used heat pumps can be classified by their operating principle into two categories, the compression and the absorption heat pumps. The main difference between these categories is the supplied energy in each case, whereas mechanical energy is used for the compression heat pumps, the absorption ones work with thermal energy. The working principle of the compression heat pump is depicted in Figure 2.2 and is further described exemplarily. The heat pump consists of a closed loop, which is filled with a working fluid. At the heat source, this working fluid flows through a heat exchanger under low pressure, where it gets heated and, therefore, evaporates. Afterwards, the vapour is compressed by a compressor and, thereby, raised to a higher temperature level. In a second heat exchanger, the working fluid releases some of its energy to the heat sink and condenses. Following that, the pressure and consequently the temperature level of the fluid are decreased by means of a valve. Thus, when choosing the working fluid, in particular the boiling temperature plays an important role, although the boiling point can be adjusted via a suitable choice of operating pressures. It is clear that the variation between the existing and the required temperature difference is essential for the efficiency of the total system, because there may be a considerable amount of energy that has to be supplied for the compression.

Geothermal reservoirs can be categorised either by their location or their prevalent temperature. According to Haenel *et al.* [72], a low-enthalpy resource corresponds to a reservoir temperature of less than $150\text{ }^{\circ}\text{C}$, whereas the temperature for high-enthalpy resources exceeds $150\text{ }^{\circ}\text{C}$, see also Chandrasekharam & Bundschuh [27]. For temperatures beyond $150\text{ }^{\circ}\text{C}$, the water vapour can be used directly to operate a turbine. In a case where the temperature is lower, water has to be replaced as the working fluid by another component that has its boiling point at a lower temperature. It is common practice for this purpose to use either an Organic Rankine Cycle (ORC) or a Kalina cycle. It should, however, be noted that, whereas the ORC operates with an organic working fluid, the Kalina cycle employs an inorganic one. Then, the vapour of either of these methods can be utilised to generate electricity. The important point is that using these techniques, temperatures of as low as $80\text{ }^{\circ}\text{C}$ are sufficient. Regarding the location, one distinguishes between near-surface and deep geothermal reservoirs and, moreover, geothermal energy from tunnels

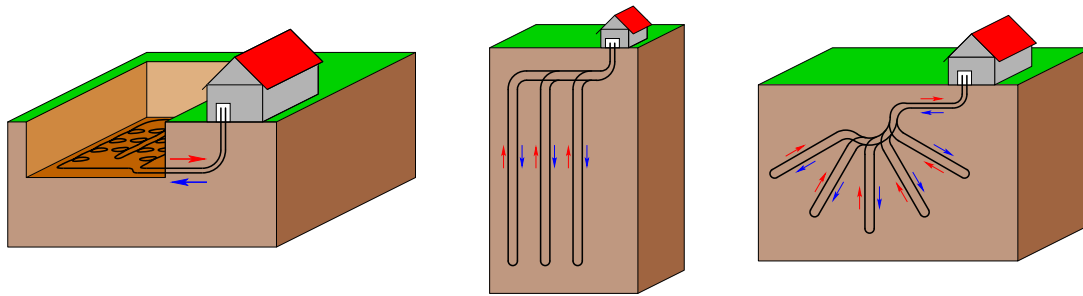


Figure 2.3: *The most common configurations of near-surface ground heat exchanger: a geothermal collector (left), a geothermal probe (middle) and a GRD (right).*

and from mines. There are installations in all sizes, ranging from small plants for space and water heating of family houses, up to large plants for power generation.

In small, near-surface installations, a working fluid, usually water, mixed with a frost protection agent circulates in a closed loop. This means that the fluid is isolated by tubes from the underground, what strongly limits the surface area available for the heat transfer from the surroundings. Thus, the diameter, length and position of the tubes need to be adjusted according to the circumstances and requirements. In Figure 2.3, three possible configurations of a near surface ground heat exchanger are illustrated. **Geothermal collectors** are placed horizontally in a depth of 80 to 160 cm. The collectors cause a significant space requirement for the installation, because the pipes are laid into the open pit, but, therefore, fortunately, no elaborate drilling must be carried out. A further disadvantage of this type is the fact that with a lower outdoor temperature, the temperature in the ground at this depth also decreases. As a consequence, exactly in the times when heat is particularly needed, less heat is available. The soil around the collector should be water saturated, because this would increase the thermal conductivity. If the collectors are furthermore not built over, the heat from precipitations can also be used. **Geothermal probes** are installed vertically to a depth of 50 to 160 m. They benefit from the prevailing, constant temperature there. In addition, they only need a very small space at the surface. Depending on the required capacity, one or two probes are sufficient for small residential buildings, whereas significantly more probes are used for larger offices or commercial buildings. Using shallow geothermal energy with probes is the most widely used method in central and northern Europe. For the **Geothermal Radial Drilling (GRD)**, probes of 30 to 40 m length are installed in different directions into the underground. By doing that, one can also benefit from the constant temperature that exists from the depth of 10 to 15 m. This method also requires very little space on the surface and is recommended, for example, in case of a depth limitation by existing regulatory requirements. Frequently, at least in Germany, the use of geothermal energy collectors and probes is prohibited in some regions, or authorised only under certain conditions. This is particularly the case in water protection zones and geologically tricky areas such as karst or confined aquifers.

Installations for the use of high temperatures at greater depths can be furthermore distinguished in terms of permeability of the subsoil. A deep, water-bearing reservoir with a high permeability is also known as a hydrothermal system, whereas a reservoir with a low permeability is called a petrothermal system. The original designation hot dry

rock (HDR) for the method of extracting energy out of petrothermal systems is a little misleading, because the rock is actually not dry. Therefore, additional names have been established over time as hot wet rock (HWR), hot fractured rock (HFR) and finally enhanced geothermal system (EGS), which is probably the most common term today, cf. Valley [117]. The primary difference between the two mentioned systems is the fact that in the case of an EGS, usually the reservoir has to be firstly created, cf. section 2.2, whereas, in the context of hydrothermal systems, the thermal water can be taken directly out of the existing reservoir.

2.2 Composition and functions of enhanced geothermal systems

EGS systems can be installed almost everywhere, independent of natural occurrence of thermal water, as far as sufficiently high temperatures are available in a reachable depth. At least two wells, one IW and one PW, are necessary for the operation of a plant, where the maximum depth of the wells usually is in a range between 3 to 6 km. By appropriately deflecting the drilling, it is possible to reduce the distance between the wells at the surface to a few metres although the distance in the underground is actually a few hundred metres. Compared with other types of power plants, geothermal plants are usually much smaller and, therefore, the impairment of the scenery is very low. This improves the social acceptance of geothermal power plants in the neighbourhood.

The efficiency of a power plant is described by the ratio between the energy produced and the energy required during the operation. Therefore, in order to maximise the efficiency of EGS, the amount of energy required for the extraction of hot water must be kept as small as possible, at concurrent highest possible flow rates and temperature. The majority of the expended energy is needed for the pumps that generate a sufficient pressure difference between the IW and the PW. It should be noted at this point that for a given flow rate, a higher permeability naturally reduces the necessary pressure difference. There might be several reasons which can lead to a drop in temperature at the PW. One reason may be the existence of a few large cracks, such that the contact surface between the water and the rock is very small and, therefore, the water is not heated enough. Moreover, very high flow rates can lead to a fast cool down of the whole reservoir, when the heat from the outside of the reservoir cannot flow in fast enough. This influx of heat into the EGS occurs almost exclusively by heat conduction within the rock and not, as in hydrothermal systems, convectively, by flowing water. In summary, it can be said that the extraction rate must be adjusted according to the given circumstances.

In an EGS, water is pumped down through the IW into the reservoir. Afterwards, it flows along the pressure gradient through the reservoir and is thereby heated by the rock until it is pumped through the PW back to the surface. Subsequently, in a heat exchanger, the heat from the produced water is transferred to another working fluid which, as a result, evaporates. This vapour drives a turbine, which converts the mechanical into electrical energy. After that, the working fluid is cooled and liquefied in another heat exchanger. Here, the arising heat can be further used, for example, as district heating. Figure 2.4

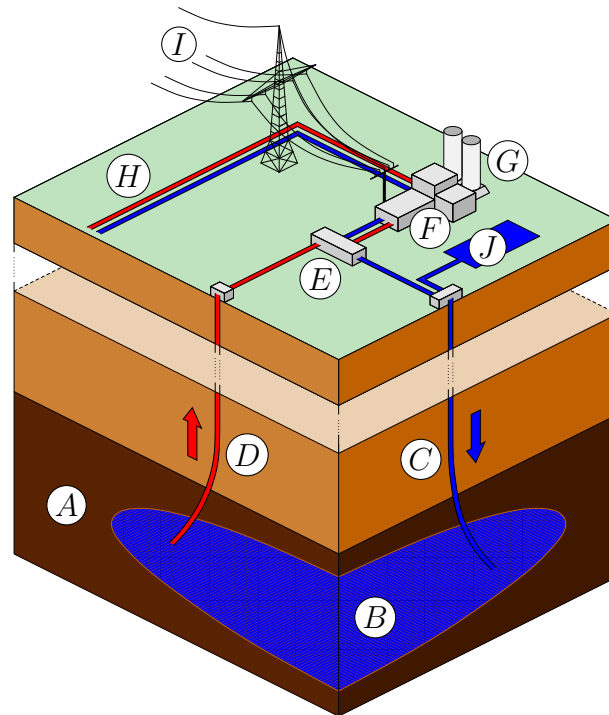


Figure 2.4: *Functional principle of an EGS power plant with A: impermeable rock, B: geothermal reservoir, C: IW, D: PW, E: heat exchanger, F: turbine hall, G: cooling tower, H: output for district heating, I: electricity output, J: water reservoir.*

illustrates the basic design of an EGS.

2.2.1 Preparation of boreholes and implementation of wells

In the following, the creation and the design of geothermal wells are described. The information presented is taken, unless otherwise indicated, from the Handbook of Best Practices for Geothermal Drilling (Finger & Blankenship [55]). For a more detailed insight, the interested reader is recommended to read this book.

Drilling deep wells to an overall depth of several hundred metres or even a few kilometres is carried out with a drilling rig with an attached mud pump. To increase the stability of the well, it is conventional practice to successively set separate strings of casing. The length of a string is hereby determined by several factors, for example, the fracture gradient, swelling phenomenon in the surrounding subsurface, unstable formation, a big pressure difference between pore and drilling fluid, determinative well control considerations, or even regulatory requirements. Since the drill bits and further casing strings must fit through the already installed casing strings, for the further course of the borehole, the well diameter has to be reduced inevitably string by string with depth. Thus, the necessary diameter at the lower end of the well needs to be considered already at the planning stage. It must also be kept in mind that sometimes, due to unforeseen events, an additional casing string is needed. However, The required lower well diameter depends on the targeted production rate and on the permeability of the subsoil. In geothermal systems, usually a diameter in the range between 20 and 34 cm is used. In addition to the resistance

capability against mechanical stress, the casing strings are specially protected against corrosion, because the fluids in the subsoil contain hydrogen sulphide (H_2S). This issue is detailed in ISO² 15156 [91]. In the productive area of the well, the well can either be left as-drilled (open-hole completion) or needs to be supported by a slotted liner (slotted tube), if the surrounding underground is not stable enough.

During the drilling process, the well is flushed continuously with a drilling fluid, also known as drilling mud, which is introduced through the drill string. The drilling fluid emerges into the wellbore at the drill bit and flows upward again between drill pipe and casing, together with the cuttings. In the context of geothermal drilling, this water-based drilling fluid fulfils different tasks. The main purpose is, as already mentioned, to carry the cuttings up to the surface. But, it also cools the drill head, such that it does not overheat. Moreover, the borehole walls are supported by the mud pressure from collapsing. Furthermore, by adding appropriate additives, the corrosion of the drilling tools can be reduced. The additives also permit the manipulation of the viscosity and, within certain limits, of the density of the drilling fluid. After cleaning the fluid at the surface and, if necessary, adding further additives, it can be reused.

2.2.2 Hydraulic stimulation and the creation of a geothermal reservoir

According to Jung [81], for an economically viable operation of a plant that uses the thermal energy from crystalline bedrock, the flow rate must be at least 50 to 100 l/s. To thereby produce an electrical power of 3-10 MW_{el} for 25 years, a minimum distance between the wells from 0.5 to 2.0 km is needed. Moreover, a crack surface area of 5 to 10 km^2 and a volume of rock to be accessed by the fracture system of about 0.1 to 0.3 km^3 should be available. In order to get an appropriate reservoir, new cracks for a bigger and finer fracture network have to be created and the existing cracks should be increased accordingly. This can be done by massively injecting water under high pressure through a well. Thereby, the pressure of the water must exceed the absolute value of the former, least principal stress of the rock. The crack propagates perpendicular to the direction of the least principal stress, which is the so-called “fracture gradient”. Since the lithospheric pressure results from the weight of the overlying subsoil, it increases with depth. Mostly, the horizontal Earth pressure is lower, which supports the formation of vertical cracks. However, there exist some exceptions, such as in Central Australia, where the compression of the continent finally leads to horizontal fractures.

First experiments for the generation of a geothermal reservoir in an initially almost impermeable underground took place in the early 1970s, when a group of the Los Alamos National Laboratory examined the creation of a geothermal reservoir in the hot granites underlying the Jemez Plateau in northern New Mexico (Smith *et al.* [108]). Although, the project was shut down as it ultimately failed to produce more energy than was needed for the operation of the installation, the idea of an artificial creation of reservoirs has been further developed in the following decades. To get information about the result-

²International Organization for Standardization.

ing reservoir during the course of stimulation, it is important to collect as much data as possible. Due to the fact that the subsoil apart from the wells is not directly accessible, additional indirect measurements must be performed. The measurable quantities in the well are the temperature, the pressure and the amount and velocity of the water flowing through. By use of very accurate instruments for the detection of accelerations, it is furthermore possible to measure the small vibrations which are caused by the growth of a crack. The positioning of several seismic instruments allows a determination of the strength (magnitude) and the position of the events, where the different travel times of the seismic waves to the individual instruments are exploited. Hence, finally, the cloud of the locations of this recorded induced seismic events facilitates the identification of the shape and the spatial distribution of the fractured domain. According to Majer *et al.* [87], there exist several possible reasons for induced seismicity during the development or the operation of EGS and, unfortunately, this seismicity is not limited to very small events. Thus, occasionally also seismic responses occur with magnitudes larger than 3. Bigger seismic events can cause damage at buildings and have, therefore, besides the financial losses, a very negative impact on the public perception of geothermal projects. One example, that can be mentioned here, is the Deep Heat Mining project in Basel, which has been ceased after several major seismic shocks (Giardini [66]). A good overview about induced seismicity due to geothermal fluid injection can be found in Evans *et al.* [54].

Besides the purely hydraulic stimulation, there are further possibilities to support the generation of a reservoir. For a **thermal stimulation**, the surface of the fractures within the hot rock is strongly cooled by injecting cold water and, thereby, causing internal stresses in the rock. This, in turn, triggers the initiation of new cracks or, at least, the enlargement of existing cracks (Benson *et al.* [13]). During a **chemical stimulation**, acid is injected into the ground, so as to increase existing cracks by dissolving material from the rock. For the removal of calcium and carbonates, usually hydrochloric acid (HCl) is used. In order to additionally solve even silicate minerals, also hydrofluoric acid (HF) can be added. Acids can only be used for the stimulation if the cracks in the rock already exist, which then are enlarged with this procedure. When using acids and other additives such as biocides, there is always a risk that the additives inadvertently enter other areas, such as a groundwater bearing layer. This may happen via previously unknown vertical permeabilities in faults, or even simply through leaky areas in the casing of the well.

In the subsurface, there are also natural occurrences of unstable radionuclides such as radium-226 and radium-228, which decay radioactively. Therefore, the waste water from the drilling and the stimulation, and also the circulating water in the productive operation of the plant may contain radionuclides and must, if it cannot be easily re-injected, be judged with respect to its radioactivity and be treated accordingly.

2.2.3 The European geothermal test site in Soultz-sous-Forêts

The European test site in Soultz-sous-Forêts (France) has been developed and extended over the last 20 years and has finally become a power plant which produces electrical energy. It is located in a geothermal anomaly within the Upper Rhine Graben.

Geological conditions

The Upper Rhine Graben is a major rift in the NW-Alpine foreland. It is a part of the European Cenozoic Rift System that extends from the Mediterranean to the North Sea (Ziegler [121]). The Upper Rhine Graben results from the lithospheric thinning in the European Cenozoic Rift System and lithospheric folding. This process starts in the late Eocene and is caused by the Alpine orogeny (Bourgeois *et al.* [21]). With a width of about 40 km, the Upper Rhine Graben extends 300 km in NNE-SSW-direction between the cities of Basel and Frankfurt/Wiesbaden, and is overlain by 1400 m of sediments. The deep thermal structure of the Upper Rhine Graben is attributed to an uplift of the mantle, such that the Moho is only 24 km beneath the surface in the southern area of the Upper Rhine Graben (Brun *et al.* [26]). Figure 2.5 shows a map with the location of the Upper Rhine Graben.

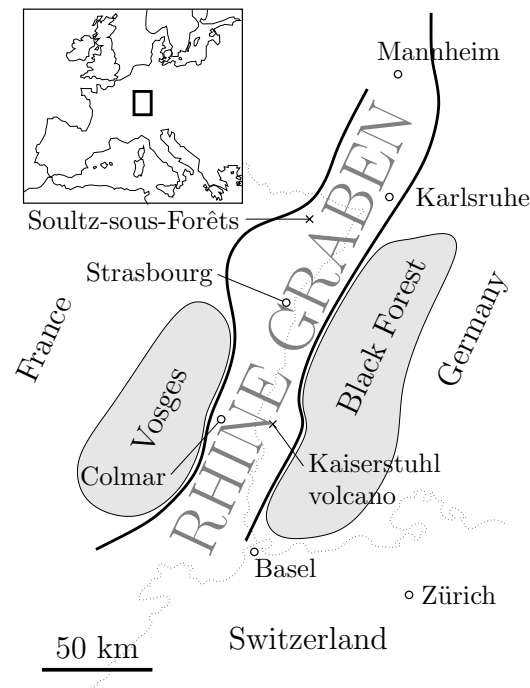


Figure 2.5: Map of the Upper Rhine Graben, Central Europe.

Pribnow & Schellschmidt [98] have shown that the temperature at shallow depths of about 800 m is highly variable, and the vertical heat flow of $100\text{--}120\text{ mW/m}^2$ is rather high in the Graben compared to 80 mW/m^2 for the surrounding area. They have also found by evaluating a temperature log from a well at the Sultz-sous-Forêts site that the temperature gradient is highly dependent on the local material properties. If the heat is mainly transferred by fluid convection, the temperature gradient is very small compared with regions where due to small permeabilities the heat flow is driven by conduction. Particularly, because of a thermal anomaly, the temperature in the subsurface at Sultz-sous-Forêts is very high.

Chronology of the test site

In 1987, Gérard & Kappelmeyer [70] described the decision of an international team from France and Germany to explore the subsurface in Soultz-sous-Forêts to find out the reason for the thermal anomaly. Due to the oil extraction in the 1950s in the former Pechelstein oil field, which is close to the test site in Soultz, the existence of the thermal anomaly was already known at that time. The first borehole for the new project is called GPK-1 and it was drilled to a depth of 2 km, while the top of the granite was reached after 1 376 m. The thermal anomaly results in a BHT of 140 °C. Whereas, in the sedimentary rock, the temperature gradient of 10.5 °C per 100 m and the heat flux of 176 mW/m², are very high, these values reduce in the granite basement to a quasi-normal state of 2.8 °C per 100 m and 82 mW/m² (Baria *et al.* [5]). Another borehole (EPS-1), which exists already from the former oil production to a depth of 830 m, has been deepened to 2 227 m, where, from a depth of 930 m on, a continuous coring was performed to get detailed information about the orientation and the dimensions of fractures, the density of fracture zones, and also about the chemical and mineralogical features. The process of drilling and coring of EPS-1 and the analysis of the macroscopic fractures are described in detail by Genter & Traineau [63, 64]. In 1991, the borehole GPK-1 was stimulated in Packer³ isolated zones with a temporarily maximum rate of 15 l/s. The existing wells from the oil production were used to create a network for the seismic observation of the stimulation. In the following time, GPK-1 was deepened to 3 590 m where the BHT reached 160 °C (Garnish *et al.* [59]). In 1993, four fresh-water stimulations of GPK-1 have been realised at various open-hole intervals with flow rates up to 50 l/s and a maximum pressure of approximately 10 MN/m². During the stimulation, over 19 000 seismic events were recorded. Most of them originated from a specific fracture zone, intersecting the borehole at 3 480–3 485 m. The stimulation and the meanwhile observations are described by Evans *et al.* [53] and Jung *et al.* [82]. Evans [52] also examined the prevailing underground stress state and the resulting fracture mechanisms. He concluded that the stress regime in Soultz is typical for active graben setting. The minimum principal stress is in horizontal direction with orientation N80°E ± 15° and the magnitude of the vertical stress is about 200 % of the minimum horizontal stress. Finally, he concluded that shearing is the most common damage mechanism, where dislocations for the fractures are in the region of some millimetres to a few centimetres. The transmissivity was increased by a factor of 15.

In late 1994, a second borehole (GPK-2) was drilled south of GPK-1 to a depth of 3 876 m with a 650 m open-hole section and an open-hole distance between the boreholes of about 450 m. The measured temperature was 168 °C at 3 800 m, which was the deepest observation point at that time. After some more stimulations of the reservoir via GPK-2, which were described, e. g., by Baria *et al.* [5], a short-time circulation test with flow rates up to 20 l/s and an extraction temperature of 130 °C was realised for the duration of a few days (cf. Baumgärtner *et al.* [11]). This corresponds to approximately 8–9 MW_{th} and, by assuming a state-of-the-art energy transformation to electricity, the produced energy

³Packer is a standard component to provide a seal between the outside of the production tubing and the inside of the casing, liner, or wellbore wall.

would have exceeded the required energy for the production. In 1997, a four-month circulation test showed how the flow resistance, the flow rate and the extraction temperature changed with time (Baumgärtner *et al.* [10]). Since corrosion and scaling were shown to be problematic in the previous short-term test, the goal was to examine how these problems can be avoided or at least reduced. The test was performed with flow rates of 22 l/s, 23 l/s and 25 l/s. In addition to a centrifugal pump at the IW GPK-1, a high-temperature feed pump with a nominal power of 250 kW was deployed in the PW GPK-2 at a depth of 430 m. Using the pumps, the entire produced water was re-injected. At the surface, the extracted fluid was conducted in a closed system under a pressure of 1 MPa. This prevented oxygen and carbon dioxide from entering the system, circumstance which would have led to corrosion and the precipitation of calcium carbonate, respectively. It eventually became clear that there was no need for the initially added acrylate polymers, which had originally been used precisely in order to prevent corrosion and precipitation. Abandoning acrylate polymers also had the positive consequence that the filter no longer had to be changed every day, and a few days after the addition was stopped, also the required injection pressure decreased from 3.5 MPa to 2 MPa. Therefore, it can be concluded that the acrylate polymers have a strong negative influence on the permeability.

Based on the positive experiences from the long-term circulation test, a deeper reservoir was planned using three wells (triplet) with boreholes to a depth of 5 km. One IW (GPK-3) in the middle of two lateral PW (GPK-2 and GPK-4). In order to simplify the layout on the surface, all three wells were drilled from the same platform and have been deviated in the underground. At first, GPK-2 was recased and deepened to 4 955 m, with a casing shoe at 4 403 m. It should be noted that the cited depths are taken from Dorbath *et al.* [34], and describe the true vertical depth (TVD) measured from the drilling platform. In 2000, the deep reservoir around GPK-2 was stimulated via the open hole. After the injection of 400 m³ of heavy brine (density ≈ 1.2 kg/l) to initiate the stimulation as deep as possible, more than 20 000 m³ of fresh water were injected by flow rates from 30 to 50 l/s (Weidler *et al.* [119]). During the stimulation, more than 30 000 triggers were detected by the microseismic network and almost 14 000 seismic events were localised. By evaluating the locations where the seismic events occurred, the NNW-SSE orientation of the reservoir became clearly visible (Dorbath *et al.* [34]). In 2002, the second borehole (GPK-3) of the planned triplet was also drilled to a depth of 5 091 m with an open-hole distance of 600 m to GPK-2. The casing-shoe of GPK-3 was set at 4 487 m. The stimulation of GPK-3 took place in summer 2003 and is described in detail by Baria *et al.* [6]. Just like during the stimulation of GPK-2, the initial injection of heavy brine, was followed by more than 30 000 m³ fresh water. The flow rate was varied between 20 and 60 l/s with two additional pulses of 100 and 90 l/s for only a few hours each. Six days after the beginning, the stimulation was supported by an additional injection with a flow rate of 25 l/s in GPK-2. During this stimulation, over 90 000 triggering events were recorded and about 8 000 seismic events were located. Although the number of seismic events decreased, the amount of injected water was enhanced by a factor of 1.5. In 2004, GPK-4 was drilled to a depth of 4 982 m with an open-hole distance to GPK-3 of about 650 m. The casing shoe of this last borehole of the triplet was set at 4 479 m. The stimulation of GPK-4 began with the hydraulic fracturing for nearly four days with a flow rate of 30 l/s and three “shocks” at 45 l/s, injecting at first 560 m³ of heavy brine followed by 9 300 m³ of fresh water. After

a first peak of 17 MPa, the well-head pressure stabilised at around 16 MPa, and it only increases by about 2 MPa during the “shocks”. Then, unfortunately, the stimulation was interrupted due to the failure of a pump. It took almost half a year until the stimulation could be continued. Finally, the second part of the hydraulic stimulation took place in spring 2005, when 12 300 m³ were injected within 4 days with flow rates between 25 and 45 l/s. Due to the fact that the instruments and triggering levels of the down-hole seismic network had been changed, the number of 22 718 registered and 9 570 localised events can't be compared to the number of events found during earlier stimulations. During this period, there have been only 1 341 events that were localised by the surface network. This is a really small amount compared with the previous stimulations. The fact that the overpressure in GPK-2 and GPK-3 was negligible during the stimulation of GPK-4 leads to the conclusion that the connectivity between GPK-4 and the other two wells is very low. A summarising overview concerning the hydraulic stimulations of the deep EGS reservoir is given by Dorbath *et al.* [34].

Subsequently, after the hydraulic stimulations, low pressure injection tests were performed in order to determine the productivity or injectivity of the wells. Tischner *et al.* [112] compared the tests and concluded that the productivity has risen considerably due to the stimulation and was then largely preserved afterwards. They found that the factor for the increase of productivity was almost 20 for GPK-2, 1.5 for GPK-3 and 20 for GPK-4. The enhanced productivity can hereby be attributed mainly to shear failure along existing cracks. Solely in GPK-4, the pressure response to the injection indicates a tensile fracturing. This assumption is also supported by the flow logs that show a continuous decrease in the flow rate over a height of about 300 m (4 500–4 800 m), which actually can only be explained by a long vertical crack.

After the hydraulic stimulations, also chemical stimulations were tested through the three boreholes GPK-2, GPK-3 and GPK-4 (Nami *et al.* [92], Portier *et al.* [97]). Hereby, a special focus was on GPK-4 because of its, so far, very low connectivity. In GPK-2, the chemical stimulation was confined to 1 460 m³ of 0.09–0.18 % HCl. GPK-3 was first stimulated with 865 m³ of 0.45 % HCl and later on with 250 m³ organic clay acid (OCA). OCA consists of 5–10 % citric acid (C₆H₈O₇), 0.1–1 % HF, 0.5–1.5 % fluoroboric acid (HBF₄), and 1–5 % ammonium chloride (NH₄Cl). For GPK-4, four different solutions were tested in order to increase the permeability. The first one was an injection of 4 700 m³ of 0.2 % HCl. One year later, a stimulation with 200 m³ regular mud acid, which consists of 12 % HCl and 3 % HF, was followed. A stimulation with 200 m³ chelatants was performed next. Hereby, 19 % trisodium nitrilotriacetate (Na₃NTA) at pH 12, caused by the addition of NaOH, was injected. It turned out that, unfortunately, the Na₃NTA stimulation reduced the productivity. One conjecture is that scales have been detached from the casing, and were transported into the reservoir, where they partly clogged the cracks. Finally, a stimulation with 250 m³ OCA was also carried out in GPK-4. A chronological overview of the chemical stimulation is given in Table 2.1. The injectivity/productivity index after the chemical stimulations increased by a factor of 1.25 for GPK-2, 1.15 for GPK-3 and 2.5 for GPK-4. Since the casing of GPK-4 was defective, the factor, considering only the productivity of the open-hole, is actual more likely in the range 1.5–1.75 (Genter *et al.* [62]).

Date	Well	Injected solution [m ³]	Solution	Flow rate [l/s]
13.02.2003	GPK-2	650	0.18 % HCl	30
14.02.2003	GPK-2	270	0.18 % HCl	15
14.02.2003	GPK-2	540	0.09 % HCl	30
27.06.2003	GPK-3	865	0.45 % HCl	20
02.02.2005	GPK-4	4 700	0.2 % HCl	27.2
17.05.2006	GPK-4	200	12 % HCl + 3 % HF	22
19.10.2006	GPK-4	200	NaOH + 19 % Na ₃ NTA	35
15.02.2007	GPK-3	250	OCA	55
21.03.2007	GPK-4	250	OCA	55

Table 2.1: Chronological overview of the chemical stimulation at Soultz (cf. Nami *et al.* [92]). Herein, OCA consists of 5–10 % C₆H₈O₇ + 0.1–1 % HF + 0.5–1.5 % HBF₄ + 1–5 % NH₄Cl.

From July to December 2005, after the hydraulic stimulation and the chemical stimulation with HCl, a long-term circulation test was performed for the triplet, see Gérard *et al.* [69] and Genter *et al.* [62]. Hereby, 205 000 m³ of water was produced via GPK-2 at 160 °C and via GPK-4 at 120 °C with a cumulative flow rate of 151/s driven by buoyancy without any down-hole production pumps. To prevent mineral scaling, the well-head pressure was maintained at 0.8 MPa. The cycle was closed by re-injecting the produced water into GPK-3, whereby the necessary well-head pressure of GPK-3 was increased to 7 MPa during the test. During the re-injection, about 600 microseismic events were recorded due to the circulation test. Some of these events exceeded magnitude 2.0, and some could even be felt on the surface. Sanjuan *et al.* [103, 104] conducted tracer tests during the circulation, which reveal a better connectivity between GPK-2 and GPK-3 compared with GPK-4 and GPK-3. Moreover, the fact that from GPK-2 only 25 % and from GPK-4 only 2 % of the injected tracer was recovered after 5 months of circulation suggests that the generated reservoir is connected to a large natural reservoir.

After the successful circulation in 2005, it was decided to build a geothermal power plant. The targeted flow rate was 351/s with a production temperature of 175 °C. Due to the high salinity of the produced water, which induces corrosion issues and would also lead to scaling problems in the turbine, only a binary plant is possible. Therefore, a closed ORC with isobutane as the working fluid was built, where the heat energy was transferred from the extracted fluid via a heat exchanger to the working fluid. The production of electricity using a radial turbine at 13 000 rpm started on 13th June 2008. At that time, only GPK-2 was used as a PW. After cooling down the geothermal water in the heat exchanger to 80–90 °C, it was completely re-injected into the reservoir via GPK-3. For this process, a well-head pressure of 6–7 MPa was needed at the IW. A line-shaft pump (LSP) in a depth of 350 m in GPK-2 provided a flow rate of 251/s at 164 °C. The production fluid was maintained at the surface at a pressure of 2 MPa. The test was interrupted in August 2008 due to a carbonate scaling problem in the LSP, which led to a failure of the shaft. The scaling problem was caused by the high mineral content of the fresh water that was

injected from the surface into the enclosing tube in order to lubricate the shaft. The density of seismic events during the circulation test was almost the same as it was in 2005, but the magnitude never exceeds 1.4. After the problems in GPK-2 had been fixed and the LSP was re-installed in 250 m depth, another test started in November of the same year. This time, besides of the LSP in GPK-2, an electric submersible pump (ESP) was installed in GPK-4 in a depth of 500 m, so an overall flow rate of 28 l/s was achieved for a period of 17 days. During this time, the thermal output of the circulation was around 12 MW_{th}. Due to various issues with the LSP, the air cooling system and the heat exchanger, this test had to be stopped. The final temperature of the produced water was 163 °C for GPK-2 and 155 °C for GPK-4. From March 2009 on, several circulation tests were performed with a long-term test in 2010 for about eleven months. More details concerning the first circulation tests and the building of the plant can be found in Genter [60]. In the further operation of the plant, there have always been problems with the LSP. To handle these problems, softened water and later on purified water by reverse osmosis with sulphite was used for the lubrication. After all, in 2012, a new pump was developed based on an ESP. It was installed and put into operation in January 2013. Further details on the operation and the meanwhile appearing problems of the production pump are described by Ravier *et al.* [100].

In the further course, it was found that GPK-4 could not be used for an efficient production. Therefore, GPK-2 became the only PW. However, GPK-1 was reused as IW. Further long and short term circulation tests that have been performed in the following years are described by Genter *et al.* [61]. During these tests at flow rates up to 26 l/s and a production temperature of 160 °C of the extracted water, a mean electrical gross power of 500 kW_{el} and a thermal power of over 8 MW_{th} has been achieved. Thus, since the energy consumption of the operating plant was around 400 kW_{el}, the EGS power plant was able to produce net power.

Findings from the test site

In petrothermal systems, the hydraulic stimulation is suitable for obtaining a transmissivity, which is high enough to operate a geothermal plant. Chemical stimulation is another way to increase the permeability of the reservoir, however, with a much smaller effect compared to the hydraulic stimulation. The knowledge about the existence of large permeabilities in the underground is one of the results from the numerous experiments and studies in Soultz that should be mentioned here. It was found by the seismic observation and also from logging activities, e. g., flow logs, UBI logs, and caliper logs in the boreholes that there are more or less a few fault regions with a much higher transmissivity compared to the surrounding, almost impermeable rock. Although, the preferred direction of propagation and the rough dimensions of the reservoir can be estimated by seismic observations, finally, the geological structure remains uncertain and suitable approximations are inevitable for simulation purposes. It could be shown that with the operation of a geothermal power plant, more electrical energy can be generated than it is needed for the operation of the plant itself. However, there is still a large potential for further improvements of the efficiency.

Chapter 3:

Theoretical fundamentals of the Theory of Porous Media

In a geothermal reservoir, the water is flowing through cracks of various sizes, where most of them are very small. With today's technology, it is impossible to capture and describe physical processes of the subsurface on a microscopic level and, therefore, to simulate these. Moreover, the currently available computer hardware does not allow calculations within a domain size of several cubic kilometres, while modelling the processes on the microscopic level. Therefore, nowadays, the TPM is the most suited method (cf. Ehlers [40, 41]) to model fluid flow through a porous solid, such as, for example, highly fractured rock. The TPM is a continuum-mechanical approach to model multi-constituent continua. It is based on the TM as formulated by Truesdell [116] and Truesdell & Toupin [115], which is combined with the concept of volume fractions by Bowen [23, 24] to consider the local composition of the aggregate. Within this chapter, a brief overview of the fundamentals of the TPM is presented. After describing the basic idea of homogenisation and the concept of volume fractions, the kinematical relations, stress measures and finally mechanical and thermo-dynamical balance relations are introduced. More detailed descriptions can be found in de Boer [17], de Boer & Ehlers [20], Ehlers [38, 42], and citations therein. Moreover, for a historical overview the interested reader is referred to Ehlers [43].

3.1 Homogenisation and volume fractions

The framework of the TPM comprises a homogenisation process, where the real microstructure properties are volumetrically averaged over a representative element volume (REV). For the here presented model it is assumed that the total aggregate φ is composed of two constituents φ^α , a solid φ^S and a fluid φ^F . This leads to a model

$$\varphi = \bigcup_{\alpha} \varphi^\alpha = \varphi^S \cup \varphi^F \quad (3.1)$$

of superimposed and interacting continua φ^α , see Figure 3.1. In (3.1), α is a placeholder for the solid S and the fluid F constituent, respectively. In the sense of volume fractions, the total volume dv can be divided into partial volumes dv^α of the constituents. Thus, the local composition of the aggregate is determined by the volume fraction n^α of each constituent with

$$n^\alpha := \frac{dv^\alpha}{dv}. \quad (3.2)$$

Fulfilling the saturation condition

$$\sum_{\alpha} n^\alpha = 1 \quad (3.3)$$

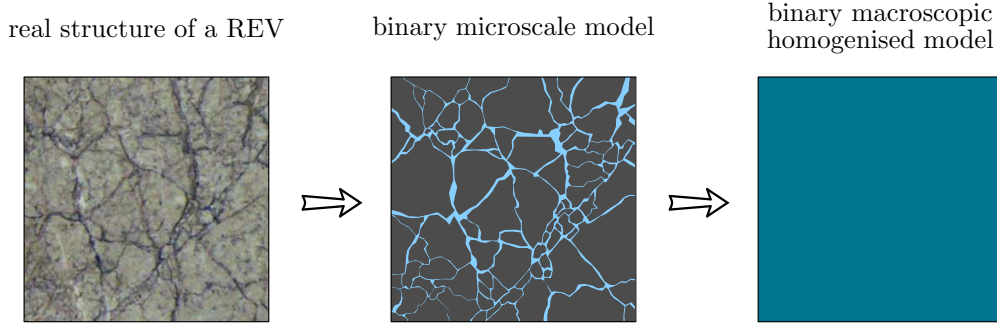


Figure 3.1: A REV of the real structure, an exemplary microscale model with two phases in separated volumes and a homogenised model of superimposed continua.

ensures that there is no vacant space within the domain. The introduction of the volume fractions allows the definition of two different densities, the realistic or material density $\rho^{\alpha R}$ and the partial density ρ^α , as the local mass element dm^α can be related either on the volume element dv^α of the respective constituent φ^α or on the entire volume element dv :

$$\rho^{\alpha R} := \frac{dm^\alpha}{dv^\alpha} \quad \text{and} \quad \rho^\alpha := \frac{dm^\alpha}{dv}. \quad (3.4)$$

The relation between the real and the partial density can be found with (3.2) as

$$\rho^\alpha = n^\alpha \rho^{\alpha R}. \quad (3.5)$$

Note that material incompressibility of a constituent ($\rho^{\alpha R} = \text{const.}$) does not imply a bulk incompressibility ($\rho^\alpha = \text{const.}$) since the volume fractions may change. It follows from (3.4) with $dm = \sum_\alpha dm^\alpha$ and is also shown later in (3.45) that the density ρ of the overall aggregate

$$\rho = \sum_\alpha \rho^\alpha \quad (3.6)$$

is the summation of all partial densities ρ^α .

3.2 Kinematical relations

3.2.1 Motion functions

The body \mathcal{B} consists of a superimposed and interacting continua, where each material point \mathcal{P}^α of a constituent φ^α follows its own motion function χ_α , starting from different locations \mathbf{X}_α in the reference configuration at time t_0 . In the actual configuration, at time t , each spatial position \mathbf{x} with

$$\mathbf{x} = \chi_\alpha(\mathbf{X}_\alpha, t) \quad (3.7)$$

is occupied simultaneously by material points of both constituents, cf. Figure 3.2. The assumption that the inverse motion function χ_α^{-1} assigns a unique reference position \mathbf{X}_α to every spatial point \mathbf{x} at time t requires a non-singular Jacobian determinant J_α :

$$\mathbf{X}_\alpha = \chi_\alpha^{-1}(\mathbf{x}, t), \quad \text{if} \quad J_\alpha := \det \frac{\partial \chi_\alpha}{\partial \mathbf{X}_\alpha} \neq 0. \quad (3.8)$$

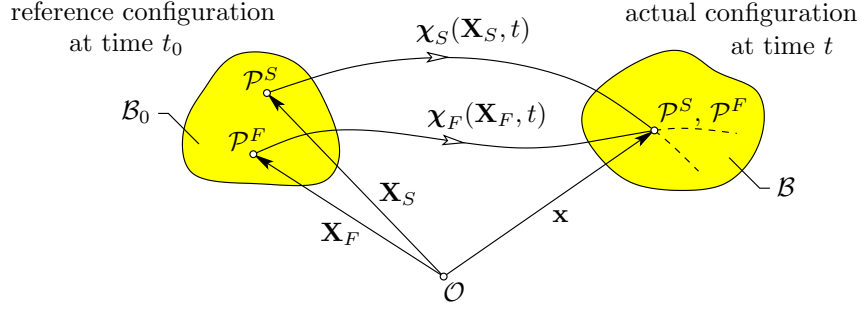


Figure 3.2: Motion of a binary aggregate.

The idea of a unique motion function for each of the constituents leads to individual velocity and acceleration fields, which can be given either in Lagrangean description as

$$\dot{\mathbf{x}}_\alpha = \frac{\partial \chi_\alpha(\mathbf{X}_\alpha, t)}{\partial t} = \dot{\mathbf{x}}_\alpha(\mathbf{X}_\alpha, t) \quad \text{and} \quad \ddot{\mathbf{x}}_\alpha = \frac{\partial^2 \chi_\alpha(\mathbf{X}_\alpha, t)}{\partial t^2} = \ddot{\mathbf{x}}_\alpha(\mathbf{X}_\alpha, t), \quad (3.9)$$

or with the inverse motion function (3.8) within an Eulerian setting as

$$\dot{\mathbf{x}}_\alpha = \dot{\mathbf{x}}_\alpha(\mathbf{x}, t) \quad \text{and} \quad \ddot{\mathbf{x}}_\alpha = \ddot{\mathbf{x}}_\alpha(\mathbf{x}, t). \quad (3.10)$$

In order to account for of the implicit time dependencies in the context of the Eulerian formulation, material time derivatives must be considered. Thus, the total time derivative of an arbitrary, steady and sufficiently often steadily differentiable scalar Υ and vectorial $\mathbf{\Upsilon}$ field function following the motion of the constituents φ^α or the barycentric velocity of the overall aggregate reads

$$\begin{aligned} (\Upsilon)'_\alpha(\mathbf{x}, t) &= \frac{d_\alpha \Upsilon}{dt} = \frac{\partial \Upsilon}{\partial t} + \text{grad } \Upsilon \cdot \dot{\mathbf{x}}_\alpha, & \dot{\Upsilon}(\mathbf{x}, t) &= \frac{d\Upsilon}{dt} = \frac{\partial \Upsilon}{\partial t} + \text{grad } \Upsilon \cdot \dot{\mathbf{x}}, \\ (\mathbf{\Upsilon})'_\alpha(\mathbf{x}, t) &= \frac{d_\alpha \mathbf{\Upsilon}}{dt} = \frac{\partial \mathbf{\Upsilon}}{\partial t} + (\text{grad } \mathbf{\Upsilon}) \dot{\mathbf{x}}_\alpha, & \dot{\mathbf{\Upsilon}}(\mathbf{x}, t) &= \frac{d\mathbf{\Upsilon}}{dt} = \frac{\partial \mathbf{\Upsilon}}{\partial t} + (\text{grad } \mathbf{\Upsilon}) \dot{\mathbf{x}}. \end{aligned} \quad (3.11)$$

Therein, the barycentric velocity

$$\dot{\mathbf{x}} = \frac{1}{\rho} \sum_\alpha \rho^\alpha \dot{\mathbf{x}}_\alpha \quad (3.12)$$

is an averaged velocity of the overall aggregate φ . Furthermore, the spatial operator $\text{grad}(\cdot)$ represents the gradient with respect to the actual configuration \mathbf{x} . Subsequently, the diffusion velocity

$$\mathbf{d}_\alpha = \dot{\mathbf{x}}_\alpha - \dot{\mathbf{x}}, \quad \text{with} \quad \sum_\alpha \rho^\alpha \mathbf{d}_\alpha = \mathbf{0}, \quad (3.13)$$

can be found as the relative velocity of a constituent with respect to the barycentric velocity of the aggregate.

For the description of biphasic materials in the context of the TPM, the motion of the solid is given by a Lagrangean formulation in terms of the displacement vector

$$\mathbf{u}_S = \mathbf{x} - \mathbf{X}_S, \quad (3.14)$$

and the fluid flow is related to the deforming solid. Therefore, the seepage velocity

$$\mathbf{w}_F = \dot{\mathbf{x}}_F - \dot{\mathbf{x}}_S \quad (3.15)$$

is considered within a modified Eulerian setting.

3.2.2 Deformation and strain measures

To describe the deformation, the material deformation gradient \mathbf{F}_α and its inverse \mathbf{F}_α^{-1} are introduced via

$$\mathbf{F}_\alpha = \frac{\partial \mathbf{x}}{\partial \mathbf{X}_\alpha} = \text{Grad}_\alpha \mathbf{x} \quad \text{and} \quad \mathbf{F}_\alpha^{-1} = \frac{\partial \mathbf{X}_\alpha}{\partial \mathbf{x}} = \text{grad} \mathbf{X}_\alpha. \quad (3.16)$$

In (3.16)₁, the spatial operator $\text{Grad}_\alpha(\cdot)$ represents the gradient with respect to the reference configuration of φ^α . In the undeformed initial state, the deformation tensor must match the second-order identity tensor \mathbf{I} whose determinant is equal to 1. So with

$$\mathbf{F}_\alpha(t = t_0) = \text{Grad}_\alpha \mathbf{X}_\alpha = \mathbf{I}, \quad \text{and} \quad \det \mathbf{F}_\alpha(t_0) = \det \mathbf{I} = 1, \quad (3.17)$$

and further considering the condition of a non-zero Jacobian determinant in (3.8) follows under the assumption of a continuous deformation gradient \mathbf{F}_α that

$$J_\alpha = \det \mathbf{F}_\alpha > 0. \quad (3.18)$$

Using (3.14) in (3.16), the deformation gradient for the solid constituent \mathbf{F}_S and its inverse \mathbf{F}_S^{-1} can be expressed in terms of the solid displacement, viz.:

$$\mathbf{F}_S = \text{Grad}_S \mathbf{u}_S + \mathbf{I} \quad \text{and} \quad \mathbf{F}_S^{-1} = \mathbf{I} - \text{grad} \mathbf{u}_S. \quad (3.19)$$

The two-field deformation tensor \mathbf{F}_α can be used for transformations between the reference and the actual configuration. Thus, the push-forward, from reference to actual configuration, and pull-back, from actual to reference configuration, mapping of line elements

$$d\mathbf{x} = \mathbf{F}_\alpha d\mathbf{X}_\alpha \quad \leftrightarrow \quad d\mathbf{X}_\alpha = \mathbf{F}_\alpha^{-1} d\mathbf{x} \quad (3.20)$$

follows from (3.16). Appropriate push-forward transport mechanisms can also be found for the area and volume elements, namely

$$d\mathbf{a} = \det \mathbf{F}_\alpha \mathbf{F}_\alpha^{T-1} d\mathbf{A}_\alpha = \text{cof} \mathbf{F}_\alpha d\mathbf{A}_\alpha \quad \text{and} \quad dv = (\det \mathbf{F}_\alpha) dV_\alpha. \quad (3.21)$$

Based on (3.20), further deformation measures can be introduced. Comparing the square of line elements in the reference and the actual configuration

$$\begin{aligned} d\mathbf{x} \cdot d\mathbf{x} &= d\mathbf{X}_\alpha \cdot (\mathbf{F}_\alpha^T \mathbf{F}_\alpha) d\mathbf{X}_\alpha =: d\mathbf{X}_\alpha \cdot \mathbf{C}_\alpha d\mathbf{X}_\alpha & \rightarrow & \mathbf{C}_\alpha = \mathbf{F}_\alpha^T \mathbf{F}_\alpha, \\ d\mathbf{X}_\alpha \cdot d\mathbf{X}_\alpha &= d\mathbf{x} \cdot (\mathbf{F}_\alpha^{T-1} \mathbf{F}_\alpha^{-1}) d\mathbf{x} =: d\mathbf{x} \cdot \mathbf{B}_\alpha^{-1} d\mathbf{x} & \rightarrow & \mathbf{B}_\alpha = \mathbf{F}_\alpha \mathbf{F}_\alpha^T, \end{aligned} \quad (3.22)$$

the right \mathbf{C}_α and the left \mathbf{B}_α Cauchy-Green deformation tensor can be found. Proceeding from the difference of the squares of the actual and the referential line elements, with (3.20) and (3.22) the Green-Lagrangean \mathbf{E}_α and the Almansian \mathbf{A}_α strain tensor are introduced:

$$\begin{aligned} d\mathbf{x} \cdot d\mathbf{x} - d\mathbf{X}_\alpha \cdot d\mathbf{X}_\alpha &= d\mathbf{X}_\alpha \cdot (\mathbf{C}_\alpha - \mathbf{I}) d\mathbf{X}_\alpha =: d\mathbf{X}_\alpha \cdot 2\mathbf{E}_\alpha d\mathbf{X}_\alpha, \\ d\mathbf{x} \cdot d\mathbf{x} - d\mathbf{X}_\alpha \cdot d\mathbf{X}_\alpha &= d\mathbf{x} \cdot (\mathbf{I} - \mathbf{B}_\alpha^{-1}) d\mathbf{x} =: d\mathbf{x} \cdot 2\mathbf{A}_\alpha d\mathbf{x}. \end{aligned} \quad (3.23)$$

For the description of the rates of deformation and strain, the material time derivative of the deformation gradient is introduced in a Lagrangean

$$(\mathbf{F}_\alpha)'_\alpha = \frac{d_\alpha}{dt} \mathbf{F}_\alpha = \frac{\partial \dot{\mathbf{x}}_\alpha(\mathbf{X}_\alpha, t)}{\partial \mathbf{X}_\alpha} = \text{Grad}_\alpha \dot{\mathbf{x}}_\alpha \quad (3.24)$$

and an Eulerian formulation

$$(\mathbf{F}_\alpha)'_\alpha = \frac{d_\alpha}{dt} \mathbf{F}_\alpha = \frac{\partial \dot{\mathbf{x}}_\alpha(\mathbf{x}, t)}{\partial \mathbf{X}_\alpha} = \frac{\partial \dot{\mathbf{x}}_\alpha}{\partial \mathbf{x}} \frac{\partial \mathbf{x}}{\partial \mathbf{X}_\alpha} =: \mathbf{L}_\alpha \mathbf{F}_\alpha. \quad (3.25)$$

Therein,

$$\mathbf{L}_\alpha := \frac{\partial \dot{\mathbf{x}}_\alpha(\mathbf{x}, t)}{\partial \mathbf{x}} = \text{grad} \dot{\mathbf{x}}_\alpha = (\mathbf{F}_\alpha)'_\alpha \mathbf{F}_\alpha^{-1} \quad (3.26)$$

is known as the spatial velocity gradient of φ^α . It is useful for the further application to split \mathbf{L}_α into a symmetric deformation velocity $\mathbf{D}_\alpha = \mathbf{D}_\alpha^T$ and a skew symmetric spin tensor $\mathbf{W}_\alpha = -\mathbf{W}_\alpha^T$, viz.:

$$\mathbf{L}_\alpha = \mathbf{D}_\alpha + \mathbf{W}_\alpha, \quad \text{with} \quad \mathbf{D}_\alpha = \frac{1}{2}(\mathbf{L}_\alpha + \mathbf{L}_\alpha^T) \quad \text{and} \quad \mathbf{W}_\alpha = \frac{1}{2}(\mathbf{L}_\alpha - \mathbf{L}_\alpha^T). \quad (3.27)$$

The rate of the right Cauchy-Green deformation tensor is derived by the material time derivative of (3.22)₁:

$$(\mathbf{C}_\alpha)'_\alpha = (\mathbf{F}_\alpha^T \mathbf{F}_\alpha)'_\alpha = 2\mathbf{F}_\alpha^T \mathbf{D}_\alpha \mathbf{F}_\alpha. \quad (3.28)$$

Thus, it follows for the rate of the Green-Lagrangean strain tensor:

$$(\mathbf{E}_\alpha)'_\alpha = \frac{1}{2}(\mathbf{C}_\alpha)'_\alpha = \mathbf{F}_\alpha^T \mathbf{D}_\alpha \mathbf{F}_\alpha. \quad (3.29)$$

3.3 External loads and stress measures

External mechanical loads can act on a body from a distance or at its vicinity. The action from a distance \mathbf{k}_B^α is usually interpreted as the gravitational force, which acts over the whole body on the mass of the constituent, such that

$$\mathbf{k}_B^\alpha = \mathbf{g} \int_B \rho^\alpha dv. \quad (3.30)$$

Therein, \mathbf{g} is the constant gravitation vector acting on all constituents. The action at the vicinity $\mathbf{k}_{\partial\mathcal{B}}^\alpha$ is a local contact load which appears at the surface $\partial\mathcal{B}$ of the body:

$$\mathbf{k}_{\partial\mathcal{B}}^\alpha = \int_{\partial\mathcal{B}} \mathbf{t}^\alpha \, da. \quad (3.31)$$

In addition to the actual position \mathbf{x} and the time t , the contact force $\mathbf{t}^\alpha = \mathbf{t}^\alpha(\mathbf{x}, \mathbf{n}, t)$ per surface area depends also on the outward-oriented unit surface normal \mathbf{n} . Thus, the total mechanical load on a constituent

$$\mathbf{k}^\alpha = \mathbf{k}_\mathcal{B}^\alpha + \mathbf{k}_{\partial\mathcal{B}}^\alpha, \quad (3.32)$$

is the sum of the applied volume and contact forces.

With the surface traction vector \mathbf{t}^α and Cauchy's Theorem

$$\mathbf{t}^\alpha(\mathbf{x}, \mathbf{n}, t) = \mathbf{T}^\alpha(\mathbf{x}, t) \mathbf{n} \quad (3.33)$$

the Cauchy stress tensor \mathbf{T}^α of a constituent φ^α can be introduced. Due to the fact that stress is defined as force per area, it is possible to find different stress tensors, depending on the concerned area element. The Cauchy stress is also known as the true stress, because it relates the actual surface force element $d\mathbf{k}_{\partial\mathcal{B}}^\alpha$ to the oriented area element $d\mathbf{a}$ of the actual configuration:

$$d\mathbf{k}_{\partial\mathcal{B}}^\alpha = \mathbf{T}^\alpha d\mathbf{a} \quad \text{with} \quad d\mathbf{a} = \mathbf{n} \, da. \quad (3.34)$$

Further definitions of stress tensors are:

$$\begin{aligned} \boldsymbol{\tau}^\alpha &= (\det \mathbf{F}_\alpha) \mathbf{T}^\alpha & : & \text{Kirchhoff stress tensor,} \\ \mathbf{P}^\alpha &= (\det \mathbf{F}_\alpha) \mathbf{T}^\alpha \mathbf{F}_\alpha^{T-1} & : & \text{first Piola-Kirchhoff stress tensor,} \\ \mathbf{S}^\alpha &= (\det \mathbf{F}_\alpha) \mathbf{F}_\alpha^{-1} \mathbf{T}^\alpha \mathbf{F}_\alpha^{T-1} & : & \text{second Piola-Kirchhoff stress tensor.} \end{aligned} \quad (3.35)$$

3.4 Balance relations

In continuum mechanics, the conservation of mechanical and thermodynamical quantities, in particular mass, linear momentum, momentum of momentum, energy and entropy, are introduced axiomatically. These axioms, which were originally developed for single-phasic materials, can be transferred to multi-constituent models with the help of Truesdell's three famous "metaphysical principles" of mixture theories (cf. Truesdell [113]):

1. *All properties of the mixture must be mathematical consequences of properties of the constituents.*
2. *So as to describe the motion of a constituent, we may in imagination isolate it from the rest of the mixture, provided we allow properly for the actions of the other constituents upon it.*

3. *The motion of the mixture is governed by the same equations as is a single body.*

This means, the balance relations hold for the total aggregate as well as for its single constituents. Hereby, an interaction between the constituents is allowed by the introduction of so-called production terms.

The fundamental structure of all balance relations, which is known as the master balance, is based on the idea that the temporal change of a mechanical or thermodynamical quantity can only be caused by the following three reasons:

- efflux of the mechanical quantity through the surface $\partial\mathcal{B}$ of the body,
- supply of the mechanical quantity from an external source and
- production of the mechanical quantity within the body.

Therefore, the global master balance equations of the overall aggregate, where Ψ (scalar-valued) and $\mathbf{\Psi}$ (vector-valued) are the respective mechanical quantities, reads:

$$\begin{aligned} \frac{d}{dt} \int_{\mathcal{B}} \Psi \, dv &= \int_{\partial\mathcal{B}} (\boldsymbol{\phi} \cdot \mathbf{n}) \, da + \int_{\mathcal{B}} \sigma \, dv + \int_{\mathcal{B}} \hat{\Psi} \, dv, \\ \frac{d}{dt} \int_{\mathcal{B}} \mathbf{\Psi} \, dv &= \int_{\partial\mathcal{B}} (\mathbf{\Phi} \mathbf{n}) \, da + \int_{\mathcal{B}} \boldsymbol{\sigma} \, dv + \int_{\mathcal{B}} \hat{\mathbf{\Psi}} \, dv. \end{aligned} \quad (3.36)$$

Therein, $\boldsymbol{\phi} \cdot \mathbf{n}$ and $\mathbf{\Phi} \mathbf{n}$ are the effluxes (action at the vicinity), σ and $\boldsymbol{\sigma}$ are the external supplies (action from the distance), and $\hat{\Psi}$ and $\hat{\mathbf{\Psi}}$ are the total productions of the respective mechanical quantity. As the production term describes the interaction with the surrounding of the system, this production term vanishes for a closed system, except for the entropy production. Applying the material time derivation to the left-hand sides and the Gaussian integral theorem to the surface part of the global master balance (3.36) yields the local forms of the balance relations for the overall aggregate:

$$\begin{aligned} \dot{\Psi} + \Psi \operatorname{div} \dot{\mathbf{x}} &= \operatorname{div} \boldsymbol{\phi} + \sigma + \hat{\Psi}, \\ \dot{\mathbf{\Psi}} + \mathbf{\Psi} \operatorname{div} \dot{\mathbf{x}} &= \operatorname{div} \mathbf{\Phi} + \boldsymbol{\sigma} + \hat{\mathbf{\Psi}}. \end{aligned} \quad (3.37)$$

Thereby, steady and steadily differentiable integrands are postulated.

Based on Truesdell's second metaphysical principle and analogously to (3.36) the global scalar and vectorial master balance relations follow for a particular constituent φ^α via

$$\begin{aligned} \frac{d_\alpha}{dt} \int_{\mathcal{B}} \Psi^\alpha \, dv &= \int_{\partial\mathcal{B}} (\boldsymbol{\phi}^\alpha \cdot \mathbf{n}) \, da + \int_{\mathcal{B}} \sigma^\alpha \, dv + \int_{\mathcal{B}} \hat{\Psi}^\alpha \, dv, \\ \frac{d_\alpha}{dt} \int_{\mathcal{B}} \mathbf{\Psi}^\alpha \, dv &= \int_{\partial\mathcal{B}} (\mathbf{\Phi}^\alpha \mathbf{n}) \, da + \int_{\mathcal{B}} \boldsymbol{\sigma}^\alpha \, dv + \int_{\mathcal{B}} \hat{\mathbf{\Psi}}^\alpha \, dv. \end{aligned} \quad (3.38)$$

Consequently, the corresponding local forms read:

$$\begin{aligned} (\Psi^\alpha)'_\alpha + \Psi^\alpha \operatorname{div} \dot{\mathbf{x}}_\alpha &= \operatorname{div} \phi^\alpha + \sigma^\alpha + \hat{\Psi}^\alpha, \\ (\Psi^\alpha)'_\alpha + \Psi^\alpha \operatorname{div} \dot{\mathbf{x}}_\alpha &= \operatorname{div} \Phi^\alpha + \sigma^\alpha + \hat{\Psi}^\alpha. \end{aligned} \quad (3.39)$$

As already mentioned, the interaction of the mechanical quantity between the regarded system and its surroundings can be described by the production term. In this context, the production term is used for multi-constituent models to describe the interaction between different constituents. With Truesdell's first metaphysical principle, which states that the sum of the partial balances is identical to the balance of the overall aggregate, the following relations can be found:

$$\begin{aligned} \Psi &= \sum_\alpha \Psi^\alpha, & \phi &= \sum_\alpha (\phi^\alpha - \Psi^\alpha \mathbf{d}_\alpha), & \sigma &= \sum_\alpha \sigma^\alpha, & \hat{\Psi} &= \sum_\alpha \hat{\Psi}^\alpha, \\ \Psi &= \sum_\alpha \Psi^\alpha, & \Phi &= \sum_\alpha (\Phi^\alpha - \Psi^\alpha \otimes \mathbf{d}_\alpha), & \sigma &= \sum_\alpha \sigma^\alpha, & \hat{\Psi} &= \sum_\alpha \hat{\Psi}^\alpha. \end{aligned} \quad (3.40)$$

Furthermore, except for the entropy production, the sum of the production terms must vanish which leads to constraints that also must be met by the process.

Balance of mass

Based on the axiomatic statement, that the mass M of a closed system stays constant, the balance of mass for the overall aggregate is introduced via

$$M = \int_{\mathcal{B}} \rho \, dv = \text{const.} \quad \rightarrow \quad \dot{M} = \frac{d}{dt} \int_{\mathcal{B}} \rho \, dv = 0, \quad (3.41)$$

where the observed mechanical quantity Ψ from the master balance is identified as the mass density ρ . Because there is neither any efflux or supply, and, as stated above, the production of mass is excluded for the overall body, no other term from the master balance occur here. However, to allow for mass transfer between different constituents, $\hat{\rho}^\alpha$ denotes the mass production per volume element. Thus, the mass balance of a single constituent reads

$$\frac{d_\alpha}{dt} \int_{\mathcal{B}} \rho^\alpha \, dv = \int_{\mathcal{B}} \hat{\rho}^\alpha \, dv. \quad (3.42)$$

With the correlations

$$\begin{aligned} \varphi : & \quad \Psi \rightarrow \rho, \quad \phi \rightarrow \mathbf{0}, \quad \sigma \rightarrow 0, \quad \hat{\Psi} \rightarrow 0, \\ \varphi^\alpha : & \quad \Psi^\alpha \rightarrow \rho^\alpha, \quad \phi^\alpha \rightarrow \mathbf{0}, \quad \sigma^\alpha \rightarrow 0, \quad \hat{\Psi}^\alpha \rightarrow \hat{\rho}^\alpha, \end{aligned} \quad (3.43)$$

the local forms of the mass balances for the overall body and the single constituent follow with (3.37)₁ and (3.39)₁, respectively:

$$\begin{aligned} \dot{\rho} + \rho \operatorname{div} \dot{\mathbf{x}} &= 0, \\ (\rho^\alpha)'_\alpha + \rho^\alpha \operatorname{div} \dot{\mathbf{x}}_\alpha &= \hat{\rho}^\alpha. \end{aligned} \quad (3.44)$$

From (3.40), it further follows that

$$\rho = \sum_{\alpha} \rho^{\alpha} \quad \text{and} \quad \sum_{\alpha} \hat{\rho}^{\alpha} = 0. \quad (3.45)$$

Balance of linear momentum

The axiomatic statement that the temporal change of momentum of a body

$$\frac{d}{dt} \int_{\mathcal{B}} \rho \dot{\mathbf{x}} dv = \int_{\partial \mathcal{B}} \mathbf{T} \mathbf{n} da + \int_{\mathcal{B}} \rho \mathbf{g} dv \quad (3.46)$$

is equivalent to the sum of the acting surface and body forces is basically Newton's second law. Therein, the observed mechanical quantity is the local momentum $\rho \dot{\mathbf{x}}$. Analogously, for the global momentum balance of the constituent φ^{α} , considering the additional momentum production $\hat{\mathbf{s}}^{\alpha}$, follows

$$\frac{d}{dt} \int_{\mathcal{B}} \rho^{\alpha} \dot{\mathbf{x}}_{\alpha} dv = \int_{\partial \mathcal{B}} \mathbf{T}^{\alpha} \mathbf{n} da + \int_{\mathcal{B}} \rho^{\alpha} \mathbf{g} dv + \int_{\mathcal{B}} \hat{\mathbf{s}}^{\alpha} dv, \quad (3.47)$$

with the local momentum $\rho^{\alpha} \dot{\mathbf{x}}_{\alpha}$. Thus, comparing (3.46) and (3.47) with the master balances (3.36)₂ and (3.38)₂, respectively, yields

$$\begin{aligned} \varphi : \quad \Psi &\rightarrow \rho \dot{\mathbf{x}}, & \Phi &\rightarrow \mathbf{T}, & \sigma &\rightarrow \rho \mathbf{g}, & \hat{\Psi} &\rightarrow \mathbf{0}, \\ \varphi^{\alpha} : \quad \Psi^{\alpha} &\rightarrow \rho^{\alpha} \dot{\mathbf{x}}_{\alpha}, & \Phi^{\alpha} &\rightarrow \mathbf{T}^{\alpha}, & \sigma^{\alpha} &\rightarrow \rho^{\alpha} \mathbf{g}, & \hat{\Psi}^{\alpha} &\rightarrow \hat{\mathbf{s}}^{\alpha}. \end{aligned} \quad (3.48)$$

These relations, the local master balances (3.37)₂ and (3.39)₂, and a reformulation of the left-hand side using the mass balance relations (3.44) yield the local momentum balances

$$\begin{aligned} \rho \ddot{\mathbf{x}} &= \operatorname{div} \mathbf{T} + \rho \mathbf{g} \quad \text{and} \\ \rho^{\alpha} \ddot{\mathbf{x}}_{\alpha} &= \operatorname{div} \mathbf{T}^{\alpha} + \rho^{\alpha} \mathbf{g} + \hat{\mathbf{p}}^{\alpha} \end{aligned} \quad (3.49)$$

of the overall aggregate φ and the constituent φ^{α} . The direct momentum production $\hat{\mathbf{p}}^{\alpha}$ is one part of the total momentum production

$$\hat{\mathbf{s}}^{\alpha} = \hat{\mathbf{p}}^{\alpha} + \hat{\rho}^{\alpha} \dot{\mathbf{x}}_{\alpha}. \quad (3.50)$$

The other part results from the mass transfer $\hat{\rho}^{\alpha}$ between the constituents. Keeping Truesdell's first principle in mind, a comparison of (3.48) and (3.40)₂, yields the following dependencies:

$$\begin{aligned} \dot{\mathbf{x}} &= \frac{1}{\rho} \sum_{\alpha} \rho^{\alpha} \dot{\mathbf{x}}_{\alpha}, & \mathbf{T} &= \sum_{\alpha} (\mathbf{T}^{\alpha} - \rho^{\alpha} \mathbf{d}_{\alpha} \otimes \mathbf{d}_{\alpha}), \\ \mathbf{g} &= \frac{1}{\rho} \sum_{\alpha} \rho^{\alpha} \mathbf{g}, & \mathbf{0} &= \sum_{\alpha} \hat{\mathbf{s}}^{\alpha} = \sum_{\alpha} (\hat{\mathbf{p}}^{\alpha} + \hat{\rho}^{\alpha} \dot{\mathbf{x}}_{\alpha}). \end{aligned} \quad (3.51)$$

Balance of moment of momentum

Based on the standard finding that $\mathbf{T} = \mathbf{T}^T$ for a single-constituent body, it can be shown with the balances of mass and moment of momentum that for non-polar materials (Cauchy continua) the Cauchy stress tensor of the constituents is symmetric (cf. Ehlers [40]):

$$\mathbf{T}^\alpha = (\mathbf{T}^\alpha)^T. \quad (3.52)$$

Balance of energy

In order to consider the thermal properties of a system, the energy balance is introduced via an axiomatic statement, which is also known as the first law of thermodynamics. It implies that the temporal change of the sum of the internal energy \mathcal{E} and the kinetic energy \mathcal{K} of a body is equivalent to the sum of the external mechanical power \mathcal{L} and the non-mechanical power \mathcal{Q} :

$$\frac{d}{dt} [\mathcal{E}(\mathcal{B}, t) + \mathcal{K}(\mathcal{B}, t)] = \mathcal{L}(\mathcal{B}, t) + \mathcal{Q}(\mathcal{B}, t). \quad (3.53)$$

Thus, it follows with

$$\begin{aligned} \mathcal{E} &= \int_{\mathcal{B}} \rho \varepsilon \, dv, & \mathcal{K} &= \int_{\mathcal{B}} \frac{1}{2} \rho \dot{\mathbf{x}} \cdot \dot{\mathbf{x}} \, dv, \\ \mathcal{L} &= \int_{\partial \mathcal{B}} (\mathbf{T}^T \dot{\mathbf{x}}) \cdot \mathbf{n} \, da + \int_{\mathcal{B}} \rho \mathbf{g} \cdot \dot{\mathbf{x}} \, dv, & \mathcal{Q} &= - \int_{\partial \mathcal{B}} \mathbf{q} \cdot \mathbf{n} \, da + \int_{\mathcal{B}} \rho r \, dv \end{aligned} \quad (3.54)$$

for the balance of energy of the overall aggregate φ :

$$\frac{d}{dt} \int_{\mathcal{B}} \rho (\varepsilon + \frac{1}{2} \dot{\mathbf{x}} \cdot \dot{\mathbf{x}}) \, dv = \int_{\partial \mathcal{B}} (\mathbf{T}^T \dot{\mathbf{x}} - \mathbf{q}) \cdot \mathbf{n} \, da + \int_{\mathcal{B}} \rho (\mathbf{g} \cdot \dot{\mathbf{x}} + r) \, dv. \quad (3.55)$$

The heat conduction \mathbf{q} through the surface of the body is reverse oriented compared with the introduction of the efflux in the master balance, therefore the negative sign is deployed. Moreover, r is the non-mechanical action from the distance. An analogous procedure provides the global energy balance for a constituent φ^α , viz.:

$$\begin{aligned} \frac{d_\alpha}{dt} \int_{\mathcal{B}} \rho^\alpha (\varepsilon^\alpha + \frac{1}{2} \dot{\mathbf{x}}_\alpha \cdot \dot{\mathbf{x}}_\alpha) \, dv &= \int_{\partial \mathcal{B}} [(\mathbf{T}^\alpha)^T \dot{\mathbf{x}}_\alpha - \mathbf{q}^\alpha] \cdot \mathbf{n} \, da + \\ &+ \int_{\mathcal{B}} \rho^\alpha (\mathbf{g} \cdot \dot{\mathbf{x}}_\alpha + r^\alpha) \, dv + \int_{\mathcal{B}} \hat{e}^\alpha \, dv \end{aligned} \quad (3.56)$$

with the total energy production \hat{e} . Thus, comparing (3.55) and (3.56) with the master balance (3.36)₁ and (3.38)₁ respectively, yields

$$\begin{aligned} \varphi : \quad & \begin{cases} \Psi \rightarrow \rho (\varepsilon + \frac{1}{2} \dot{\mathbf{x}} \cdot \dot{\mathbf{x}}), & \phi \rightarrow \mathbf{T}^T \dot{\mathbf{x}} - \mathbf{q}, \\ \sigma \rightarrow \rho (\mathbf{g} \cdot \dot{\mathbf{x}} + r), & \hat{\Psi} \rightarrow 0, \end{cases} \\ \varphi^\alpha : \quad & \begin{cases} \Psi^\alpha \rightarrow \rho^\alpha (\varepsilon^\alpha + \frac{1}{2} \dot{\mathbf{x}}_\alpha \cdot \dot{\mathbf{x}}_\alpha), & \phi^\alpha \rightarrow (\mathbf{T}^\alpha)^T \dot{\mathbf{x}}_\alpha - \mathbf{q}^\alpha, \\ \sigma^\alpha \rightarrow \rho^\alpha (\mathbf{g} \cdot \dot{\mathbf{x}}_\alpha + r^\alpha), & \hat{\Psi}^\alpha \rightarrow \hat{e}^\alpha. \end{cases} \end{aligned} \quad (3.57)$$

Inserting (3.57) into the local master balance equations (3.37)₁ and (3.39)₁ and using the already known balance equations for mass and linear momentum yields the local form of the energy balance relation for the overall aggregate φ and the constituent φ^α :

$$\begin{aligned}\rho \dot{\varepsilon} &= \mathbf{T} \cdot \mathbf{L} - \operatorname{div} \mathbf{q} + \rho r, \\ \rho^\alpha (\varepsilon^\alpha)'_\alpha &= \mathbf{T}^\alpha \cdot \mathbf{L}_\alpha - \operatorname{div} \mathbf{q}^\alpha + \rho^\alpha r^\alpha + \hat{\varepsilon}^\alpha.\end{aligned}\quad (3.58)$$

Therein, the direct energy production $\hat{\varepsilon}^\alpha$ is a part of the total momentum production

$$\hat{e}^\alpha = \hat{\varepsilon}^\alpha + \hat{\mathbf{p}}^\alpha \cdot \dot{\mathbf{x}}_\alpha + \hat{\rho}^\alpha \left(\varepsilon + \frac{1}{2} \dot{\mathbf{x}}_\alpha \cdot \dot{\mathbf{x}}_\alpha \right).\quad (3.59)$$

The other parts are resulting from the mass and momentum transfer between the constituents. Furthermore, with (3.40)₁ and (3.57) the following relationships hold

$$\begin{aligned}\varepsilon &= \frac{1}{\rho} \sum_\alpha \rho^\alpha \left(\varepsilon^\alpha + \frac{1}{2} \mathbf{d}_\alpha \cdot \mathbf{d}_\alpha \right), \\ \mathbf{q} &= \sum_\alpha \left[\mathbf{q}^\alpha - (\mathbf{T}^\alpha)^T \mathbf{d}_\alpha + \rho^\alpha \varepsilon^\alpha \mathbf{d}_\alpha + \frac{1}{2} \rho^\alpha (\mathbf{d}_\alpha \cdot \mathbf{d}_\alpha) \mathbf{d}_\alpha \right], \\ r &= \frac{1}{\rho} \sum_\alpha \rho^\alpha (r^\alpha + \mathbf{g} \cdot \mathbf{d}_\alpha), \\ 0 &= \sum_\alpha \hat{e}^\alpha = \sum_\alpha \left[\hat{\varepsilon}^\alpha + \hat{\mathbf{p}}^\alpha \cdot \dot{\mathbf{x}}_\alpha + \hat{\rho}^\alpha \left(\varepsilon + \frac{1}{2} \dot{\mathbf{x}}_\alpha \cdot \dot{\mathbf{x}}_\alpha \right) \right].\end{aligned}\quad (3.60)$$

For the interpretation of these terms see Ehlers [40].

Balance of entropy

In order to balance the entropy of a body, it is axiomatically stated that the temporal change of the entropy of a body \mathcal{B} equals the sum of external change of entropy (efflux and supply) and the internal entropy production:

$$\frac{d}{dt} \int_{\mathcal{B}} \rho \eta \, dv = \int_{\partial \mathcal{B}} \boldsymbol{\phi}_\eta \cdot \mathbf{n} \, da + \int_{\mathcal{B}} \sigma_\eta \, dv + \int_{\mathcal{B}} \hat{\eta} \, dv.\quad (3.61)$$

Here, η is the mass-specific entropy and $\hat{\eta}$ the volume-specific entropy production. The efflux $\boldsymbol{\phi}_\eta$ and the supply σ_η are commonly given by means of an a-priori constitutive assumption via

$$\boldsymbol{\phi}_\eta = -\frac{\mathbf{q}}{\theta} \quad \text{and} \quad \sigma_\eta = \frac{\rho r}{\theta}.\quad (3.62)$$

The corresponding global entropy balance of a constituent φ^α reads

$$\frac{d_\alpha}{dt} \int_{\mathcal{B}} \rho^\alpha \eta^\alpha \, dv = \int_{\partial \mathcal{B}} \boldsymbol{\phi}_\eta^\alpha \cdot \mathbf{n} \, da + \int_{\mathcal{B}} \sigma_\eta^\alpha \, dv + \int_{\mathcal{B}} \hat{\eta}^\alpha \, dv\quad (3.63)$$

with

$$\boldsymbol{\phi}_\eta^\alpha = -\frac{\mathbf{q}^\alpha}{\theta^\alpha} \quad \text{and} \quad \sigma_\eta^\alpha = \frac{\rho^\alpha r^\alpha}{\theta^\alpha}.\quad (3.64)$$

In (3.62) and (3.64), $\theta > 0$ and $\theta^\alpha > 0$ are the absolute Kelvin's temperatures of the overall aggregate φ and the constituent φ^α , respectively. Comparing (3.61) and (3.63) with the master balances (3.36)₁ and (3.38)₁ yields

$$\begin{aligned} \varphi : \quad \psi &\rightarrow \rho \eta, & \phi &\rightarrow -\frac{\mathbf{q}}{\theta}, & \sigma &\rightarrow \frac{\rho r}{\theta}, & \hat{\psi} &\rightarrow \hat{\eta}, \\ \varphi^\alpha : \quad \psi^\alpha &\rightarrow \rho^\alpha \eta^\alpha, & \phi^\alpha &\rightarrow -\frac{\mathbf{q}^\alpha}{\theta^\alpha}, & \sigma^\alpha &\rightarrow \frac{\rho^\alpha r^\alpha}{\theta^\alpha}, & \hat{\psi}^\alpha &\rightarrow \hat{\eta}^\alpha. \end{aligned} \quad (3.65)$$

Inserting (3.65) into the local master balance equations (3.37)₁ and (3.39)₁ and further using the local mass balances (3.44) yields the local form of the entropy balance for the overall aggregate φ and the constituent φ^α :

$$\begin{aligned} \rho \dot{\eta} &= -\operatorname{div} \frac{\mathbf{q}}{\theta} + \frac{\rho r}{\theta} + \hat{\eta}, \\ \rho^\alpha (\eta^\alpha)'_\alpha &= -\operatorname{div} \frac{\mathbf{q}^\alpha}{\theta^\alpha} + \frac{\rho^\alpha r^\alpha}{\theta^\alpha} + \hat{\zeta}^\alpha. \end{aligned} \quad (3.66)$$

Therein, the direct entropy production $\hat{\zeta}^\alpha$ is a part of the total entropy production

$$\hat{\eta}^\alpha = \hat{\zeta}^\alpha + \hat{\rho}^\alpha \eta^\alpha. \quad (3.67)$$

The entropy balance is not required as a governing equation in the sense of the closure problem of continuum mechanics. However, it is very important, as it is able to provide conditions, that must be satisfied by all constitutive model assumptions to ensure a thermodynamically consistent material behaviour. This restriction is equivalent to the second law of thermodynamics, which states that production of entropy in a closed system can never be negative. It is therefore necessary to postulate that

$$\hat{\eta} = \sum_\alpha \hat{\eta}^\alpha = \sum_\alpha [\rho^\alpha (\eta^\alpha)'_\alpha + \hat{\rho}^\alpha \eta^\alpha + \operatorname{div} \frac{\mathbf{q}^\alpha}{\theta^\alpha} - \frac{\rho^\alpha r^\alpha}{\theta^\alpha}] \geq 0. \quad (3.68)$$

By means of the energy balance (3.58)₂ and using the definition of the Helmholtz free energy

$$\psi^\alpha := \varepsilon^\alpha - \theta^\alpha \eta^\alpha, \quad (3.69)$$

(3.68) can be reformulated to the so-called Clausius-Duhem inequality, viz.:

$$\begin{aligned} \sum_\alpha \frac{1}{\theta^\alpha} \{ \mathbf{T}^\alpha \cdot \mathbf{L}_\alpha - \rho^\alpha [(\psi^\alpha)'_\alpha + (\theta^\alpha)'_\alpha \eta^\alpha] - \hat{\mathbf{p}}^\alpha \cdot \dot{\mathbf{x}}_\alpha - \\ - \hat{\rho}^\alpha (\psi^\alpha + \frac{1}{2} \dot{\mathbf{x}}_\alpha \cdot \dot{\mathbf{x}}_\alpha) - \frac{\mathbf{q}^\alpha}{\theta^\alpha} \cdot \operatorname{grad} \theta^\alpha + \hat{e}^\alpha \} \geq 0. \end{aligned} \quad (3.70)$$

As previously mentioned, this inequality leads to restrictions for the constitutive setting which is discussed in detail in Chapter 4.

Chapter 4:

Constitutive modelling

Based on the continuum-mechanical fundamentals, presented in the preceding chapter, it is possible to develop a manifold of models to describe a variety of possible material behaviour. Within this chapter, a particular model for the simulation of geothermal reservoirs is presented. To reduce the complexity of the governing equations it is reasonable to apply some preliminary simplifications that are meaningful in the context of the considered application. Furthermore, as already mentioned, the satisfaction of the Clausius-Duhem inequality (3.70) is necessary to obtain a thermodynamically consistent material behaviour. Finally, constitutive assumptions related to the material behaviour are needed in order to close the continuum-mechanical problem and receive the final set of governing equations.

4.1 Preliminary model assumptions

A geothermal reservoir consists of two different material components, namely rock φ^S and water φ^F . These two components are the constituents of the considered TPM model. Assuming that there is neither any vacant space nor other materials that have to be concerned, the saturation condition (3.3) reads

$$n^S + n^F = 1. \quad (4.1)$$

Here, n^S and n^F are the volume fractions occupied by the rock (solidity) and the water (porosity), respectively. Both materials can be considered as materially incompressible, which means that the density of the material is not dependent on any acting mechanical load. The occurring temperatures in a geothermal reservoir may reach from about 300 K to around 500 K. However, since the volumetric thermal expansion coefficient of the rock ($2.37 \cdot 10^{-5} \text{ K}^{-1}$ for granite¹) is much smaller than the volumetric thermal expansion coefficient of $7 \cdot 10^{-4} \text{ K}^{-1}$ for water², the thermal expansion of the rock is further neglected within this work. Consequently, it follows for the real densities:

$$\rho^{SR} \approx \text{const.} \quad \text{and} \quad \rho^{FR} = \rho^{FR}(\theta^F). \quad (4.2)$$

Nevertheless, it is noted that the partial density ρ^S may change due to variations of the volume fractions, cf. (3.5). Moreover, at these high temperatures, the high pressure between 10 and 100 MPa within the reservoir ensures that the water remains liquid during the considered processes, cf. Figure 4.1. Furthermore, a mass exchange between the constituents can be excluded. Therefore, the mass production term vanishes:

$$\hat{\rho}^\alpha = 0. \quad (4.3)$$

¹http://www.engineeringtoolbox.com/linear-expansion-coefficients-d_95.html - Retrieved 1. 5. 2016.

²<http://physics.info/expansion> - Retrieved 25. 3. 2015.

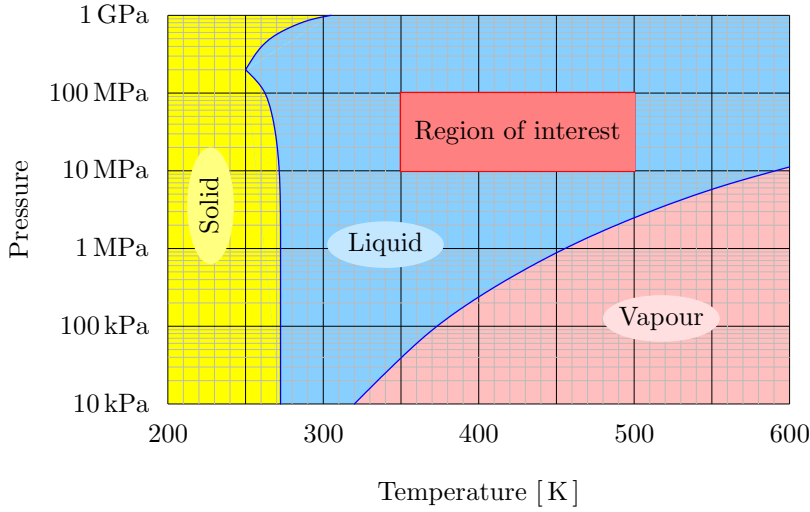


Figure 4.1: Pressure–temperature phase diagram of water.

In addition, assuming a quasi-static behaviour, the influence of the acceleration is very small and therefore neglected in the following, viz.:

$$\ddot{\mathbf{x}} = \mathbf{0} \quad \text{and} \quad \ddot{\mathbf{x}}_\alpha = \mathbf{0}. \quad (4.4)$$

4.2 Evaluation of the entropy inequality

4.2.1 Thermodynamical principles

According to Ehlers [42], for a TPM material model with non-isothermal constituents, the fundamental set

$$\begin{aligned} \mathcal{V} = \{ & \theta^\alpha, \text{grad } \theta^\alpha, n^\alpha, \text{grad } n^\alpha, \rho^{\alpha R}, \text{grad } \rho^{\alpha R}, \\ & \mathbf{F}_\alpha, \text{Grad}_\alpha \mathbf{F}_\alpha, \dot{\mathbf{x}}_\alpha, \text{Grad}_\alpha \dot{\mathbf{x}}_\alpha, \mathbf{X}_\alpha \} \end{aligned} \quad (4.5)$$

of process variables is given. This means, the process can depend on the temperature, volume fraction, density, deformation, actual velocity and their appropriate gradients. Furthermore, the initial position \mathbf{X}_α may be needed to describe inhomogeneous material behaviour. The response functions

$$\mathcal{R} = \{ \psi^S, \psi^F, \mathbf{T}_E^S, \mathbf{T}_E^F, \hat{\mathbf{p}}_E^F, \hat{\boldsymbol{\varepsilon}}^F, \mathbf{q}^S, \mathbf{q}^F \} \quad (4.6)$$

cannot be found via the balance equations or the actual state of the system. It is rather necessary to constitutively define reasonable relations. According to this choice of constitutive dependencies, the material behaviour is specified and, moreover, the set of independent process variables is reduced thereby. For a constant real solid density, the mass balance of the solid reduces to the volume balance

$$(n^S)'_S + n^S \text{div } \dot{\mathbf{x}}_S = 0 \quad (4.7)$$

and, after integration, it follows an equation to determine the actual solid volume fraction

$$n^S = n_{0S}^S (\det \mathbf{F}_S)^{-1}. \quad (4.8)$$

Therefore, the actual volume fraction of the solid depends on the initial volume fraction n_{0S}^S and the deformation gradient \mathbf{F}_S , such that, in combination with the saturation condition, the volume fractions n^α and their respective gradients can be eliminated from the set of independent process variables. Assuming an isotropic, thermal expansion of the fluid with the constant thermal expansion coefficient α^F yields, as it was already described by Lu & Pister [85], for the real density of the fluid

$$\rho^{FR} = \rho^{FR}(\theta^F) = \rho_{0S}^{FR} e^{-3\alpha^F(\theta^F - \theta_0^F)}, \quad (4.9)$$

where θ_0^F is the initial fluid temperature. Thus, and remembering the constant solid density, also the real densities $\rho^{\alpha R}$ and their gradients can be eliminated from the set (4.5) of process variables.

Remark: Starting from the definition of the thermal expansion coefficient

$$\alpha^F := \frac{1}{L^F} \frac{\partial L^F}{\partial \theta^F} = \frac{\partial (\ln L^F)}{\partial \theta^F}, \quad (4.10)$$

where L^F is the one-dimensional (1-d) measure of length of the fluid for a certain temperature, integration yields the following relation:

$$\alpha^F(\theta^F - \theta_0^F) = \ln \frac{L^F(\theta^F)}{L^F(\theta_0^F)}. \quad (4.11)$$

After reformulation, the change in length can be given as a function of the change in temperature, namely

$$\frac{L^F(\theta^F)}{L^F(\theta_0^F)} = e^{\alpha^F(\theta^F - \theta_0^F)}. \quad (4.12)$$

Considering isotropic materials, it follows directly for the 3-d volumetric expansion

$$\frac{V^F(\theta^F)}{V^F(\theta_0^F)} = e^{3\alpha^F(\theta^F - \theta_0^F)}, \quad (4.13)$$

since $V^F(\theta^F) = [L^F(\theta^F)]^3$. Therefore, with the constant fluid mass M^F , and with $V^F = M^F/\rho^{FR}$, the temperature dependency of the density (4.9) is found. Note in passing that sometimes $3\alpha^F$ is also called the volumetric thermal expansion coefficient α_V^F .

According to the principle of frame indifference as described by Truesdell & Noll [114], a physical phenomenon is independent of the observer's position. Therefore, the velocity $\dot{\mathbf{x}}_\alpha$ and its respective gradient $\text{Grad}_\alpha \dot{\mathbf{x}}_\alpha$ are replaced by the material frame independent seepage velocity \mathbf{w}_F and \mathbf{D}_α , respectively, cf. de Boer & Ehlers [20]. Moreover, the deformation gradient \mathbf{F}_S , which is also not frame independent, is replaced by the objective

right Cauchy-Green deformation tensor \mathbf{C}_S . For the solid constituent the symmetric part \mathbf{D}_S of the spatial velocity gradient is not needed, because only elastic material behaviour is assumed. Due to the fact that only homogeneous, anisotropic material behaviour is considered, the material response is independent from the initial position \mathbf{X}_S . For more details concerning such issues, the interested reader is referred to Ehlers [42]. As a consequence, for the description of the specific material behaviour, the set of process variables is reduced to

$$\mathcal{S} = \{\theta^S, \text{grad } \theta^S, \theta^F, \text{grad } \theta^F, \mathbf{C}_S, \text{Grad}_S \mathbf{C}_S, \mathbf{w}_F, \mathbf{D}_F\}. \quad (4.14)$$

4.2.2 The saturation condition and the effective stress principle

In order to consider the restrictions from the saturation condition within the thermodynamical process, the time derivative of this condition with respect to the solid deformation

$$n^S + n^F = 1 \quad \rightarrow \quad (n^S)'_S + (n^F)'_S = 0 \quad (4.15)$$

is multiplied by the Lagrange multiplier Λ and added to the Clausius-Duhem inequality (3.70).

With the mass balances (3.44)₂ for the constituents φ^S and φ^F , the time derivatives of the volume fractions are obtained via

$$\begin{aligned} (n^S)'_S &= -n^S \text{div } \dot{\mathbf{x}}_S, \\ (n^F)'_F &= -n^F \text{div } \dot{\mathbf{x}}_F - \frac{n^F}{\rho^{FR}} (\rho^{FR})'_F \\ &= -n^F \text{div } \dot{\mathbf{x}}_F + 3\alpha^F n^F (\theta^F)'_F. \end{aligned} \quad (4.16)$$

Therein, according to (4.9), the material time derivative of the real fluid density reads

$$(\rho^{FR})'_F = \frac{\partial \rho^{FR}}{\partial \theta^F} (\theta^F)'_F = -3\alpha^F \rho^{FR} (\theta^F)'_F. \quad (4.17)$$

Considering the relation

$$(\cdot)'_S = (\cdot)'_F - \text{grad}(\cdot) \cdot \mathbf{w}_F, \quad (4.18)$$

deduced from (3.11), it follows for (4.15) in combination with (4.16):

$$n^S \mathbf{L}_S \cdot \mathbf{I} + n^F \mathbf{L}_F \cdot \mathbf{I} - 3\alpha^F n^F (\theta^F)'_F + \text{grad } n^F \cdot \mathbf{w}_F = 0. \quad (4.19)$$

Due to the fact that mass production is excluded, the Clausius-Duhem inequality (3.70) for the biphasic model reads

$$\begin{aligned} &\mathbf{T}^S \cdot \mathbf{L}_S + \frac{\theta^S}{\theta^F} \mathbf{T}^F \cdot \mathbf{L}_F - \rho^S [(\psi^S)'_S + (\theta^S)'_S \eta^S] - \\ & - \frac{\theta^S}{\theta^F} \rho^F [(\psi^F)'_F + (\theta^F)'_F \eta^F] - \frac{1}{\theta^S} \mathbf{q}^S \cdot \text{grad } \theta^S - \frac{\theta^S}{(\theta^F)^2} \mathbf{q}^F \cdot \text{grad } \theta^F - \\ & - \hat{\mathbf{p}}^S \cdot \dot{\mathbf{x}}_S - \frac{\theta^S}{\theta^F} \hat{\mathbf{p}}^F \cdot \dot{\mathbf{x}}_F + \hat{e}^S + \frac{\theta^S}{\theta^F} \hat{e}^F \geq 0. \end{aligned} \quad (4.20)$$

It follows further with (3.51)₄, (3.60)₄ and the definition of the seepage velocity (3.15):

$$\begin{aligned} & \mathbf{T}^S \cdot \mathbf{L}_S + \frac{\theta^S}{\theta^F} \mathbf{T}^F \cdot \mathbf{L}_F - \rho^S [(\psi^S)'_S + (\theta^S)'_S \eta^S] - \\ & - \frac{\theta^S}{\theta^F} \rho^F [(\psi^F)'_F + (\theta^F)'_F \eta^F] - \frac{1}{\theta^S} \mathbf{q}^S \cdot \text{grad } \theta^S - \frac{\theta^S}{(\theta^F)^2} \mathbf{q}^F \cdot \text{grad } \theta^F - \\ & - \hat{\mathbf{p}}^F \cdot \mathbf{w}_F + \hat{\varepsilon}^F \left(\frac{\theta^S}{\theta^F} - 1 \right) \geq 0. \end{aligned} \quad (4.21)$$

Thus, multiplying (4.19) with the Lagrange multiplier Λ and adding the result to the entropy inequality (4.21) yields

$$\begin{aligned} & [\mathbf{T}^S + \Lambda n^S \mathbf{I}] \cdot \mathbf{L}_S + \left[\frac{\theta^S}{\theta^F} \mathbf{T}^F + \Lambda n^F \mathbf{I} \right] \cdot \mathbf{L}_F - \rho^S [(\psi^S)'_S + (\theta^S)'_S \eta^S] - \\ & - \frac{\theta^S}{\theta^F} \rho^F (\theta^F)'_F \left[\eta^F + \Lambda \frac{\theta^F}{\theta^S} \frac{3 \alpha^F}{\rho^{FR}} \right] - [\hat{\mathbf{p}}^F - \Lambda \text{grad } n^F] \cdot \mathbf{w}_F - \\ & - \frac{\theta^S}{\theta^F} \rho^F (\psi^F)'_F - \frac{1}{\theta^S} \mathbf{q}^S \cdot \text{grad } \theta^S - \frac{\theta^S}{(\theta^F)^2} \mathbf{q}^F \cdot \text{grad } \theta^F + \hat{\varepsilon}^F \left(\frac{\theta^S}{\theta^F} - 1 \right) \geq 0. \end{aligned} \quad (4.22)$$

Introducing the so-called extra quantities

$$\begin{aligned} \mathbf{T}_E^S & := \mathbf{T}^S + \Lambda n^S \mathbf{I}, & \mathbf{T}_E^F & := \frac{\theta^S}{\theta^F} \mathbf{T}^F + \Lambda n^F \mathbf{I}, \\ \hat{\mathbf{p}}_E^F & := \hat{\mathbf{p}}^F - \Lambda \text{grad } n^F, & \eta_E^F & := \eta^F + \Lambda \frac{\theta^F}{\theta^S} \frac{3 \alpha^F}{\rho^{FR}}, \end{aligned} \quad (4.23)$$

the entropy inequality (4.22) reads

$$\begin{aligned} & \mathbf{T}_E^S \cdot \mathbf{L}_S + \mathbf{T}_E^F \cdot \mathbf{L}_F - \rho^S [(\psi^S)'_S + (\theta^S)'_S \eta^S] - \frac{\theta^S}{\theta^F} \rho^F [(\psi^F)'_F + (\theta^F)'_F \eta_E^F] - \\ & - \hat{\mathbf{p}}_E^F \cdot \mathbf{w}_F - \frac{1}{\theta^S} \mathbf{q}^S \cdot \text{grad } \theta^S - \frac{\theta^S}{(\theta^F)^2} \mathbf{q}^F \cdot \text{grad } \theta^F + \hat{\varepsilon}^F \left(\frac{\theta^S}{\theta^F} - 1 \right) \geq 0. \end{aligned} \quad (4.24)$$

4.2.3 Thermodynamical restrictions

Following the principle of phase separation (cf. Ehlers [42]), the Helmholtz free energy ψ^α of the constituent φ^α depends merely on the non-dissipative process variables of the constituent itself. Therefore, variables describing velocities are excluded. Moreover, a further evaluation would show that the Helmholtz free energy is independent of the gradients $\text{grad } \theta^\alpha$ and $\text{Grad}_S \mathbf{C}_S$, see Ghadiani [65]. Hence, the dependencies of the Helmholtz free energies of the considered solid and fluid constituents are

$$\begin{aligned} \psi^S & := \psi^S(\theta^S, \mathbf{C}_S), \\ \psi^F & := \psi^F(\theta^F). \end{aligned} \quad (4.25)$$

Thus, with (3.28) the appropriate time derivatives of the free energies read

$$\begin{aligned} (\psi^S)'_S &= \frac{\partial \psi^S}{\partial \theta^S} (\theta^S)'_S + 2 \mathbf{F}_S \frac{\partial \psi^S}{\partial \mathbf{C}_S} \mathbf{F}_S^T \cdot \mathbf{D}_S, \\ (\psi^F)'_F &= \frac{\partial \psi^F}{\partial \theta^F} (\theta^F)'_F. \end{aligned} \quad (4.26)$$

Inserting (4.26) into (4.24) while considering symmetric stress tensors, which means $\mathbf{T}_E^\alpha \cdot \mathbf{L}_\alpha = \mathbf{T}_E^\alpha \cdot \mathbf{D}_\alpha$, yields

$$\begin{aligned} & [\mathbf{T}_E^S - 2 \rho^S \mathbf{F}_S \frac{\partial \psi^S}{\partial \mathbf{C}_S} \mathbf{F}_S^T] \cdot \mathbf{D}_S + \mathbf{T}_E^F \cdot \mathbf{D}_F - \\ & - [\eta^S + \frac{\partial \psi^S}{\partial \theta^S}] \rho^S (\theta^S)'_S - [\eta_E^F + \frac{\partial \psi^F}{\partial \theta^F}] \frac{\theta^S}{\theta^F} \rho^F (\theta^F)'_F - \hat{\mathbf{p}}_E^F \cdot \mathbf{w}_F - \\ & - \frac{1}{\theta^S} \mathbf{q}^S \cdot \text{grad } \theta^S - \frac{\theta^S}{(\theta^F)^2} \mathbf{q}^F \cdot \text{grad } \theta^F + \hat{\varepsilon}^F (\frac{\theta^S}{\theta^F} - 1) \geq 0. \end{aligned} \quad (4.27)$$

Further evaluation of the entropy inequality is carried out according to the procedure of Coleman & Noll [29]. By doing so, the entropy inequality is divided into an equilibrium part

$$[\mathbf{T}_E^S - 2 \rho^S \mathbf{F}_S \frac{\partial \psi^S}{\partial \mathbf{C}_S} \mathbf{F}_S^T] \cdot \mathbf{D}_S - [\eta^S + \frac{\partial \psi^S}{\partial \theta^S}] \rho^S (\theta^S)'_S - [\eta_E^F + \frac{\partial \psi^F}{\partial \theta^F}] \frac{\theta^S}{\theta^F} \rho^F (\theta^F)'_F = 0, \quad (4.28)$$

and a non-equilibrium, dissipation part

$$\begin{aligned} \mathcal{D} &= \mathbf{T}_E^F \cdot \mathbf{D}_F - \hat{\mathbf{p}}_E^F \cdot \mathbf{w}_F - \frac{1}{\theta^S} \mathbf{q}^S \cdot \text{grad } \theta^S - \\ & - \frac{\theta^S}{(\theta^F)^2} \mathbf{q}^F \cdot \text{grad } \theta^F + \hat{\varepsilon}^F \frac{1}{\theta^F} (\theta^S - \theta^F) \geq 0. \end{aligned} \quad (4.29)$$

As a sufficient condition for the satisfaction of (4.28) and (4.29), each term of the non-equilibrium part has to be greater or equal to zero and all equilibrium terms are claimed to be equal to zero. These conditions must hold for arbitrary values of the process variables \mathbf{D}_S , \mathbf{D}_F , $(\theta^S)'_S$, $(\theta^F)'_F$, \mathbf{w}_F , $\text{grad } \theta^S$ and $\text{grad } \theta^F$ and for an arbitrary temperature difference $(\theta^S - \theta^F)$. Hence, the following restrictions from the equilibrium part can be found:

$$\begin{aligned} \mathbf{T}_E^S - 2 \rho^S \mathbf{F}_S \frac{\partial \psi^S}{\partial \mathbf{C}_S} \mathbf{F}_S^T = \mathbf{0} & \quad \rightarrow \quad \mathbf{T}_E^S = 2 \rho^S \mathbf{F}_S \frac{\partial \psi^S}{\partial \mathbf{C}_S} \mathbf{F}_S^T \\ \eta^S + \frac{\partial \psi^S}{\partial \theta^S} = 0 & \quad \rightarrow \quad \eta^S = - \frac{\partial \psi^S}{\partial \theta^S}, \\ \eta_E^F + \frac{\partial \psi^F}{\partial \theta^F} = 0 & \quad \rightarrow \quad \eta_E^F = - \frac{\partial \psi^F}{\partial \theta^F}. \end{aligned} \quad (4.30)$$

By the arguments of a dimensional analysis (cf. Ehlers *et al.* [46]), the divergence of the fluid friction stress $\text{div } \mathbf{T}_E^F$ is negligibly small compared to the fluid extra momentum production $\hat{\mathbf{p}}_E^F$, such that

$$\text{div } \mathbf{T}_E^F \ll \hat{\mathbf{p}}_E^F \quad \rightarrow \quad \mathbf{T}_E^F \approx \mathbf{0}. \quad (4.31)$$

In order to satisfy the condition (4.29) the following constitutive relations are chosen:

$$\begin{aligned}
\hat{\mathbf{p}}_E^F &=: -\mathbf{S}^{FS} \mathbf{w}_F, \\
\mathbf{q}^S &=: -\mathbf{H}^S \text{grad } \theta^S, \\
\mathbf{q}^F &=: -\mathbf{H}^F \text{grad } \theta^F, \\
\hat{\varepsilon}^F &=: k_\theta^\varepsilon (\theta^S - \theta^F).
\end{aligned} \tag{4.32}$$

Therein, \mathbf{S}^{FS} is a positive definite tensor that describes the friction between the constituents due to their relative motion. In the sense of Fourier's law of heat conduction, \mathbf{H}^α is a positive definite, partial heat conductivity tensor of the corresponding constituent. Finally, k_θ^ε is a positive volume-specific heat transfer coefficient.

Identification of the Lagrange multiplier

Based on the constitutive statement for the definition of the partial fluid stress tensor

$$\mathbf{T}^F =: -n^F p \mathbf{I}, \tag{4.33}$$

with a pore pressure p , the definition of the fluid extra stress (4.23)₂ and the assumption of its negligibility (4.31), yield the identification of the Lagrange multiplier:

$$\mathbf{T}^F = -n^F \frac{\theta^F}{\theta^S} \Lambda \mathbf{I} \quad \rightarrow \quad \Lambda = \frac{\theta^S}{\theta^F} p. \tag{4.34}$$

Therefore, according to (4.23), it follows for the extra quantities:

$$\begin{aligned}
\mathbf{T}_E^S &= \mathbf{T}^S + \frac{\theta^S}{\theta^F} n^S p \mathbf{I}, \\
\hat{\mathbf{p}}_E^F &= \hat{\mathbf{p}}^F - \frac{\theta^S}{\theta^F} p \text{grad } n^F, \\
\eta_E^F &= \eta^F + p \frac{3\alpha^F}{\rho^{FR}}.
\end{aligned} \tag{4.35}$$

It is also conceivable to use other approaches for the determination of the Lagrange multiplier. For example, the overall stress may be considered under hydrostatic pressure in an undeformed state:

$$\mathbf{T} =: -p^{FR} \mathbf{I}. \tag{4.36}$$

For this static conditions, the velocities $\dot{\mathbf{x}}_\alpha$ vanish and, therefore, also the term $\rho^\alpha \mathbf{d}_\alpha \otimes \mathbf{d}_\alpha$. Consequently, according to (3.51), the partial stress tensors \mathbf{T}^α add up to the overall stress tensor \mathbf{T} . This yields

$$\mathbf{T}^S + \mathbf{T}^F = -p^{FR} \mathbf{I}. \tag{4.37}$$

Thus, with (4.23) it follows for the effective pore pressure

$$p^{FR} = (n^S + \frac{\theta^F}{\theta^S} n^F) \Lambda \tag{4.38}$$

and, therefore, the Lagrange multiplier reads

$$\Lambda = \frac{\theta^S}{\theta^S n^S + \theta^F n^F} p^{FR}. \quad (4.39)$$

This yields the relation between the pressures p and p^{FR} :

$$p = \frac{\theta^F}{\theta^S n^S + \theta^F n^F} p^{FR}. \quad (4.40)$$

In the further course of this work, the pressure p is used. However, it would be possible at any time to use the effective pore pressure p^{FR} via an appropriate conversion. Note that for $\theta^S = \theta^F$ the pressures are equal.

4.3 The fluid constituent

4.3.1 Direct momentum production and Darcy's fluid flow

The constitutive definition of the fluid extra momentum production, which is actually the momentum exchange between the constituents, should satisfy several physical effects. In particular, for an increasing partial viscosity $n^F \mu^{FR}$ or filter velocity $n^F \mathbf{w}_F$, a higher momentum exchange is expected. Whereas, an increasing permeability should lead to a smaller momentum production. Therefore, the extra momentum production is introduced via

$$\hat{\mathbf{p}}_E^F = -\mathbf{S}^{FS} \mathbf{w}_F = -n^F \mu^{FR} (\mathbf{K}^S)^{-1} n^F \mathbf{w}_F = -\frac{\mu^{FR}}{K^S} (n^F)^2 \mathbf{w}_F, \quad (4.41)$$

$$\text{where} \quad \mathbf{K}^S = K^S \mathbf{I}.$$

Therein, $\mu^{FR} > 0$ is the dynamic fluid viscosity and $K^S > 0$ represents the intrinsic permeability of the solid. To describe isotropic permeability, it is sufficient to introduce the permeability as a scalar-valued parameter. For more information about permeability with anisotropic properties, the interested reader is referred to Wagner [118] and citations therein, especially Markert [88]. The intrinsic permeability is a purely geometrical measure. Often also other permeabilities are used, such as the specific permeability K^F or the Darcy flow coefficient k^F :

$$K^F := \frac{K^S}{\mu^{FR}} \quad \text{and} \quad k^F := \frac{\gamma^{FR}}{\mu^{FR}} K^S \quad (4.42)$$

with the effective fluid weight $\gamma^{FR} = \rho^{FR} |\mathbf{g}|$. Moreover, to consider a change in the permeability due to the deformation of the solid constituent, following Eipper [49], the relation

$$K^S := \left(\frac{1 - n^S}{1 - n_{0S}^S} \right)^\kappa K_{0S}^S \quad \text{with} \quad \kappa > 0 \quad (4.43)$$

is introduced. Therein, K_{0S}^S is the initial permeability of the solid constituent in the reference configuration and κ is a material parameter to adjust the dependency of the

permeability on the solid deformation. For further details about various permeability measures and their deformation dependency, the interested reader is referred to Markert [89].

It follows with (4.4), (4.33) and (4.35)₂ for the fluid momentum balance (3.49)₂

$$\mathbf{0} = \operatorname{div}(-n^F p \mathbf{I}) + \rho^F \mathbf{g} + \hat{\mathbf{p}}_E^F + \frac{\theta^S}{\theta^F} p \operatorname{grad} n^F. \quad (4.44)$$

Insertion of the constitutive relation (4.41) and further reformulation (cf. Ehlers [39]) yields

$$\mathbf{0} = -n^F \operatorname{grad} p + \rho^F \mathbf{g} - \frac{\mu^{FR}}{K^S} (n^F)^2 \mathbf{w}_F + \left(\frac{\theta^S}{\theta^F} - 1\right) p \operatorname{grad} n^F. \quad (4.45)$$

Following the arguments of Heider [73], for the considered small deformations, the gradient of the volume fractions can be omitted. Finally, this leads to Darcy's well-known equation for fluid flow in porous media

$$n^F \mathbf{w}_F = \frac{K^S}{\mu^{FR}} [-\operatorname{grad} p + \rho^{FR} \mathbf{g}]. \quad (4.46)$$

4.3.2 Helmholtz free energy and entropy

Proceeding from the definition of the volume-specific heat capacity (cf. Baehr & Kabelac [4])

$$C_V^F := \frac{\partial \varepsilon^F}{\partial \theta^F}, \quad (4.47)$$

in conjunction with the Legendre transformation and with the relations (4.30)₃ and (4.35)₃, it follows

$$C_V^F = \frac{\partial \varepsilon^F}{\partial \eta_E^F} \frac{\partial \eta_E^F}{\partial \theta^F} = -\theta^F \frac{\partial^2 \psi^F}{\partial (\theta^F)^2}. \quad (4.48)$$

Moreover, with the initial conditions $\eta_E^F(\theta^F = \theta_0^F) = 0$ and $\psi^F(\theta^F = \theta_0^F) = 0$ integration yields for the Helmholtz free energy

$$\psi^F(\theta^F) = -C_V^F \left[\theta^F \left(\ln \frac{\theta^F}{\theta_0^F} - 1 \right) + \theta_0^F \right]. \quad (4.49)$$

Thus,

$$(\psi^F)'_F = \frac{\partial \psi^F}{\partial \theta^F} (\theta^F)'_F = -C_V^F \ln \frac{\theta^F}{\theta_0^F} (\theta^F)'_F. \quad (4.50)$$

Furthermore, starting from relation (4.49), with (4.30)₃ and (4.35)₃, the fluid entropy and its material time derivative read

$$\begin{aligned} \eta^F &= C_V^F \ln \frac{\theta^F}{\theta_0^F} - p \frac{3 \alpha^F}{\rho^{FR}}, \\ (\eta^F)'_F &= \left[C_V^F \frac{1}{\theta^F} - p \frac{(3 \alpha^F)^2}{\rho^{FR}} \right] (\theta^F)'_F - \frac{3 \alpha^F}{\rho^{FR}} (p)'_F. \end{aligned} \quad (4.51)$$

4.4 The solid constituent

Under the assumption of small deformations, the linearisation of the solid volume fraction (4.8) about the initial state, yields

$$\text{lin}(n^S) = n_{0S}^S (1 - \text{div } \mathbf{u}_S). \quad (4.52)$$

Due to the fact that, during the process of hot water production, the load on the rock within a geothermal reservoir is completely within the elastic domain of the material, it is meaningful to assume an entirely elastic solid material behaviour. Moreover, it is supposed that the material behaviour is isotropic. Due to the assumption of a constant solid density ρ^{SR} , the deformation of the solid is only induced by mechanical reasons. This means

$$\mathbf{F}_S \approx \mathbf{F}_{S, \text{mech}}, \quad \text{since} \quad \mathbf{F}_{S, \text{therm}} = (\det \mathbf{F}_{S, \text{therm}})^{1/3} \mathbf{I} \approx \mathbf{I} \quad (4.53)$$

This leads to a description of a hyperelastic body, where, as it is shown in the following, the free Helmholtz energy can be additively split into a mechanical and a thermal part.

4.4.1 Helmholtz free energy and entropy

In the context of the description of a hyperplastic body, the Helmholtz free energy ψ^S of the solid constituent can be additively split into a mechanical part ψ_{mech}^S and a thermal part ψ_{therm}^S , viz.

$$\psi^S = \psi_{\text{mech}}^S + \psi_{\text{therm}}^S \quad \text{with} \quad \begin{cases} \psi_{\text{mech}}^S = \psi_{\text{mech}}^S(\mathbf{C}_S), \\ \psi_{\text{therm}}^S = \psi_{\text{therm}}^S(\theta^S). \end{cases} \quad (4.54)$$

Proceeding from Simo & Pister [107], the mechanical part of the Helmholtz free energy is defined as follows:

$$\rho_{0S}^S \psi_{\text{mech}}^S = \frac{1}{2} \mu^S (\mathbf{C}_S \cdot \mathbf{I} - 3) - \mu^S \ln(\det \mathbf{C}_S)^{\frac{1}{2}} + \frac{1}{2} \lambda^S [\ln(\det \mathbf{C}_S)^{\frac{1}{2}}]^2. \quad (4.55)$$

Therein, μ^S and λ^S are the Lamé constants. Furthermore, analogously to the Helmholtz free energy of the fluid, cf. (4.47)-(4.49), the thermal part of ψ^S reads

$$\psi_{\text{therm}}^S = -C_V^S [\theta^S (\ln \frac{\theta^S}{\theta_0^S} - 1) + \theta_0^S]. \quad (4.56)$$

It follows with (3.35)₃ and (4.30)₁ that

$$\begin{aligned} \mathbf{S}_E^S &= 2\rho_{0S}^S \frac{\partial \psi_{\text{mech}}^S}{\partial \mathbf{C}_S}, \\ &= \rho_{0S}^S \frac{\partial \psi_{\text{mech}}^S}{\partial \mathbf{E}_S}, \quad \text{because} \quad \frac{\partial \mathbf{C}_S}{\partial \mathbf{E}_S} = 2(\mathbf{I} \otimes \mathbf{I})^T. \end{aligned} \quad (4.57)$$

The linearisation of \mathbf{S}_E^S about the undeformed reference configuration, i. e., for $\mathbf{E}_S = \mathbf{0}$, yields

$$\text{lin}(\mathbf{S}_E^S) = 2\mu^S \mathbf{E}_S + \lambda^S (\mathbf{E}_S \cdot \mathbf{I}) \mathbf{I}, \quad (4.58)$$

which is the so-called de-Saint-Venant elasticity model for materially linear solids. It can be shown analogously that the linearisation of the Cauchy extra stress tensor reads

$$\text{lin}(\mathbf{T}_E^S) = 2\mu^S \mathbf{A}_S + \lambda^S (\mathbf{A}_S \cdot \mathbf{I}) \mathbf{I}. \quad (4.59)$$

By inserting (3.22) into (3.23) and applying (3.19), the strain tensors \mathbf{E}_S and \mathbf{A}_S can be expressed in terms of the displacement vector \mathbf{u}_S , namely:

$$\begin{aligned} \mathbf{E}_S &= \frac{1}{2} (\text{Grad}_S \mathbf{u}_S + \text{Grad}_S^T \mathbf{u}_S + \text{Grad}_S^T \mathbf{u}_S \text{Grad}_S \mathbf{u}_S), \\ \mathbf{A}_S &= \frac{1}{2} (\text{grad} \mathbf{u}_S + \text{grad}^T \mathbf{u}_S - \text{grad}^T \mathbf{u}_S \text{grad} \mathbf{u}_S). \end{aligned} \quad (4.60)$$

Furthermore, while assuming small deformations, $\text{Grad}_S \mathbf{u}_S \approx \text{grad} \mathbf{u}_S$ and the higher-order product of the displacement gradients can be neglected. Thus, the geometrical linearisation of the strain tensors yields

$$\text{lin}(\mathbf{A}_S) \equiv \text{lin}(\mathbf{E}_S) = \frac{1}{2} (\text{grad} \mathbf{u}_S + \text{grad}^T \mathbf{u}_S) = \text{sym}(\text{grad} \mathbf{u}_S) =: \boldsymbol{\varepsilon}_S, \quad (4.61)$$

where $\boldsymbol{\varepsilon}_S$ is the linear strain tensor. Consequently, assuming a materially linear solid skeleton, in the geometrically linear regime, the extra stress tensors \mathbf{S}_E^S and \mathbf{T}_E^S become equivalent and reduce to the linear extra stress tensor $\boldsymbol{\sigma}_E^S$:

$$\text{lin}(\mathbf{S}_E^S) \equiv \text{lin}(\mathbf{T}_E^S) = 2\mu^S \boldsymbol{\varepsilon}_S + \lambda^S (\boldsymbol{\varepsilon}_S \cdot \mathbf{I}) \mathbf{I} =: \boldsymbol{\sigma}_E^S. \quad (4.62)$$

This relation describes a generalised 3-d Hookean model for a linear elastic material. Thus, the Helmholtz free energy ψ_{lin}^S considering linearised stress and strain is given by

$$\rho_{0S}^S \psi_{\text{lin}}^S := \mu^S \boldsymbol{\varepsilon}_S \cdot \boldsymbol{\varepsilon}_S + \frac{1}{2} \lambda^S (\boldsymbol{\varepsilon}_S \cdot \mathbf{I})^2 - \rho_{0S}^S C_V^S [\theta^S (\ln \frac{\theta^S}{\theta_0^S} - 1) + \theta_0^S]. \quad (4.63)$$

According to (4.30)₂, differentiation of the Helmholtz free energy with respect to the solid temperature yields the entropy of the solid constituent, namely

$$\eta^S = - \frac{\partial \psi^S}{\partial \theta^S} = - \frac{\partial \psi_{\text{therm}}^S}{\partial \theta^S} = C_V^S \ln \frac{\theta^S}{\theta_0^S}. \quad (4.64)$$

Moreover, with

$$\boldsymbol{\sigma}_E^S = \rho_{0S}^S \frac{\partial \psi_{\text{lin}}^S}{\partial \boldsymbol{\varepsilon}_S}, \quad (4.65)$$

based on (4.57), while considering linearised stress and strain, and recalling (4.30)₂, the material time derivative of ψ_{lin}^S reads

$$\begin{aligned} (\psi_{\text{lin}}^S)'_S &= \frac{\partial \psi_{\text{lin}}^S}{\partial \boldsymbol{\varepsilon}_S} \cdot (\boldsymbol{\varepsilon}_S)'_S + \frac{\partial \psi_{\text{lin}}^S}{\partial \theta^S} (\theta^S)'_S, \\ &= \frac{1}{\rho_{0S}^S} \boldsymbol{\sigma}_E^S \cdot (\boldsymbol{\varepsilon}_S)'_S - C_V^S \ln \frac{\theta^S}{\theta_0^S} (\theta^S)'_S. \end{aligned} \quad (4.66)$$

Furthermore, the material time derivative of η^S is given by

$$(\eta^S)'_S = \frac{\partial \eta^S}{\partial \theta^S} (\theta^S)'_S = \frac{C_V^S}{\theta^S} (\theta^S)'_S. \quad (4.67)$$

4.5 Thermal conditions

4.5.1 Heat exchange between the solid and the fluid constituent

As a consequence of the consideration of individual temperatures for the constituents, a suitable constitutive characterisation of the heat transfer between the solid skeleton and the fluid is necessary. Proceeding from the proportional approach (4.32)₄, which was intentionally introduced to fulfil the restriction from the dissipation inequality, a constitutive ansatz for k_θ^ε is required. The heat exchange takes place at the interface between the constituents. Since the balance relations, and therefore k_θ^ε , are given in a volume-specific manner, an additional parameter ω is needed to describe the amount of interface area a_Γ per volume (cf. e. g. Ehlers & Häberle [47]). Thus,

$$k_\theta^\varepsilon = \frac{da_\Gamma}{dv} k_\theta^{\varepsilon I} =: \omega k_\theta^{\varepsilon I}, \quad (4.68)$$

where $k_\theta^{\varepsilon I}$ is the heat transfer coefficient at the interface between the solid and the fluid constituent. The specific values for ω must be reasonably selected for the considered case. This might be based, for example, on the grain size for a granular material, as it is described by Graf [67], or as it is done within this work, ensuing from the values given in the literature, e. g., by Doonechaly *et al.* [33].

4.5.2 Heat flux

The thermal conduction within the constituents is represented by a diffusion process. This mechanism is constitutively described with aid of the proportional relations (4.32)_{2,3}. In order to consider the biphasic approach, the real heat conductivity $\mathbf{H}^{\alpha R}$ of the constituent φ^α multiplied with the volume fraction yields the partial heat conductivity

$$\mathbf{H}^\alpha := n^\alpha \mathbf{H}^{\alpha R}. \quad (4.69)$$

Under isotropic conductivity conditions, the real heat conductivity can be reduced to a scalar valued parameter $H^{\alpha R}$, via

$$\mathbf{H}^{\alpha R} = H^{\alpha R} \mathbf{I}. \quad (4.70)$$

4.6 Balance relations of the non-isothermal biphasic model

To describe a thermo-mechanical, initial-boundary-value problem (IBVP), the primary variables (PV) pore pressure p , solid displacement \mathbf{u}_S , as well as the temperatures θ^F

and θ^S , are determined by evaluating appropriate balance relations. The pore pressure is computed via the mass balance of the fluid constituent. The momentum balance of the overall aggregate is utilised to obtain the solid displacement. Therefore, in contrast to the momentum balance only for the solid constituent, the stress at the boundary is not applied on the single constituent, but on the overall aggregate. The temperatures of the constituents are determined via the energy balance relations of the solid and the fluid constituent, respectively.

In the following, the constitutive assumptions, already presented in the current chapter, are inserted into the governing balance equations from section 3.4. The final strong form of the balance equations only consists of the PV and already known values such as material parameters, initial values and, as a part of the action at a distance, r^α and \mathbf{g} . Secondary variables which, in turn, solely contain PV and already known parameters, were used for the sake of clarity. It turns out that it is obviously possible to close the continuum-mechanical problem by means of the thermomechanical consistent constitutive assumptions that are chosen within this work.

4.6.1 Mass balance of the fluid

Using the identity $\rho^F \operatorname{div} \dot{\mathbf{x}}_S - \rho^F \operatorname{div} \dot{\mathbf{x}}_S = 0$ to reformulate the mass balance (3.44)₂ for the fluid constituent φ^F yields

$$(\rho^F)'_F + \rho^F \operatorname{div} \mathbf{w}_F + \rho^F \operatorname{div} \dot{\mathbf{x}}_S = 0. \quad (4.71)$$

It follows after some appropriate reformulations

$$(n^F)'_S \rho^{FR} + n^F (\rho^{FR})'_S + \operatorname{div}(n^F \rho^{FR} \mathbf{w}_F) + n^F \rho^{FR} \operatorname{div}(\mathbf{u}_S)'_S = 0. \quad (4.72)$$

Finally, with (4.17), the derivative of the saturation condition (4.15) and the volume balance of the solid (4.16)₁, the governing equation for the pore pressure reads

$$\operatorname{div}(n^F \rho^{FR} \mathbf{w}_F) + \rho^{FR} \operatorname{div}(\mathbf{u}_S)'_S - 3 \alpha^F n^F \rho^{FR} (\theta^F)'_S = 0. \quad (4.73)$$

Therein, the following secondary variables are included:

$$n^F = 1 - n_{0S}^S (1 - \operatorname{div} \mathbf{u}_S),$$

$$\rho^{FR} = \rho_{0S}^{FR} e^{-3 \alpha^F (\theta^F - \theta_0^F)},$$

$$\mathbf{w}_F = \frac{\left(\frac{1 - n_{0S}^S (1 - \operatorname{div} \mathbf{u}_S)}{1 - n_{0S}^S}\right)^\kappa K_{0S}^S}{[1 - n_{0S}^S (1 - \operatorname{div} \mathbf{u}_S)] \mu^{FR}} [-\operatorname{grad} p + \rho_{0S}^{FR} e^{-3 \alpha^F (\theta^F - \theta_0^F)} \mathbf{g}]. \quad (4.74)$$

4.6.2 Momentum balance of the overall aggregate

The momentum balance of the overall aggregate (3.49)₁ equals the sum of the momentum balances of the individual constituents (3.49)₂. Therefore, assuming quasi-static conditions yields

$$\operatorname{div} \mathbf{T} + \rho \mathbf{g} = \operatorname{div} \mathbf{T}^S + \operatorname{div} \mathbf{T}^F + (\rho^S + \rho^F) \mathbf{g} + \hat{\mathbf{p}}^S + \hat{\mathbf{p}}^F = \mathbf{0}. \quad (4.75)$$

If mass transfer between the constituents is further excluded, it can be shown from the time derivative of (3.51)₁ and (3.51)₂ that (cf. e.g. Wagner [118]):

$$\operatorname{div} \mathbf{T} = \operatorname{div}(\mathbf{T}^S + \mathbf{T}^F). \quad (4.76)$$

Thus, with the sum of the direct momentum production (3.51)₄, equation (4.75) reads

$$\operatorname{div}(\mathbf{T}^S + \mathbf{T}^F) + (\rho^S + \rho^F)\mathbf{g} = \mathbf{0}. \quad (4.77)$$

Finally, recalling (3.5), (4.33), (4.35)₁, and $\mathbf{T}_E^S \approx \boldsymbol{\sigma}_E^S$, the governing equation for the solid displacement results in

$$\operatorname{div}\{\boldsymbol{\sigma}_E^S - [n^S(\frac{\theta^S}{\theta^F} - 1) + 1]p\mathbf{I}\} + [n^S\rho^{SR} + (1 - n^S)\rho^{FR}]\mathbf{g} = \mathbf{0}. \quad (4.78)$$

Therein, the following secondary variables are included:

$$\begin{aligned} \boldsymbol{\sigma}_E^S &= 2\mu^S \operatorname{sym}(\operatorname{grad} \mathbf{u}_S) + \lambda^S[\operatorname{sym}(\operatorname{grad} \mathbf{u}_S) \cdot \mathbf{I}]\mathbf{I}, \\ n^S &= n_{0S}^S(1 - \operatorname{div} \mathbf{u}_S), \\ \rho^{FR} &= \rho_{0S}^{FR} e^{-3\alpha^F(\theta^F - \theta_0^F)}. \end{aligned} \quad (4.79)$$

4.6.3 Energy balance of the fluid

Reformulation of the local energy balance (3.58)₂ for the fluid constituent by using the Legendre transformation (3.69) yields

$$\rho^F (\psi^F)'_F + \rho^F (\theta^F)'_F \eta^F + \rho^F \theta^F (\eta^F)'_F = \mathbf{T}^F \cdot \mathbf{L}_F - \operatorname{div} \mathbf{q}^F + \rho^F r^F + \hat{\varepsilon}^F. \quad (4.80)$$

With the density relation (3.5), the time derivative of the fluid's free Helmholtz energy (4.50), the fluid entropy (4.51)₁ and its time derivative (4.51)₂, it follows

$$\begin{aligned} [-n^F \rho^{FR} C_V^F + 3\alpha^F n^F p + (3\alpha^F)^2 n^F p \theta^F] (\theta^F)'_F + 3\alpha^F n^F \theta^F (p)'_F + \\ + \mathbf{T}^F \cdot \mathbf{L}_F - \operatorname{div} \mathbf{q}^F + \rho^F r^F + \hat{\varepsilon}^F = 0. \end{aligned} \quad (4.81)$$

Further reformulation with the definition of the partial fluid stress (4.33), the velocity gradient (3.26), the fluid mass balance, the material time derivative of the real fluid density (4.17) and, moreover, relating the material time derivatives to the motion of the solid constituent provides

$$\begin{aligned} [-n^F \rho^{FR} C_V^F + n^F \theta^F p (3\alpha^F)^2] [(\theta^F)'_S + \operatorname{grad} \theta^F \cdot \mathbf{w}_F] + \\ + 3\alpha^F n^F \theta^F [(p)'_S + \operatorname{grad} p \cdot \mathbf{w}_F] + \\ + p [(n^F)'_S + \operatorname{grad} n^F \cdot \mathbf{w}_F] - \operatorname{div} \mathbf{q}^F + n^F \rho^{FR} r^F + \hat{\varepsilon}^F = 0. \end{aligned} \quad (4.82)$$

Finally, neglecting the gradient of the volume fraction according to Heider [73] and applying the solid volume balance, yields, based on the energy balance of the fluid, the governing equation for the fluid temperature:

$$\begin{aligned} & [-n^F \rho^{FR} C_V^F + n^F \theta^F p (3\alpha^F)^2][(\theta^F)'_S + \text{grad } \theta^F \cdot \mathbf{w}_F] + \\ & \quad + 3\alpha^F n^F \theta^F [(p)'_S + \text{grad } p \cdot \mathbf{w}_F] + \\ & \quad + n^S p \text{div}(\mathbf{u}_S)'_S - \text{div } \mathbf{q}^F + n^F \rho^{FR} r^F + \hat{\varepsilon}^F = 0. \end{aligned} \quad (4.83)$$

Therein, the following secondary variables are included:

$$\begin{aligned} n^S &= n_{0S}^S (1 - \text{div } \mathbf{u}_S), \\ n^F &= 1 - n_{0S}^S (1 - \text{div } \mathbf{u}_S), \\ \rho^{FR} &= \rho_{0S}^{FR} e^{-3\alpha^F(\theta^F - \theta_0^F)}, \\ \mathbf{w}_F &= \frac{\left(\frac{1 - n_{0S}^S(1 - \text{div } \mathbf{u}_S)}{1 - n_{0S}^S}\right)^\kappa K_{0S}^S}{[1 - n_{0S}^S(1 - \text{div } \mathbf{u}_S)] \mu^{FR}} [-\text{grad } p + \rho_{0S}^{FR} e^{-3\alpha^F(\theta^F - \theta_0^F)} \mathbf{g}], \\ \mathbf{q}^F &= -[1 - n_{0S}^S(1 - \text{div } \mathbf{u}_S)] H^{FR} \text{grad } \theta^F, \\ \hat{\varepsilon}^F &= \omega k_\theta^{\varepsilon I} (\theta^S - \theta^F). \end{aligned} \quad (4.84)$$

4.6.4 Energy balance of the solid

Rewriting the energy balance (3.58)₂ for the solid constituent, yields in the case of a symmetric stress tensor and with the aid of the Legendre transformation (3.69)

$$\rho^S (\psi_{\text{lin}}^S)'_S + \rho^S (\theta^S)'_S \eta^S + \rho^S \theta^S (\eta^S)'_S = \mathbf{T}^S \cdot \mathbf{D}_S - \text{div } \mathbf{q}^S + \rho^S r^S + \hat{\varepsilon}^S. \quad (4.85)$$

With the density relation (3.5), the time derivative of the solid free Helmholtz energy (4.66), the solid entropy (4.64) and its time derivative (4.67) it follows

$$-\frac{n^S}{n_{0S}^S} \boldsymbol{\sigma}_E^S \cdot (\boldsymbol{\varepsilon}_S)'_S - n^S \rho^{SR} C_V^S (\theta^S)'_S + \mathbf{T}^S \cdot \mathbf{D}_S - \text{div } \mathbf{q}^S + n^S \rho^{SR} r^S + \hat{\varepsilon}^S = 0. \quad (4.86)$$

Further reformulation with the linearisation of the solid volume fraction (4.52), the definition of the solid extra stress (4.35)₁, $\mathbf{T}_E^S \approx \boldsymbol{\sigma}_E^S$ and $\mathbf{D}_S = (\boldsymbol{\varepsilon}_S)'_S$ yields

$$\begin{aligned} & (\text{div } \mathbf{u}_S) \boldsymbol{\sigma}_E^S \cdot (\boldsymbol{\varepsilon}_S)'_S - n^S \rho^{SR} C_V^S (\theta^S)'_S - \frac{\theta^S}{\theta^F} n^S p \mathbf{I} \cdot (\boldsymbol{\varepsilon}_S)'_S - \\ & \quad - \text{div } \mathbf{q}^S + n^S \rho^{SR} r^S + \hat{\varepsilon}^S = 0. \end{aligned} \quad (4.87)$$

Finally, with the sums of the linear momentum (3.60)₄ and energy production (3.51)₄, while assuming that the mass production is excluded and the gradient of the solid volume

fraction can be neglected, the governing equation for the solid temperature, based on the energy balance of the solid, reads

$$\begin{aligned} & (\operatorname{div} \mathbf{u}_S) \boldsymbol{\sigma}_E^S \cdot (\boldsymbol{\varepsilon}_S)'_S - n^S \rho^{SR} C_V^S (\theta^S)'_S - \frac{\theta^S}{\theta^F} n^S p \operatorname{div}(\mathbf{u}_S)'_S - \\ & - \operatorname{div} \mathbf{q}^S + n^S \rho^{SR} r^S - \hat{\varepsilon}^F - \hat{\mathbf{p}}_E^F \cdot \mathbf{w}_F = 0. \end{aligned} \quad (4.88)$$

Therein, the following secondary variables are included:

$$\begin{aligned} \boldsymbol{\sigma}_E^S &= 2 \mu^S \operatorname{sym}(\operatorname{grad} \mathbf{u}_S) + \lambda^S [\operatorname{sym}(\operatorname{grad} \mathbf{u}_S) \cdot \mathbf{I}] \mathbf{I}, \\ \boldsymbol{\varepsilon}_S &= \operatorname{sym}(\operatorname{grad} \mathbf{u}_S), \\ n^S &= n_{0S}^S (1 - \operatorname{div} \mathbf{u}_S), \\ \mathbf{q}^S &= -n_{0S}^S (1 - \operatorname{div} \mathbf{u}_S) H^{SR} \operatorname{grad} \theta^S, \\ \hat{\varepsilon}^F &= \omega k_\theta^{\varepsilon I} (\theta^S - \theta^F), \\ \hat{\mathbf{p}}_E^F &= [1 - n_{0S}^S (1 - \operatorname{div} \mathbf{u}_S)] [\operatorname{grad} p - \rho_{0S}^{FR} e^{-3\alpha^F (\theta^F - \theta_0^F)} \mathbf{g}], \\ \mathbf{w}_F &= \frac{\left(\frac{1-n_{0S}^S (1-\operatorname{div} \mathbf{u}_S)}{1-n_{0S}^S}\right)^\kappa K_{0S}^S}{[1 - n_{0S}^S (1 - \operatorname{div} \mathbf{u}_S)] \mu^{FR}} [-\operatorname{grad} p + \rho_{0S}^{FR} e^{-3\alpha^F (\theta^F - \theta_0^F)} \mathbf{g}]. \end{aligned} \quad (4.89)$$

Chapter 5:

Numerical treatment

In order to simulate the behaviour of an EGS with an appropriate material model, the set of partial differential equations presented in the preceding chapter has to be solved. Due to the fact that, realistically, it is an impossible endeavour to find the analytical solution for an adequate IBVP, the governing equations are transferred into a weak form, which is less restrictive. Afterwards, the IBVP is discretised in space via the FEM, and in time with the implicit Euler time integration scheme. During the further procedure, the solution is found with the aid of a Newton iteration scheme using suitable software tools.

5.1 Finite-element method

For the set of PV $\{\mathbf{u}_S, p, \theta^F, \theta^S\}$, the system of six PDE needs to be solved at each time t , while certain restrictions in the form of Dirichlet and Neumann boundary conditions at the boundary $\Gamma = \partial\Omega$, the surface of the spatial domain Ω , have to be fulfilled. The entire boundary Γ is divided into essential or Dirichlet Γ_D and natural or Neumann Γ_N boundaries with essential and natural boundary conditions, respectively. However, for every part of the boundary, for each PV, either a Dirichlet or a Neumann boundary condition has to be defined:

$$\Gamma = \Gamma_D^{\text{PV}} \cup \Gamma_N^{\text{PV}} \quad \text{with} \quad \Gamma_D^{\text{PV}} \cap \Gamma_N^{\text{PV}} = \emptyset. \quad (5.1)$$

5.1.1 Weak forms of the governing equations

The FEM is chosen as a suitable approach to solve the system of PDE. In this context, the local forms (4.73), (4.78), (4.83) and (4.88) of the governing equations are integrated over the spatial domain Ω . In the sense of this finite-element formulation, the equations are weighted by the independent test functions $\delta\mathbf{u}_S$, δp , $\delta\theta^F$ and $\delta\theta^S$, respectively.

The trial spaces \mathcal{S}^{PV} and the test spaces \mathcal{T}^{PV} are defined via

$$\begin{aligned} \mathcal{S}^{\mathbf{u}_S}(t) &:= \{ \mathbf{u}_S \in \mathcal{H}^1(\Omega)^d : \mathbf{u}_S(\mathbf{x}) = \bar{\mathbf{u}}_S(\mathbf{x}, t) \text{ on } \Gamma_D^{\mathbf{u}_S} \}, \\ \mathcal{S}^p(t) &:= \{ p \in \mathcal{H}^1(\Omega) : p(\mathbf{x}) = \bar{p}(\mathbf{x}, t) \text{ on } \Gamma_D^p \}, \\ \mathcal{S}^{\theta^F}(t) &:= \{ \theta^F \in \mathcal{H}^1(\Omega) : \theta^F(\mathbf{x}) = \bar{\theta}^F(\mathbf{x}, t) \text{ on } \Gamma_D^{\theta^F} \}, \\ \mathcal{S}^{\theta^S}(t) &:= \{ \theta^S \in \mathcal{H}^1(\Omega) : \theta^S(\mathbf{x}) = \bar{\theta}^S(\mathbf{x}, t) \text{ on } \Gamma_D^{\theta^S} \} \end{aligned} \quad (5.2)$$

and

$$\begin{aligned}
\mathcal{T}^{\mathbf{u}_S} &:= \{ \delta \mathbf{u}_S \in \mathcal{H}^1(\Omega)^d : \delta \mathbf{u}_S(\mathbf{x}) = \mathbf{0} \text{ on } \Gamma_D^{\mathbf{u}_S} \}, \\
\mathcal{T}^p &:= \{ \delta p \in \mathcal{H}^1(\Omega) : \delta p(\mathbf{x}) = 0 \text{ on } \Gamma_D^p \}, \\
\mathcal{T}^{\theta^F} &:= \{ \delta \theta^F \in \mathcal{H}^1(\Omega) : \delta \theta^F(\mathbf{x}) = 0 \text{ on } \Gamma_D^{\theta^F} \}, \\
\mathcal{T}^{\theta^S} &:= \{ \delta \theta^S \in \mathcal{H}^1(\Omega) : \delta \theta^S(\mathbf{x}) = 0 \text{ on } \Gamma_D^{\theta^S} \}.
\end{aligned} \tag{5.3}$$

Therein, \mathcal{H}^1 is the Sobolev space that ensures the square-integrability of the first derivatives of the trial and test functions (cf., e. g., Bathe [8]). Moreover, since the momentum balance is a vector-valued equation, the superscript $d \in \{1, 2, 3\}$ represents the spatial dimension in the 3-d space. At the Dirichlet boundaries, the corresponding test function vanishes, whereas the PV matches the value of the Dirichlet boundary condition. Moreover, to apply natural boundary conditions, some of the volume integrals have to be transformed into surface integrals¹ via applying the Gaußian integral theorem. Finally, it follows for the scalar-valued functionals \mathcal{G}_{PV} and, therefore, for the weak form of the governing equations:

$$\begin{aligned}
\mathcal{G}_{\mathbf{u}_S}(\mathbf{u}_S, p, \theta^F, \theta^S, \delta \mathbf{u}_S) &:= \int_{\Omega} [n^S \rho^{SR} + (1 - n^S) \rho^{FR}] \mathbf{g} \cdot \delta \mathbf{u}_S \, dv - \\
&- \int_{\Omega} \{ \boldsymbol{\sigma}_E^S - [n^S (\frac{\theta^S}{\theta^F} - 1) + 1] p \mathbf{I} \} \cdot \text{grad } \delta \mathbf{u}_S \, dv + \int_{\Gamma_N^{\mathbf{u}_S}} \bar{\mathbf{t}} \cdot \delta \mathbf{u}_S \, da = 0,
\end{aligned} \tag{5.4}$$

$$\begin{aligned}
\mathcal{G}_p(\mathbf{u}_S, p, \theta^F, \delta p) &:= \int_{\Omega} [\text{div}(\mathbf{u}_S)'_S - 3 \alpha^F n^F (\theta^F)'_S] \rho^{FR} \delta p \, dv - \\
&- \int_{\Omega} n^F \rho^{FR} \mathbf{w}_F \cdot \text{grad } \delta p \, dv + \int_{\Gamma_N^p} \bar{m} \delta p \, da = 0,
\end{aligned} \tag{5.5}$$

$$\begin{aligned}
\mathcal{G}_{\theta^F}(\mathbf{u}_S, p, \theta^F, \theta^S, \delta \theta^F) &:= \int_{\Omega} \{ 3 \alpha^F n^F \theta^F [(p)'_S + \text{grad } p \cdot \mathbf{w}_F] + \\
&+ [-n^F \rho^{FR} C_V^F + n^F \theta^F p (3 \alpha^F)^2] [(\theta^F)'_S + \text{grad } \theta^F \cdot \mathbf{w}_F] + \\
&+ n^F p \text{div}(\mathbf{u}_S)'_S + n^F \rho^{FR} r^F + \hat{\varepsilon}^F \} \delta \theta^F \, dv + \\
&+ \int_{\Omega} \mathbf{q}^F \cdot \text{grad } \delta \theta^F \, dv - \int_{\Gamma_N^{\theta^F}} \bar{q}^F \delta \theta^F \, da = 0,
\end{aligned} \tag{5.6}$$

¹By splitting the surface into the Neumann and Dirichlet boundaries, it becomes obvious that only the Neumann boundary Γ_N^{PV} needs to be considered, as the test function at the Dirichlet boundary is zero anyway.

$$\begin{aligned}
\mathcal{G}_{\theta^S}(\mathbf{u}_S, p, \theta^F, \theta^S, \delta\theta^S) &:= \int_{\Omega} \{ \boldsymbol{\sigma}_E^S \cdot (\boldsymbol{\varepsilon})'_S \operatorname{div} \mathbf{u}_S - n^S \rho^{SR} C_V^S (\theta^S)'_S - \\
&- \frac{\theta^S}{\theta^F} n^S p \operatorname{div}(\mathbf{u}_S)'_S + n^S \rho^{SR} r^S - \hat{\boldsymbol{\varepsilon}}^F - \hat{\mathbf{p}}_E^F \cdot \mathbf{w}_F \} \delta\theta^S dv + \\
&+ \int_{\Omega} \mathbf{q}^S \cdot \operatorname{grad} \delta\theta^S dv - \int_{\Gamma_N^{\theta^S}} \bar{q}^S \delta\theta^S da = 0.
\end{aligned} \tag{5.7}$$

Therein,

$$\begin{aligned}
\bar{\mathbf{t}} &:= \{ \boldsymbol{\sigma}_E^S - [n^S (\frac{\theta^S}{\theta^F} - 1) + 1] p \mathbf{I} \} \mathbf{n}, & \bar{m} &:= n^F \rho^{FR} \mathbf{w}_F \cdot \mathbf{n}, \\
\bar{q}^F &:= \mathbf{q}^F \cdot \mathbf{n}, & \bar{q}^S &:= \mathbf{q}^S \cdot \mathbf{n}.
\end{aligned} \tag{5.8}$$

5.1.2 Spatial discretisation

The continuous domain Ω is partitioned in several non-overlapping subdomains Ω_e , such that the union of the subdomains gives the discretised domain Ω^h with

$$\Omega \approx \Omega^h = \bigcup_e \Omega_e. \tag{5.9}$$

These subdomains are the so-called finite elements, and they are built with the help of nodal points P^j , which are further referred to as nodes. Adjacent elements are interconnected by sharing a portion of their nodes. The entire set of nodes and their connections form the finite-element mesh with a total number of \mathcal{N} nodes.

Moreover, the discretisation of the, up to now, continuous trial and test functions yields the discretised PV and the corresponding test functions

$$\begin{aligned}
\mathbf{u}_S(\mathbf{x}, t) \approx \mathbf{u}_S^h(\mathbf{x}, t) &= \bar{\mathbf{u}}_S^h(\mathbf{x}, t) + \sum_{j=1}^{\mathcal{N}} \phi_{\mathbf{u}_S}^j(\mathbf{x}) \mathbf{u}_S^j(t) \in \mathcal{S}^{\mathbf{u}_S^h}(t), \\
p(\mathbf{x}, t) \approx p^h(\mathbf{x}, t) &= \bar{p}^h(\mathbf{x}, t) + \sum_{j=1}^{\mathcal{N}} \phi_p^j(\mathbf{x}) p^j(t) \in \mathcal{S}^{p^h}(t), \\
\theta^F(\mathbf{x}, t) \approx \theta^{Fh}(\mathbf{x}, t) &= \bar{\theta}^{Fh}(\mathbf{x}, t) + \sum_{j=1}^{\mathcal{N}} \phi_{\theta^F}^j(\mathbf{x}) \theta^{Fj}(t) \in \mathcal{S}^{\theta^{Fh}}(t), \\
\theta^S(\mathbf{x}, t) \approx \theta^{Sh}(\mathbf{x}, t) &= \bar{\theta}^{Sh}(\mathbf{x}, t) + \sum_{j=1}^{\mathcal{N}} \phi_{\theta^S}^j(\mathbf{x}) \theta^{Sj}(t) \in \mathcal{S}^{\theta^{Sh}}(t)
\end{aligned} \tag{5.10}$$

and

$$\begin{aligned}
\delta \mathbf{u}_S(\mathbf{x}) &\approx \delta \mathbf{u}_S^h(\mathbf{x}) = \sum_{j=1}^{\mathcal{N}} \phi_{\mathbf{u}_S}^j(\mathbf{x}) \delta \mathbf{u}_S^j(t) \in \mathcal{T}^{\mathbf{u}_S^h}(t), \\
\delta p(\mathbf{x}) &\approx \delta p^h(\mathbf{x}) = \sum_{j=1}^{\mathcal{N}} \phi_p^j(\mathbf{x}) \delta p^j(t) \in \mathcal{T}^{p^h}(t), \\
\delta \theta^F(\mathbf{x}) &\approx \delta \theta^{F^h}(\mathbf{x}) = \sum_{j=1}^{\mathcal{N}} \phi_{\theta^F}^j(\mathbf{x}) \delta \theta^{F^j}(t) \in \mathcal{T}^{\theta^F^h}(t), \\
\delta \theta^S(\mathbf{x}) &\approx \delta \theta^{S^h}(\mathbf{x}) = \sum_{j=1}^{\mathcal{N}} \phi_{\theta^S}^j(\mathbf{x}) \delta \theta^{S^j}(t) \in \mathcal{T}^{\theta^S^h}(t),
\end{aligned} \tag{5.11}$$

where $\mathcal{S}^{\text{PV}h}$ and $\mathcal{T}^{\text{PV}h}$ correspond to the discretised trial and test spaces. The set $\{\bar{\mathbf{u}}_S^h, \bar{p}^h, \bar{\theta}^{F^h}, \bar{\theta}^{S^h}\}$ defines the Dirichlet boundary conditions and the set of global basis functions $\{\phi_{\mathbf{u}_S}^j, \phi_p^j, \phi_{\theta^F}^j, \phi_{\theta^S}^j\}$ is, according to the Bubnov-Galerkin method, used for the trial and the test functions, where, for the 3-d case, $\phi_{\mathbf{u}_S}^j = [\phi_{u_{S1}}^j, \phi_{u_{S2}}^j, \phi_{u_{S3}}^j]^T$. Moreover, the variables $u_{S1}^j, u_{S2}^j, u_{S3}^j, p^j, \theta^{F^j}$ and θ^{S^j} compose the six nodal degrees of freedom (DOF). Recalling (5.4)–(5.7), the spatially discretised variational problem can be summarised as follows:

$$\text{Find } \left\{ \begin{array}{l} \mathbf{u}_S^h \in \mathcal{S}^{\mathbf{u}_S^h} \\ p^h \in \mathcal{S}^{p^h} \\ \theta^{F^h} \in \mathcal{S}^{\theta^{F^h}} \\ \theta^{S^h} \in \mathcal{S}^{\theta^{S^h}} \end{array} \right\} \text{ such that } \left\{ \begin{array}{l} \mathcal{G}_{\mathbf{u}_S}^h = 0 \quad \forall \delta \mathbf{u}_S^h \in \mathcal{T}^{\mathbf{u}_S^h} \\ \mathcal{G}_p^h = 0 \quad \forall \delta p^h \in \mathcal{T}^{p^h} \\ \mathcal{G}_{\theta^F}^h = 0 \quad \forall \delta \theta^{F^h} \in \mathcal{T}^{\theta^{F^h}} \\ \mathcal{G}_{\theta^S}^h = 0 \quad \forall \delta \theta^{S^h} \in \mathcal{T}^{\theta^{S^h}} \end{array} \right\} \tag{5.12}$$

at any time $t \in [0, T]$, for a given set of boundary conditions. The partition of unity and the constraint for the basis functions to be equal to 1 at the respective node and vanish for all other nodes, lead to a system of linearly independent equations. Therein, the number of equations is equivalent to the total number of DOF within the IBVP. To obtain an equal order of the variables belonging to one equation, quadratic basis functions are chosen for the solid displacement \mathbf{u}_S^h , and linear basis functions for the pore pressure p^h as well as the temperatures θ^{F^h} and θ^{S^h} . The related type of element is commonly denoted as the extended Taylor-Hood element and is depicted in Figure 5.1 for a 20-noded hexahedron.

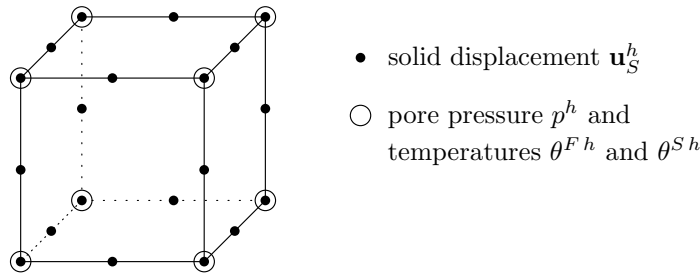


Figure 5.1: Extended hexahedral Taylor-Hood element.

Since all element quantities are evaluated locally on the element level, it is convenient to introduce a geometry transformation for the elements to a reference element. This is done here within an isoparametric concept, where the same trial functions are used for the displacement and the geometry transformation.

The semi-discretised problem can be formulated in the abstract manner

$$\mathcal{F}(t, \mathbf{y}, \mathbf{y}') = [\mathbf{d}(\mathbf{y}, \mathbf{y}') + \mathbf{k}(\mathbf{y}) - \mathbf{f}] \stackrel{!}{=} \mathbf{0}. \quad (5.13)$$

Therein, the solution vector

$$\mathbf{y} := [\mathbf{y}^1, \dots, \mathbf{y}^j, \dots, \mathbf{y}^N]^T \quad (5.14)$$

is composed of the solution vectors $\mathbf{y}^j := [u_{S1}^j, u_{S2}^j, u_{S3}^j, p^j, \theta^{Fj}, \theta^{Sj}]^T$ for the corner nodes, or $\mathbf{y}^j := [u_{S1}^j, u_{S2}^j, u_{S3}^j]^T$ for the middle nodes that are only used for the quadratic approximation of the displacement. Thus, each nodal solution vector contains the DOF of the corresponding node. Moreover, for convenience, the material time derivative with respect to the deforming solid $(\cdot)'_S$ is expressed via $(\cdot)'$. Furthermore, (5.13) contains the generalised damping vector $\mathbf{d}(\mathbf{y}, \mathbf{y}')$, the generalised stiffness vector $\mathbf{k}(\mathbf{y})$ and the generalised force vector \mathbf{f} .

5.1.3 Temporal discretisation and solution strategy

Regarding the temporal evolution of the IBVP, the system has to be discretised in time, using a suitable time-integration method. Within this work, the implicit Euler (backward Euler) time integration scheme, from the general class of Runge-Kutta methods, is selected to solve the system of differential-algebraic equations (DAE). This means, only the solution \mathbf{y}_n from the previous step at time t_n is considered to calculate the unknowns \mathbf{y}_{n+1} at the current time t_{n+1} , viz.

$$\mathbf{y}_{n+1} = \mathbf{y}_n + \Delta t \mathbf{y}'_{n+1} \quad \rightarrow \quad \mathbf{y}'_{n+1} = \frac{1}{\Delta t} (\mathbf{y}_{n+1} - \mathbf{y}_n). \quad (5.15)$$

Therein, $\Delta t = t_{n+1} - t_n$ is the temporal distance between the current and previous time and, therefore, represents the time step size. Applying the unconditionally stable implicit Euler strategy (cf. Zinatbakhsh [124]) on equation (5.13) yields

$$\mathcal{F}_{n+1}(t_{n+1}, \mathbf{y}_{n+1}, \mathbf{y}'_{n+1}) = [\mathbf{d}(\mathbf{y}_{n+1}, \mathbf{y}'_{n+1}) + \mathbf{k}(\mathbf{y}_{n+1}) - \mathbf{f}_{n+1}] \stackrel{!}{=} \mathbf{0}. \quad (5.16)$$

This set of nonlinear equations is solved iteratively with the Newton–Raphson method, where the residual tangent for each iteration step k is computed as

$$\mathbf{D}\mathcal{F}_{n+1}^k := \frac{d\mathcal{F}_{n+1}^k}{d\mathbf{y}_{n+1}^k} = \frac{\partial \mathcal{F}_{n+1}^k}{\partial \mathbf{y}_{n+1}^k} + \frac{1}{\Delta t} \frac{\partial \mathcal{F}_{n+1}^k}{\partial (\mathbf{y}')_{n+1}^k}. \quad (5.17)$$

The numerical calculation of the tangent may lead to instabilities for some IBVP. Therefore, sometimes it is necessary to analytically determined the tangent, for example, in the context of plasticity models, cf., e. g., Avci [3] for more details. However, within this work

the convergence is satisfactory, and no analytical determination of the tangent is necessary. For each iteration step, the increment $\Delta \mathbf{y}_{n+1}^k$ is calculated by solving this system of equations:

$$D\mathcal{F}_{n+1}^k \Delta \mathbf{y}_{n+1}^k = -\mathcal{F}_{n+1}^k. \quad (5.18)$$

According to Ellsiepen [50], this can be achieved by using either direct or iterative solvers. Finally, the solution is updated

$$\mathbf{y}_{n+1}^{k+1} = \mathbf{y}_{n+1}^k + \Delta \mathbf{y}_{n+1}^k \quad (5.19)$$

and the iteration is continued, until the norm of the residuum is below a certain tolerance ϵ_{tol} :

$$\|\mathcal{F}_{n+1}^{k+1}\| < \epsilon_{\text{tol}}. \quad (5.20)$$

Since this was only a brief synopsis of the numerical methodology, the interested reader is referred to Bathe [7], Belytschko *et al.* [12], Hughes [76] and Zienkiewicz *et al.* [123] for more detailed information.

5.2 Stabilisation techniques for convection dominated transport problems

The fluid energy balance

$$\underbrace{\mathbf{v}^* \cdot \text{grad } \theta^F}_{\text{convective transport}} - \underbrace{d^* \text{div grad } \theta^F}_{\text{diffusive transport}} + s^* = 0 \quad (5.21)$$

with

$$\begin{aligned} \mathbf{v}^* &:= [-n^F \rho^{FR} C_V^F + n^F \theta^F p (3 \alpha^F)^2] \mathbf{w}_F, \\ d^* &:= n^F H^{FR}, \\ s^* &:= 3 \alpha^F n^F \theta^F [(p)'_S + \text{grad } p \cdot \mathbf{w}_F] + \\ &\quad + [-n^F \rho^{FR} C_V^F + n^F \theta^F p (3 \alpha^F)^2] (\theta^F)'_S + \\ &\quad + n^S p \text{div}(\mathbf{u}_S)'_S + n^F \rho^{FR} r^F + \hat{\epsilon}^F, \end{aligned} \quad (5.22)$$

basically describes a convection-diffusion equation for the fluid temperature. This means that the heat of the fluid is simultaneously transported by the flow of the fluid itself, thus, convectively, and also by conduction (diffusion). It is well-known that for the standard Bubnov-Galerkin FEM, which was intended to be used within this work, convection-diffusion equations tend to cause oscillation problems for some IBVP, depending on the spatial discretisation, namely the element size at particular regions.

For the sake of comprehensibility, the underlying reason for this oscillations, also known as wiggles, are further discussed on the basis of a 1-d, stationary convection-diffusion equation

$$v \frac{d\phi}{dx} - d \frac{d^2\phi}{dx^2} = s. \quad (5.23)$$

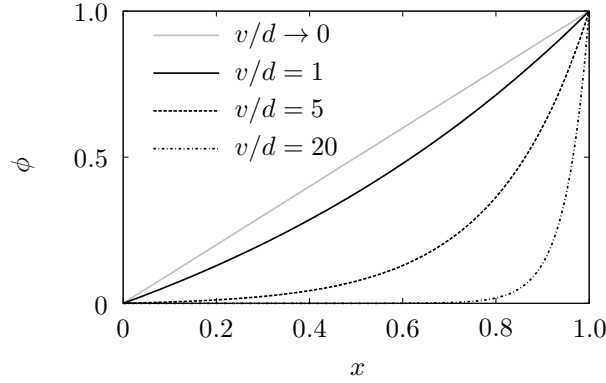


Figure 5.2: Analytical solution of a 1-d convection-diffusion equation considering different convection-diffusion ratios.

Therein, ϕ represents a scalar-valued variable and v and d are, respectively, the speed of propagation of ϕ and the diffusivity. For a constant source term s , the solution of (5.23) is given by

$$\phi(x) = \phi_0 + \left(\phi_0 + \phi_L + \frac{s}{v}\right) \frac{1 - e^{(v/d)x}}{1 - e^{v/d}} + \frac{s}{v} x, \quad (5.24)$$

where $\phi_0 = \phi(x=0)$ and $\phi_L = \phi(x=L)$ are the boundary conditions. For a spatial domain of length $L=1$ with the boundary values $\phi_0=0$ and $\phi_L=1$, and the source term $s=0$, the analytical solution

$$\phi(x) = \frac{1 - e^{(v/d)x}}{1 - e^{v/d}} \quad (5.25)$$

is exemplarily shown in Figure 5.2 for different convection-diffusion ratios. Since, for the 1-d case, the equations resulting from the Bubnov-Galerkin finite-element method with linear shape functions and from the central difference scheme are equivalent here, cf., e. g., Oñate & Manzan [94], the discretisation of the convection-diffusion equation (5.23) yields

$$v \frac{\phi_{i+1} - \phi_{i-1}}{2h} - d \frac{\phi_{i+1} - 2\phi_i + \phi_{i-1}}{h^2} = \frac{s_{i-1} + 4s_i + s_{i+1}}{6}. \quad (5.26)$$

Therein, i is the index of the respective node and h is the element size. With the definition of the dimensionless Péclet number

$$Pe := \frac{v h}{2d}, \quad (5.27)$$

(5.26) can be reformulated:

$$\frac{v}{2h} \left(\frac{Pe-1}{Pe} \phi_{i+1} + \frac{2}{Pe} \phi_i - \frac{Pe+1}{Pe} \phi_{i-1} \right) = \frac{s_{i-1} + 4s_i + s_{i+1}}{6}. \quad (5.28)$$

The Péclet number itself is an indicator, whether the convective part ($Pe > 1$) or the diffusive part ($Pe < 1$) is dominant. According to Gresho & Lee [68], for a BVP with

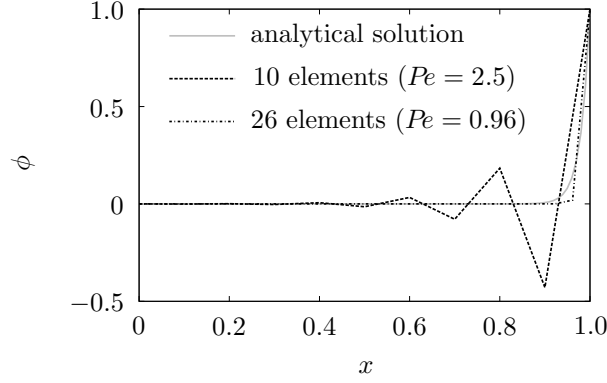


Figure 5.3: Discrete solution of a 1-d convection-diffusion equation for different numbers of elements with a convection-diffusion relation $v/d = 50$.

length $L = 1$, the boundary conditions $\phi_0 = 0$ and $\phi_L = 1$ and no source ($s = 0$), the solution of equation (5.28) reads

$$\phi_i = \frac{1 - \left(\frac{1+Pe}{1-Pe}\right)^i}{1 - \left(\frac{1+Pe}{1-Pe}\right)^N}. \quad (5.29)$$

Obviously, the solution oscillates node-wise, if $Pe > 1$. The numerical solution (5.29) is shown in Figure 5.3 for discretisations with 10 and 26 elements, in comparison with the analytical solution. Apparently, discretisations of BVP that induce Péclet numbers beyond 1 are unable to reproduce the high gradient of ϕ for $x \rightarrow 1$ and end up in spurious node-to-node oscillations.

In the following, the error of the standard Galerkin method for the solution of the discrete equation is analysed. Therefore, following Donea & Huerta [32], a discrete scheme with similar structure to equation (5.28) is invented via

$$\alpha_1 \phi_{i+1} + \alpha_2 \phi_i + \alpha_3 \phi_{i-1} = s, \quad (5.30)$$

where the source term $s = s_i = s_{i+1} = s_{i-1}$ is constant. To determine the corresponding parameters α_1 , α_2 , and α_3 , the discrete values of ϕ are evaluated using the analytical solution (5.24):

$$\begin{aligned} \phi_{i+1} &= \phi_0 + \left(\phi_L - \phi_0 - \frac{s}{v}\right) \frac{1 - e^{(v/d)x_i} e^{2Pe}}{1 - e^{v/d}} + \frac{s}{v} x_i + \frac{s}{v} h, \\ \phi_i &= \phi_0 + \left(\phi_L - \phi_0 - \frac{s}{v}\right) \frac{1 - e^{(v/d)x_i}}{1 - e^{v/d}} + \frac{s}{v} x_i, \\ \phi_{i-1} &= \phi_0 + \left(\phi_L - \phi_0 - \frac{s}{v}\right) \frac{1 - e^{(v/d)x_i} e^{-2Pe}}{1 - e^{v/d}} + \frac{s}{v} x_i - \frac{s}{v} h. \end{aligned} \quad (5.31)$$

Inserting these discrete values into (5.30) yields, after some reformulations,

$$\begin{aligned}
& (\alpha_1 + \alpha_2 + \alpha_3) \left(\phi_0 + \frac{s}{v} x_i \right) + (\alpha_1 - \alpha_3) \frac{s}{v} h + \\
& + \frac{\phi_L - \phi_0 - \frac{s}{v}}{1 - e^{v/d}} \left[\alpha_1 (1 - e^{(v/d) x_i} e^{2Pe}) + \right. \\
& \quad \left. + \alpha_2 (1 - e^{(v/d) x_i}) + \right. \\
& \quad \left. + \alpha_3 (1 - e^{(v/d) x_i} e^{-2Pe}) \right] = s.
\end{aligned} \tag{5.32}$$

Therefore, one possible solution can be found under the following conditions:

$$\begin{aligned}
\alpha_1 + \alpha_2 + \alpha_3 &= 0, \\
\alpha_1 - \alpha_3 &= \frac{v}{h}, \\
\alpha_1 e^{2Pe} + \alpha_2 + \alpha_3 e^{-2Pe} &= 0.
\end{aligned} \tag{5.33}$$

Hence, solving for α_1 , α_2 and α_3 provides

$$\begin{aligned}
\alpha_1 &= \frac{v}{2h} (1 - \coth Pe), \\
\alpha_2 &= \frac{v}{h} \coth Pe, \\
\alpha_3 &= -\frac{v}{2h} (1 + \coth Pe).
\end{aligned} \tag{5.34}$$

With this parameters, (5.30) and, therefore, the exact solution scheme, reads

$$\frac{v}{2h} [(1 - \coth Pe) \phi_{i+1} + (2 \coth Pe) \phi_i - (1 + \coth Pe) \phi_{i-1}] = s. \tag{5.35}$$

This equation can be rearranged in a form similar to (5.26), namely

$$v \frac{\phi_{i+1} - \phi_{i-1}}{2h} - (d + \bar{d}) \frac{\phi_{i+1} - 2\phi_i + \phi_{i-1}}{h^2} = s. \tag{5.36}$$

Therein, the additional diffusivity

$$\bar{d} = \beta \frac{v h}{2} = \beta d Pe \quad \text{with} \quad \beta = \left(\coth Pe - \frac{1}{Pe} \right) \tag{5.37}$$

only depends on the coefficients of the governing differential equation (5.23) and the element size h . In order to reduce the numerical costs of repetitively calculating the hyperbolic cotangent of the Péclet numbers, it is convenient to use the doubly asymptotic approximation

$$\beta \approx \min \left\{ 1, \frac{Pe}{3} \right\}. \tag{5.38}$$

Remark: The truncation error of the standard Galerkin method is represented by the diffusion coefficient \bar{d} as a function of Pe . According to Donea & Huerta [32], instead of (5.23), the Galerkin method provides an exact nodal solution for

$$v \frac{d\phi}{dx} - \left(d - \bar{d} \frac{\sinh^2(Pe)}{Pe^2} \right) \frac{d^2\phi}{dx^2} = s. \quad (5.39)$$

Thereby,

$$\lim_{Pe \rightarrow 0} \left(\bar{d} \frac{\sinh^2(Pe)}{Pe^2} \right) = 0,$$

ensures downward compatibility for a pure diffusive transport, which can be discretised exactly within the Galerkin method.

5.2.1 Stabilisation approaches

The further procedure is based on the finding from (5.36) that the Galerkin method can be stabilised by adding a numerical diffusivity \bar{d} , in order to induce the so-called artificial diffusion. The following considerations of different stabilisation methods proceed from the 3-d, stationary convection-diffusion equation

$$\mathbf{v} \cdot \text{grad } \phi - \text{div}[(\mathbf{D} + \tilde{\mathbf{D}}) \text{grad } \phi] = s. \quad (5.40)$$

Therein, \mathbf{v} and $\mathbf{D} = d\mathbf{I}$ are the velocity vector and the diffusivity tensor, respectively. Moreover, $\tilde{\mathbf{D}}$ is an additional artificial diffusivity tensor.

Isotropic artificial diffusion

In a first approach, the additional diffusivity is introduced via $\tilde{\mathbf{D}} := \tilde{d}\mathbf{I}$, which implies an isotropic artificial diffusion (IAD) with a scalar-valued diffusion coefficient \tilde{d} . Here, analogously to the 1-d equations, \tilde{d} is given by

$$\tilde{d} := \min\left\{1, \frac{\tilde{P}e}{3}\right\} d \tilde{P}e, \quad \text{where} \quad \tilde{P}e = \frac{\max\{v_1 h_1, v_2 h_2, v_3 h_3\}}{2d}. \quad (5.41)$$

Therein, $\{v_1, v_2, v_3\}$ are the components of the velocity vector \mathbf{v} and $\{h_1, h_2, h_3\}$ are the expansions of the element in the three spatial directions.

This isotropic approach for the artificial diffusion suffers from an effect, which is called crosswind diffusion. It appears, when the direction of the generated artificial diffusion is not aligned with the convection velocity. This crosswind diffusion does not affect the stabilisation of the problem, but has a strong negative effect on the accuracy of the results.

Nevertheless, the weak form of (5.40) with isotropic artificial diffusion reads

$$\underbrace{\int_{\Omega} [\delta\phi (\mathbf{v} \cdot \text{grad } \phi - s) + \text{grad } \delta\phi \cdot (\text{grad } \phi) d] dv - \int_{\Gamma} \delta\phi d \text{grad } \phi \cdot \mathbf{n} da}_{\text{Standard Galerkin}} + \underbrace{\int_{\Omega} \text{grad } \delta\phi \cdot (\text{grad } \phi) \tilde{d} dv}_{\text{Stabilisation term}} = 0. \quad (5.42)$$

Note that as the perturbation which is added to the test function is discontinuous at the element interfaces, the stabilisation is only applied in the element interiors and not on the boundary term (cf. Donea & Huerta [32], Ilinca *et al.* [78]).

Concerning the fluid energy balance, the artificial diffusivity \tilde{d}_{θ^F} is found according to (5.41) as

$$\tilde{d}_{\theta^F} = \min\left\{1, \frac{\tilde{P}e_{\theta^F}}{3}\right\}^* \tilde{P}e_{\theta^F} \quad \text{with} \quad \tilde{P}e_{\theta^F} = \frac{\max\{v_1^* h_1, v_2^* h_2, v_3^* h_3\}}{2d^*}, \quad (5.43)$$

where $\{v_1^*, v_2^*, v_3^*\}$ are the components of the vector \mathbf{v}^* . Therefore, the weak form of the IAD-stabilised fluid energy balance reads

$$\mathcal{G}_{\theta^F} + \int_{\Omega} \text{grad } \delta\theta^F \cdot (\text{grad } \theta^F) \tilde{d}_{\theta^F} dv = 0. \quad (5.44)$$

Streamline upwind diffusion

To overcome the issue of crosswind diffusion, a streamline upwind (SU) scheme is introduced. Therefore, the additional diffusion tensor

$$\tilde{\mathbf{D}} := \tilde{d} \frac{1}{|\mathbf{v}|^2} \mathbf{v} \otimes \mathbf{v} \quad (5.45)$$

depends on the direction of the convection velocity (cf. Brooks & Hughes [25]), while the definition of \tilde{d} still holds, see (5.41). With this SU diffusion approach, it follows for the weak form of (5.40)

$$\underbrace{\int_{\Omega} [\delta\phi (\mathbf{v} \cdot \text{grad } \phi - s) + \text{grad } \delta\phi \cdot (\text{grad } \phi) d] dv - \int_{\Gamma} \delta\phi d \text{grad } \phi \cdot \mathbf{n} da}_{\text{Standard Galerkin}} + \underbrace{\int_{\Omega} \frac{\tilde{d}}{|\mathbf{v}|^2} (\mathbf{v} \cdot \text{grad } \delta\phi)(\mathbf{v} \cdot \text{grad } \phi) dv}_{\text{SU stabilisation term}} = 0. \quad (5.46)$$

With the anisotropic auxiliary diffusion, the deviation from the original Galerkin scheme is smaller due to the absence of crosswind diffusion, but it fails in removing overshoots and undershoots in the vicinity of steep layers, cf., e. g., John & Knobloch [80]. Reformulating (5.46) yields

$$\int_{\Omega} [\widetilde{\delta\phi} (\mathbf{v} \cdot \text{grad } \phi) - \delta\phi s + \text{grad } \delta\phi \cdot (\text{grad } \phi) d] dv - \int_{\Gamma} \delta\phi d \text{grad } \phi \cdot \mathbf{n} da = 0. \quad (5.47)$$

Therein,

$$\widetilde{\delta\phi} = \delta\phi + \frac{\tilde{d}}{|\mathbf{v}|^2} \mathbf{v} \cdot \text{grad } \delta\phi \quad (5.48)$$

is a modified test function that is only applied on the term which is related to the convection process. This leads to a non-residual formulation, which is known to produce inaccurate or wrong results if the source term becomes significant (cf. Ilinca *et al.* [78]).

Nevertheless, with

$$\widetilde{\delta\theta^F} = \frac{\tilde{d}^*}{|\mathbf{v}^*|^2} (\mathbf{v}^* \cdot \text{grad } \delta\theta^F), \quad (5.49)$$

the weak form of the SU-stabilised fluid energy balance reads

$$\mathcal{G}_{\theta^F} + \int_{\Omega} \widetilde{\delta\theta^F} (\mathbf{v}^* \cdot \text{grad } \theta^F) dv = 0. \quad (5.50)$$

Streamline upwind Petrov-Galerkin scheme

By applying the same modified test function on all components in the sense of a Petrov-Galerkin method, Brooks & Hughes [25] overcame the inconsistency problem of the SU scheme. This approach is known as the streamline upwind Petrov-Galerkin (SUPG) method. Recalling (5.40), it follows for the weak form of the SUPG-stabilised convection-diffusion equation

$$\underbrace{\int_{\Omega} [\delta\phi (\mathbf{v} \cdot \text{grad } \phi - s) + \text{grad } \delta\phi \cdot (\text{grad } \phi) d] dv - \int_{\Gamma} \delta\phi d \text{grad } \phi \cdot \mathbf{n} da}_{\text{Standard Galerkin}} + \underbrace{\int_{\Omega} \frac{\tilde{d}}{|\mathbf{v}|^2} (\mathbf{v} \cdot \text{grad } \delta\phi) [\mathbf{v} \cdot \text{grad } \phi - \text{div}(d \text{grad } \phi) - s] dv}_{\text{SUPG stabilisation term}} = 0. \quad (5.51)$$

Note in passing that for linear basis functions, the term $\text{div}(d \text{grad } \phi)$ vanishes. Thus, in this case of a steady convection-diffusion equation, the only difference to the SU scheme would be the modified test function for the source term.

The fluid energy balance of the presented model is much more complex than the considered equations that are used here for the discussion of the numerical stabilisation. Nevertheless,

it will be shown in Chapter 6 that the SUPG method is very helpful to obtain satisfying results. So, finally, the weak form of the SUPG-stabilised fluid energy balance reads

$$\mathcal{G}_{\theta^F} + \int_{\Omega} \widetilde{\delta\theta^F} [\mathbf{v}^* \cdot \text{grad } \theta^F - d^* \text{div grad } \theta^F + \dot{s}^*] dv = 0. \quad (5.52)$$

Further methods

In recent decades, many new methods have been developed and already existing methods have been improved. A major group of approaches follows the idea of an additional stabilisation term for the standard Galerkin formulation. These include the Galerkin/least squares (GLS) method (Hughes *et al.* [77]), the subgrid scale (SGS) method (cf. Franca & Farhat [57], Hughes [75]), the characteristic Galerkin (CG) method (cf. Douglas & Russell [35], Pironneau [96]) and the Taylor-Galerkin (TG) method (Donea [31]). A very good overview for existing methods with their individual advantages and drawbacks is given by Donea & Huerta [32].

Chapter 6:

Numerical examples

Within this chapter, the set-up of the IBVP and the results of the numerical simulations are presented. After the determination of the material parameters, the different approaches for the numerical stabilisation of the fluid temperature distribution, discussed in the previous chapter, are evaluated by solving comparatively simple IBVP. Therefore, the finite-element mesh, consisting of hexahedral elements, is created with CUBIT¹ whereas the IBVP is solved with PANDAS. Due to the fact that the numerical effort for implicit FEM calculations strongly increases with the number of DOF, a parallelisation strategy is advised for larger IBVP. For this purpose, the parallel computing framework within Abaqus is used, while the element-wise evaluation of the material response is realised with PANDAS. This procedure has been presented by Schenke & Ehlers [106] and is applied here for the simulation of a full size EGS.

6.1 Material parameters and initial conditions

Within this section, suitable values for the remaining material parameters, initial conditions and further given values (cf. section 4.6) are presented. These values are assumed to stay constant during the whole simulation process. A summary is given in Table 6.1.

6.1.1 Fluid parameters

As already mentioned in Chapter 2, the temperature of a geothermal reservoir strongly depends on the geological conditions. For this work, a temperature of around 470 K ($\approx 200^\circ\text{C}$), measured at the geothermal plant at Soultz-sous-Forêts is used as the **initial fluid temperature** θ_0^F . The assumed dependency of the fluid density on the temperature (4.9) implies a **volumetric thermal expansion coefficient** $\alpha_V^F = 3\alpha^F$, which is a constant material parameter. The actually chosen value of $7 \cdot 10^{-4} \text{ K}^{-1}$ corresponds to the thermal expansion coefficient of water at about 100°C (cf. <http://physics.info/expansion2>). Based on the density of the reservoir fluid of 1060 kg/m^3 at 20°C (cf. Baujard & Bruel [9]) and the given thermal expansion coefficient α^F , an **initial real density** ρ_{0S}^{FR} of 935 kg/m^3 , considering the corresponding initial temperature, is computed. For the **dynamic fluid viscosity** μ^{FR} , a value of $2.8 \cdot 10^{-3} \text{ N s/m}^2$ is used, which corresponds to the viscosity of water at 100°C (cf. <http://physics.info/viscosity3>). Moreover, the **specific heat capacity** C_V^F is the amount of energy, that is needed to increase the temperature by 1 K. For this work, a value of 4220 J/(kg K) is used, which corresponds to the specific heat of

¹CUBIT (Sandia National Laboratories, Albuquerque, USA) is a geometry and mesh generation toolkit.

²Retrieved 25. 3. 2015.

³Retrieved 25. 3. 2015.

Initial temperatures	$\theta_0^F = 470 \text{ K}$ $\theta_0^S = 470 \text{ K}$
Initial real densities	$\rho_{0S}^{FR} = 935 \text{ kg/m}^3$ $\rho_{0S}^{SR} = 2600 \text{ kg/m}^3$
Initial solidity	$n_{0S}^S = 0.95$
Initial intrinsic permeability	$K_{0S}^S = 10^{-14} \text{ m}^2$
Lamé constants	$\mu^S = 2.16 \cdot 10^{10} \text{ kN/m}^2$ $\lambda^S = 2.16 \cdot 10^{10} \text{ kN/m}^2$
Dynamic fluid viscosity	$\mu^{FR} = 2.8 \cdot 10^{-4} \text{ N s/m}^2$
Thermal expansion coefficient	$\alpha_V^F = 3 \alpha^F = 7 \cdot 10^{-4} \text{ 1/K}$
Heat conduction coefficients	$H^{FR} = 0.679 \text{ W/(m K)}$ $H^{SR} = 3.2 \text{ W/(m K)}$
Specific heat capacities	$C_V^F = 4220 \text{ J/(kg K)}$ $C_V^S = 790 \text{ J/(kg K)}$
Specific surface area	$\omega = 0.12 \text{ m}^2/\text{m}^3$
Heat transfer coefficient	$k_\theta^{\varepsilon I} = 10^3 \text{ W/(m}^2 \text{ K)}$

Table 6.1: Material parameters and initial values.

water at 100 °C. Finally, the **heat conduction coefficient** H^{FR} is set to 0.679 W/(m K) (cf. [http://physics.info/conduction⁴](http://physics.info/conduction4)).

6.1.2 Solid parameters

For the **initial solid temperature** θ_0^S , in analogy to the initial temperature of the fluid, the measured temperature of the reservoir in Soultz-sous-Forêts is used. Due to the fact that the density of the solid is assumed to be constant, the real density ρ^{SR} is identical to the **initial real density** ρ_{0S}^{SR} , which is 2600 kg/m³ (cf. Doonechaly *et al.* [33]) for the rock in Soultz-sous-Forêts. According to Surma & Géraud [109], the porosity spans from 0.3 to 10 %. Therefore, an assumed average of 95 % is stated for the **initial solidity** n_{0S}^S . During the performed simulations, it has been found that an isotropic **initial intrinsic permeability** K_{0S}^S of 10^{-14} m^2 yields comparable flow rates as in Soultz-sous-Forêts, cf. subsection 6.3.1. The **Lamé constants** μ^S and λ^S are obtained from Valley [117] such that $\mu^S = \lambda^S = 2.16 \cdot 10^{10} \text{ kN/m}^2$. Following Surma & Géraud [109], the average **heat conduction coefficient** H^{SR} is 3.2 W/(m K). For the **specific heat capacity** C_V^S , the specific heat of granite is used, which is 790 J/(kg K).

⁴Retrieved 26. 3. 2015.

6.1.3 Heat transfer between solid and fluid

As already mentioned in section 4.5, the heat exchange between water and rock occurs at the interface within the cracks. Therefore, a parameter ω is needed that characterises the existing interface area per considered volume. Following Doonechaly *et al.* [33], at Soultz-sous-Forêts this specific surface is around $0.12 \text{ m}^2/\text{m}^3$. Furthermore, according to (4.32)₄ and (4.68), the heat exchange also depends on the temperature difference between the constituents and the **heat transfer coefficient** $k_\theta^{\varepsilon I}$. This coefficient is a characteristic parameter for the involved materials. For an interface between water and rock, a value of $10^3 \text{ W}/(\text{m}^2 \text{ K})$ (cf. Graf [67]) is assumed.

6.2 Evaluation of the stabilisation approaches

In order to determine the influence of the convection term within the fluid energy balance and the effect of the implemented methods for the numerical stabilisation, a brief set of three small examples is examined. The considered structure of the IBVP is based on the same principle for every example. Two surfaces are used for the in- and outflow, while all other boundaries are under undrained condition. The flow between the in- and the outflow boundary is induced by an applied pressure difference $p_L - p_R = 3 \cdot 10^4 \text{ N}/\text{m}^2$. Moreover, the solid displacement perpendicular to all boundaries is prevented. While the initial temperature is 470 K for both constituents within the entire domain, the fluid temperature at the inflow boundary is reduced by 100 K. The fluid temperature at the outflow boundary is held constant at 470 K, and for all other boundaries the heat flux \mathbf{q}^F is zero. Furthermore, the coupling between the temperatures is detached by setting the material parameter $k_\theta^{\varepsilon I} = 0$. The solid temperature is held constant, at all boundaries at 470 K and the gravitation is neglected. Except for the values of the initial intrinsic permeability $K_{0S}^S = 10^{-10} \text{ m}^2$ and, as already mentioned, the heat transfer coefficient $k_\theta^{\varepsilon I}$ all material parameters are applied according to Table 6.1.

Example 1

The domain of the first example is a simple beam, see Figure 6.1, where the length is 10 m and the width in the other two dimensions varies with the size of the cube-shaped finite elements.

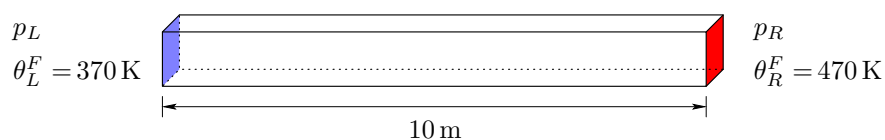


Figure 6.1: Example 1: Quasi 1-d IBVP.

The results of the fluid temperature after $2 \cdot 10^7$ seconds are shown in Figure 6.2 for different numbers of elements and, therefore, different element sizes. It turns out that smaller elements can reduce and eventually even avoid oscillations. In Table 6.2, the calculated Péclet number and the calculation time for the corresponding IBVP is given.

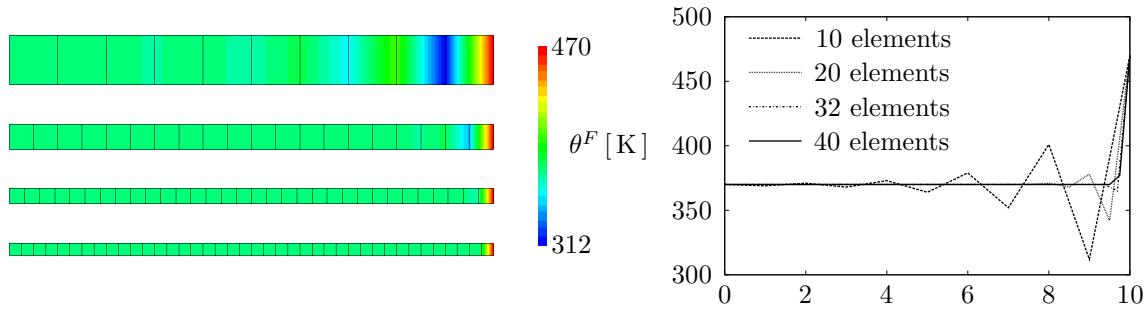


Figure 6.2: Example 1: The Fluid temperature of the quasi 1-d IBVP with 10, 20, 32 and 40 elements.

With the stabilisation techniques, presented in section 5.2, it is possible to ensure stable

	Péclet number [-]	CPU time [s]
10 elements	3.29 - 3.58	26
20 elements	1.66 - 1.77	50
32 elements	1.05 - 1.10	78
40 elements	0.84 - 0.88	95

Table 6.2: Example 1: Péclet numbers after $2 \cdot 10^7$ seconds and the required calculation time for different numbers of elements.

results even for the coarse mesh with only 10 elements. Here, in the case of a quasi 1-d IBVP, the IAD and the SU scheme are equivalent, and also the SUPG method provides almost exactly the same solution. The results from the stabilised and non-stabilised calculations are shown in Figure 6.3 for different numbers of elements. As expected, the

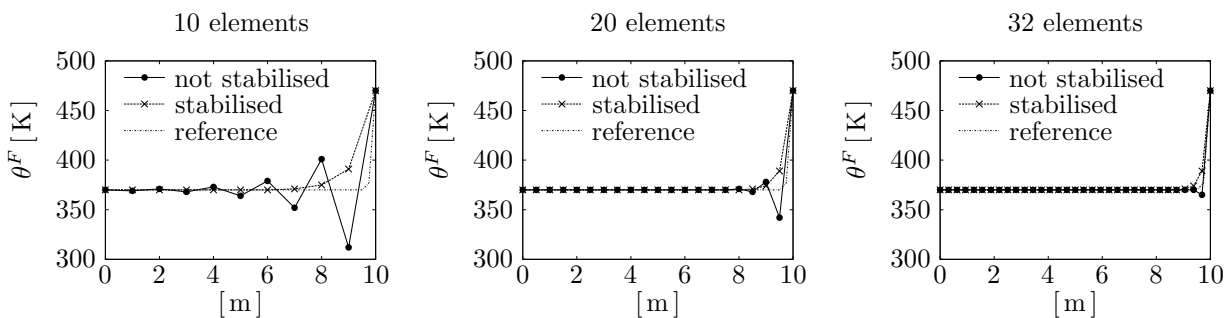


Figure 6.3: Example 1: Comparison between the fluid temperature obtained by the stabilised solution using 10, 20 and 32 elements and the non-stabilised reference solution using 40 elements.

gradient on the right-hand side is decreased by the stabilisation due to the additional diffusion. It can be stated that for larger elements more artificial diffusion is needed and, after all, the result is indeed smooth but, partly, far away from the correct solution. However, for smaller elements, the stabilised solution leads to acceptable results.

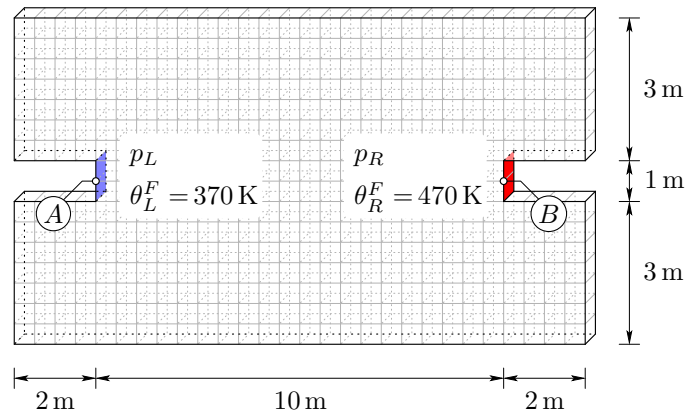


Figure 6.4: Example 2: IBVP, here illustrated with a mesh consisting of 376 elements.

Example 2

In order to evaluate the behaviour of the different approaches of numerical stabilisations, the geometry of the IBVP needs some modifications, see Figure 6.4. For a non-oscillating but also non-stabilised reference solution, the mesh has to be sufficiently fine. Thus, especially, in the areas where high gradients are expected, only very small elements can be used. For this purpose, a mesh, consisting of 6 256 elements, is used with highly varying element sizes. In detail, this means that the length of the element edge varies between approximately 1 cm at the in- and outflow surfaces and 1 m in less critical areas. Figure 6.5 shows the fluid temperature distribution after $1.5 \cdot 10^7$ seconds. However, oscillations occur even for this fine mesh in the further course of the calculation. To compare the different

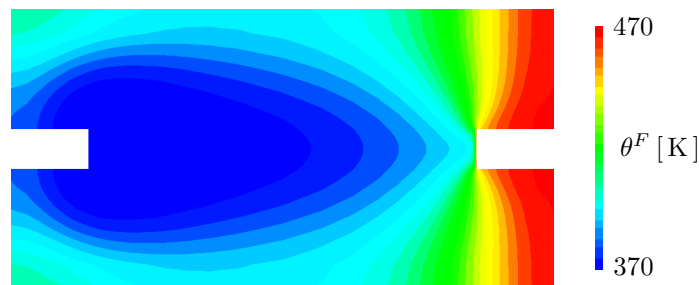


Figure 6.5: Example 2: Fluid temperature distribution after $1.5 \cdot 10^7$ seconds obtained from the non-stabilised simulation using 6 256 elements.

stabilisation approaches with the non-stabilised solution, the results for a coarse mesh consisting of only 376 cube-shaped elements is depicted in Figure 6.6. For the sake of a better comparability with Figure 6.5, the illustration of the fluid temperature in Figure 6.6 is limited to the range of 370 to 470 K, although, for the non-stabilised calculation, 170 K is actually the smallest value. The temperature distributions of the stabilised calculations are very smooth, whereas the non-stabilised calculation with 376 elements exhibits strong oscillations. As a consequence of the additional diffusivity that stabilises the result, the gradient of the fluid temperature is decreased in the region around the outflow boundary surface. Moreover, the coarse meshing prevents a more detailed representation of the temperature profile. This can be seen directly in Figure 6.6 as well as in the profile of the

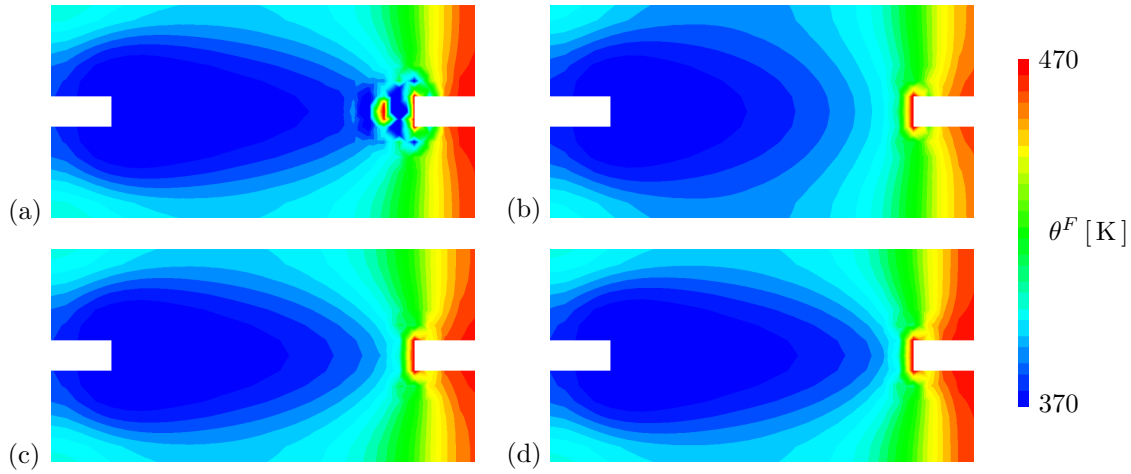


Figure 6.6: Example 2: Comparison of the fluid-temperature distribution after $1.5 \cdot 10^7$ seconds of (a) the non-stabilised calculation and the stabilised calculations with an (b) IAD, (c) SU and (d) SUPG stabilisation approach using 376 cube-shaped elements.

fluid temperature between the points *A* and *B*, which is shown in Figure 6.7. Moreover, a comparison of the IAD and the SU stabilised calculations shows the effect of crosswind diffusion.

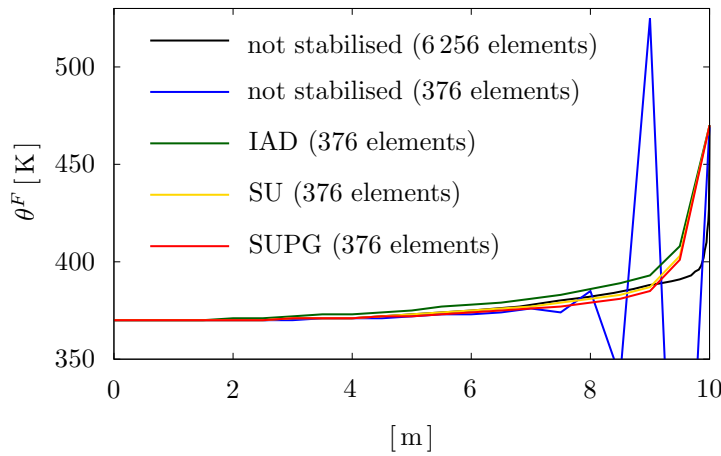


Figure 6.7: Example 2: Fluid-temperature profile between the points *A* and *B*.

Example 3

In order to show the difference between the SU and SUPG stabilisation, a third IBVP, depicted in Figure 6.8, is evaluated. The fluid-temperature distribution after $2 \cdot 10^6$ seconds resulting from stabilised and non-stabilised calculations on a coarse mesh, consisting of 36 elements, and a non-stabilised overkill solution using 3 600 elements is shown in Figure 6.9. Moreover, the corresponding fluid-temperature profile between the points *A* and *B* and the deviation from the overkill solution is given in Figure 6.10 for the stabilised and non-stabilised calculations. It turns out that after $2 \cdot 10^6$ seconds the fluid temperature is

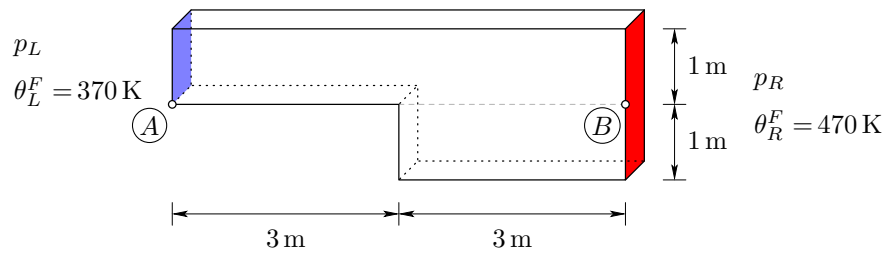


Figure 6.8: Example 3: IBVP.

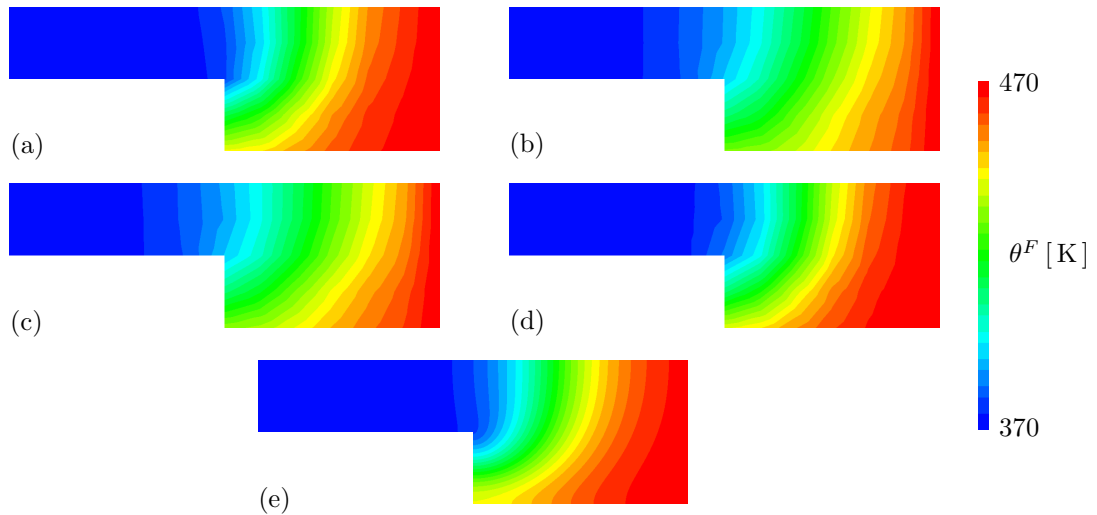


Figure 6.9: Example 3: Fluid-temperature distribution after $2 \cdot 10^6$ seconds for a calculation with 36 elements (a) without stabilisation, stabilised via (b) IAD, (c) SU, (d) SUPG, and (e) a non-stabilised overkill solution using 3600 elements.

still smooth and the solution is acceptable, even for the coarse mesh without stabilisation. At this point of the calculation, the non-stabilised calculation is actually more accurate as the IAD- and SU-stabilised calculations. Thus, apparently, the inconsistency of the IAD- and SU-stabilised calculations has, at least sometimes, a negative impact on the results, as the deviation of the SUPG-stabilised calculation is much smaller. Note, that

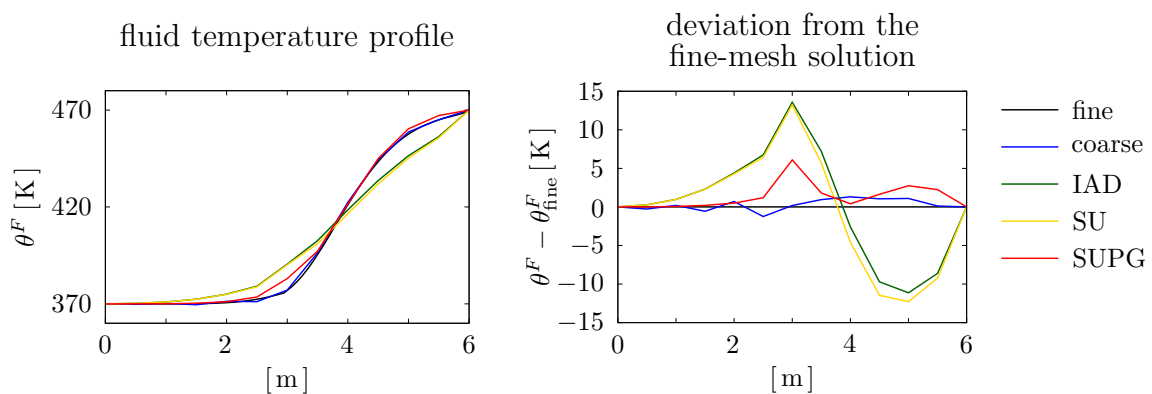


Figure 6.10: Example 3: Fluid-temperature profile and deviation between the stabilised and non-stabilised calculations with the coarse mesh (36 elements) and the fine mesh (3600 elements) overkill solution after $2 \cdot 10^6$ seconds between the points A and B.

in the further course of the simulation, the non-stabilised solution with the coarse mesh of course ends up with strong oscillations.

The three presented examples illustrate that it is not sufficient to use a numerical stabilisation to obtain reasonable results on arbitrary coarse meshes. In order to get acceptable solutions, it is rather necessary to draw on a sufficiently fine mesh, even if stabilisation methods are used. Nevertheless, the required mesh size can be significantly reduced by the use of a stabilisation technique.

6.3 Simulation of the subsurface of a geothermal power plant

In the first part of this section, the IBVP for the description of an EGS is explained. Thereby, the temporal sequence and the geometry is introduced. Moreover, the necessary permeability of the solid constituent is determined such that the ratio of the flow rate to the applied pressure corresponds to the known value of the circulation tests in Soultz-sous-Forêts. Subsequently, it is shown that, for this IBVP, only a stabilised calculation may provide acceptable results.

Afterwards, the results of the long-term simulation are presented. Here, in particular, the fluid temperature and its temporal and spatial behaviour plays an important role. Furthermore, other aspects such as the amount of produced thermal power and the temperature difference between the constituents are considered. Finally, the findings regarding the influence of the heat conduction and the occurring solid deformations are presented.

6.3.1 Set-up of the IBVP

For the following example, a two-well EGS is considered with one IW and one PW. Both wells reach a depth of 5 km with an open-hole length of 500 m each. The horizontal distance between the wells also amounts to 500 m. In order to reduce the numerical effort, the problem is split along the plane of symmetry, such that only one half of the EGS has to be considered for the simulation. Moreover, the roundness of the wells is neglected to avoid an unnecessarily complicated meshing. Instead, the inflow and the outflow takes place via corresponding partial areas of the plane of symmetry. Unfortunately, it is not possible to reduce the width of these areas to 35 cm, which would correspond to the half circumference of the Soultz' wells. The reason is that in this case too many elements would be needed such that the problem cannot be solved with the available hardware or within an acceptable period of time. This problem exists despite the fact that the mesh in the area of the wells is much finer, in order to account for the very different length dimensions and precision requirements. Moreover, a stronger variation of the element size again leads to numerical instabilities. Consequently, a well width of 1 m was necessary to obtain acceptable results in a more or less reasonable time. Furthermore, in the context of this IBVP the influence from gravity as an action from the distance is not taken into account. This decision has been made after it was seen that using realistic dimensions for

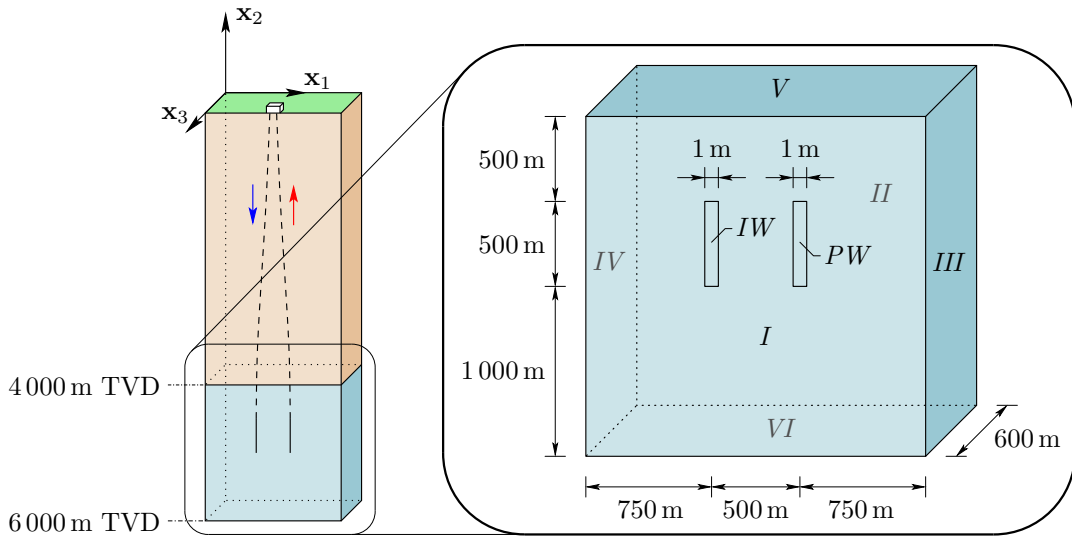


Figure 6.11: Geometry and the boundary numbering of the IBVP representing the EGS.

the wells in the presence of the gravitational forces makes an efficient numerical treatment formidable. The height of the in- and outflow areas still matches the open-hole length of 500 m. The geometry of the example is shown in Figure 6.11. Note in passing that the dimensions in the illustration are not to scale. In order to avoid the need to consider an unnecessarily large spatial domain, the weight of 4000 metres underground is applied as a load on the top of the IBVP (side V). This is done taking into account that the bottom-hole depth is at 5000 m TVD.

The initial value for the pressure p is set to 46.75 MPa, which is the corresponding hydrostatic pressure in a depth of 5 km, assuming $\rho^{FR} = 935 \text{ kg/m}^3$ and $|\mathbf{g}| = 10 \text{ m/s}^2$. The initial temperature of the solid and the fluid is 470 K.

The simulation is divided into three steps:

- Step 1:** Consolidation of the domain through the applied load on the surface V .
- Step 2:** Initialisation of the water flow between IW and PW by applying the pressure difference between the wells.
- Step 3:** Actual simulation of the operating EGS by lowering the temperature at the IW.

At the beginning of **Step 1**, a load of 94 MPa is applied on V . In the meanwhile, the pressure and the temperatures are held constant at all boundaries, according to their initial values. Except for the boundary V , at all other boundaries, the displacement perpendicular to the surface is prevented. The boundary conditions related to the momentum balance are kept unchanged for all steps. After $1.56 \cdot 10^7$ seconds (≈ 6 months), the consolidation process is completed.

During **Step 2**, the pressure at the IW is increased and the pressure at the PW is lowered. This adjustment of pressure is made linearly over the step. Finally, the pressure at the IW $p_{IW} = 55.14 \text{ MPa}$ is comprised of the overpressure of 5 MPa at the well head, and the hydrostatic pressure, which is calculated, according to (4.9), with a fluid density that corresponds to a temperature of 370 K. From the hydrostatic pressure with $\rho^{FR} = 935 \text{ kg/m}^3$ and a well head pressure of 1.8 MPa results the pressure for the PW

	<i>I</i>	<i>II</i>	<i>III</i>	<i>IV</i>	<i>V</i>	<i>VI</i>	<i>IW</i>	<i>PW</i>
MF	$p = 46.75 \text{ MPa}$							
MM ₁	$\bar{t}_1 = 0 \text{ MPa}$	$u_1 = 0 \text{ m}$		$\bar{t}_1 = 0 \text{ MPa}$				
MM ₂	$\bar{t}_2 = 0 \text{ MPa}$			$\bar{t}_2 = 94 \text{ MPa}$	$u_2 = 0 \text{ m}$	$\bar{t}_2 = 0 \text{ MPa}$		
MM ₃	$u_3 = 0 \text{ m}$	$\bar{t}_3 = 0 \text{ MPa}$				$u_3 = 0 \text{ m}$		
EF	$\theta^F = 470 \text{ K}$							
ES	$\theta^S = 470 \text{ K}$							

Table 6.3: Step 1: Boundary conditions for the mass balance of the fluid (MF), the three directions of the momentum balance of the mixture (MM_{*i*}), as well as the energy balances of the fluid (EF) and the solid (ES).

$p_{PW} = 48.55 \text{ MPa}$. It is further assumed, that the use of the LSP within the PW reduces this value to 44.35 MPa . From Step 2 on, all other boundaries, except the IW and PW, are undrained. The temperatures still remain constant on all boundaries at 470 K . Step 2 lasts for $3.12 \cdot 10^7$ seconds (≈ 12 months).

With the beginning of **Step 3**, the fluid temperature at the IW is reduced instantly to 370 K . Moreover, the solid temperature is held constant at 470 K at the bottom, namely boundary *VI*, to support the energy flux into the reservoir. It is assumed that no heat flux occurs perpendicular to all other boundaries, neither in the fluid nor within the solid. During this step, the development of the reservoir is simulated over a period of $1.56 \cdot 10^9$ seconds (≈ 50 years).

As described in section 4.2, the pressures p and the effective pore pressure p^{FR} are equal for $\theta^S = \theta^F$. Thus, in the moment of the temperature reduction the pressure at the boundary of the IW is underestimated by about 20 percent. However, due to the rapid cooling of the rock caused by the large temperature difference between the components, this deviation is practically no longer relevant from the next time step on.

The boundary conditions for the mass balance of the fluid, the three directions of the momentum balance of the mixture, and the energy balances of the fluid and the solid are summarised in Table 6.3–6.5. Therein, the values that are adopted unchanged from the last step are written in grey.

Meshing and parallelisation

The occurring length dimensions in the IBVP, range from several kilometres of the outer dimensions to the comparatively small diameter of the wells. This circumstance leads to a vast amount of elements that are required for an adequate meshing around the wells. Unfortunately, the use of tetrahedral elements is not possible, since in this case the stabilisation does not provide satisfactory results. Therefore, the meshing is additionally complicated due to the restriction to hexahedron elements. The wells are discretised with 2 elements in the horizontal direction and 20 elements in the vertical direction. The discretisation of the whole domain consists of $2.4 \cdot 10^5$ elements and $5.1 \cdot 10^5$ nodes. To

	<i>I</i>	<i>II</i>	<i>III</i>	<i>IV</i>	<i>V</i>	<i>VI</i>	<i>IW</i>	<i>PW</i>
MF	$\bar{m} = 0 \text{ kg}/(\text{m}^2 \text{ s})$						$p_{IW}(t)$	$p_{PW}(t)$
MM ₁	$\bar{t}_1 = 0 \text{ MPa}$	$u_1 = 0 \text{ m}$		$\bar{t}_1 = 0 \text{ MPa}$				
MM ₂	$\bar{t}_2 = 0 \text{ MPa}$			$\bar{t}_2 = 94 \text{ MPa}$	$u_2 = 0 \text{ m}$	$\bar{t}_2 = 0 \text{ MPa}$		
MM ₃	$u_3 = 0 \text{ m}$	$\bar{t}_3 = 0 \text{ MPa}$				$u_3 = 0 \text{ m}$		
EF	$\theta^F = 470 \text{ K}$							
ES	$\theta^S = 470 \text{ K}$							

Table 6.4: Step 2: Boundary conditions for the mass balance of the fluid (MF), the three directions of the momentum balance of the mixture (MM_{*i*}), as well as the energy balances of the fluid (EF) and the solid (ES).

	<i>I</i>	<i>II</i>	<i>III</i>	<i>IV</i>	<i>V</i>	<i>VI</i>
MF	$\bar{m} = 0 \text{ kg}/(\text{m}^2 \text{ s})$					
MM ₁	$\bar{t}_1 = 0 \text{ MPa}$	$u_1 = 0 \text{ m}$		$\bar{t}_1 = 0 \text{ MPa}$		
MM ₂	$\bar{t}_2 = 0 \text{ MPa}$			$\bar{t}_2 = 94 \text{ MPa}$	$u_2 = 0 \text{ m}$	
MM ₃	$u_3 = 0 \text{ m}$	$\bar{t}_3 = 0 \text{ MPa}$				
EF	$\bar{q}^F = 0 \text{ W}/\text{m}^2$					
ES	$\bar{q}^S = 0 \text{ W}/\text{m}^2$					$\theta^S = 470 \text{ K}$

	<i>IW</i>	<i>PW</i>
MF	$p_{IW} = 55.14 \text{ MPa}$	$p_{PW} = 44.35 \text{ MPa}$
MM ₁	$\bar{t}_1 = 0 \text{ MPa}$	
MM ₂	$\bar{t}_2 = 0 \text{ MPa}$	
MM ₃	$u_3 = 0 \text{ m}$	
EF	$\theta^F = 370 \text{ K}$	$\bar{q}^F = 0 \text{ W}/\text{m}^2$
ES	$\bar{q}^S = 0 \text{ W}/\text{m}^2$	

Table 6.5: Step 3: Boundary conditions for the mass balance of the fluid (MF), the three directions of the momentum balance of the mixture (MM_{*i*}), as well as the energy balances of the fluid (EF) and the solid (ES).

handle the resulting $1.92 \cdot 10^6$ DOF within an acceptable time frame, it is necessary to run the simulation in a parallelised framework. Therefore, according to Schenke [105] and Schenke & Ehlers [106], PANDAS is compiled in the sense of a library, and provides, within an Abaqus calculation, the element-wise contributions to the overall system of equations. This system of equations is subsequently solved on 160 processors⁵ within

⁵5 x AMD Opteron 6308, 3.5 GHz, 32 cores, 265 GB RAM.

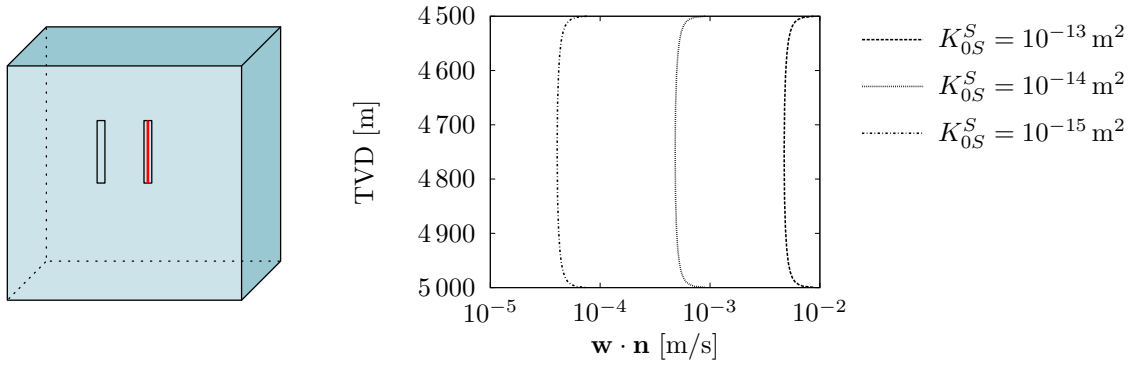


Figure 6.12: The resulting outward oriented part of the seepage velocity at the PW depending on the depth for different permeabilities.

Abaqus. For one iteration, $3.08 \cdot 10^{14}$ floating point operations are required for the solution of the system, which lasts for about 800 seconds on the used high-performance computing cluster. Furthermore, also the element evaluations are accomplished in parallel. In Step 1 and Step 2 up to 6 iterations are necessary for the calculation of the equilibrium state, whereas, for Step 3 only 2 iterations are needed. Eventually, considering further time consuming operations such as the element evaluation and the writing of the results, the overall duration of the simulation is $1.46 \cdot 10^6$ seconds, which is almost 17 days. A pleasant side effect of this procedure is the fact that for the pre- and postprocessing the convenient user interface of **Abaqus/CAE** can be used. Thereby, the additional PV fluid pressure, fluid and solid temperature are formally treated as temperatures during the preprocessing.

Determination of the intrinsic permeability

It is known from the considered circulation test in Soultz-sous-Forêts that for a well-head pressure of 5 MPa at the IW and 1.8 MPa at the PW, the in- and outflow amounts to approximately 25 l/s. Therefore, before the actual simulation can start, the appropriate intrinsic permeability has to be determined. For this purpose, the outflow at the PW was observed while running the simulation with different permeabilities of $K_{0S}^S = 10^{-13} \text{ m}^2$, $K_{0S}^S = 10^{-14} \text{ m}^2$ and $K_{0S}^S = 10^{-15} \text{ m}^2$. The resulting outward oriented part of the seepage velocity ($\mathbf{w}_F \cdot \mathbf{n}$), depending on the depth of the according open-hole section of the PW, for each of the three simulations is shown in Figure 6.12. The overall outflow of mass

$$\bar{M} = \int_{A_{PW}} \bar{m} \, da = \int_{A_{PW}} n^F \rho^{FR} \mathbf{w}_F \cdot \mathbf{n} \, da. \quad (6.1)$$

is given by the integral of the local mass flow through the surface area A_{PW} of the PW. The corresponding results of the simulations are:

$$\begin{aligned} K_{0S}^S = 10^{-13} \text{ m}^2 & \quad \rightarrow \quad \bar{M} = 116.92 \text{ kg/s}, \\ K_{0S}^S = 10^{-14} \text{ m}^2 & \quad \rightarrow \quad \bar{M} = 11.91 \text{ kg/s}, \\ K_{0S}^S = 10^{-15} \text{ m}^2 & \quad \rightarrow \quad \bar{M} = 1.00 \text{ kg/s}. \end{aligned} \quad (6.2)$$

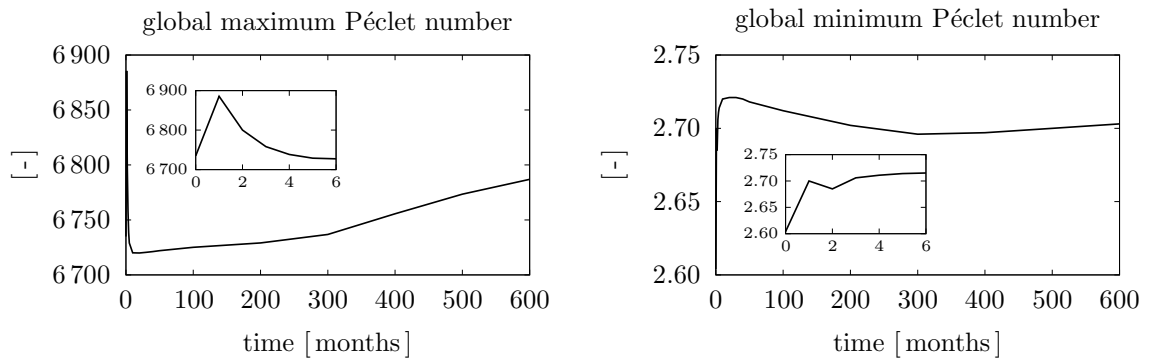


Figure 6.13: Evolution of the maximum and the minimum Péclet number of all nodes at every time step of Step 3.

For the volume flow of $25 \text{ l/s} \hat{=} 0.025 \text{ m}^3/\text{s}$ through the PW, the corresponding mass flow is 23.375 kg/s for a fluid density $\rho^{FR} = 935 \text{ kg/m}^3$. Due to the symmetry, for the actual simulation an overall mass flow of about 11.7 kg/s is expected. Thus, it is suitable, to use an intrinsic permeability of $K_{0S}^S = 10^{-14} \text{ m}^2$ for further simulations.

Péclet number and necessity of stabilisation

As it has been discussed in section 5.2, the numerical implementation based on a non-stabilised standard Galerkin scheme may lead to oscillations for Péclet numbers greater than one. In order to evaluate the necessity of a stabilisation of the fluid temperature for this IBVP, the global maximum and minimum of all Péclet numbers calculated for every node of the IBVP are shown in Figure 6.13 for every time step. These values are obtained from a stabilised calculation, which means that the actual values of a non-stabilised calculation might slightly differ, but are of the same order of magnitude. It can be seen that the minimum value is greater than zero, although the Péclet number of the nodes in the corner of the IBVP should equal zero, since at this points, there is no flow of the water, such that $|\mathbf{w}_F| = 0$. This originates in the calculation of the Péclet number at the Gaussian points and the subsequent mapping of the values to the nodes. Thus, even if these values do not correspond to the expected ones, it shows that in any case the issue of Péclet numbers beyond one appear in the probably most unsuspected elements. Furthermore, the global maximum value is consistently above 6700. This circumstance and the fact that a non-stabilised calculation aborts at the first time step due to convergence problems makes unquestionably clear that only a stabilised calculation can provide acceptable results. Furthermore, as the Péclet number is mesh-dependent, an adequate refinement of the mesh should also lead to better results. However, the limitation of the computer hardware available for this simulation does not allow to solve the resulting problem within a reasonable time. Thus, this option is not available at the moment and it is rather advisable to use the presented SUPG stabilisation approach for a smooth solution almost clear of oscillations.

6.3.2 Results of the long-term simulation

In order to investigate the long-term behaviour of the reservoir, a simulation is performed that shows the development of the reservoir for a time period of $1.56 \cdot 10^9$ seconds (≈ 50 years), with a time-step size of $2.6 \cdot 10^6$ seconds (\approx one month).

The **fluid-temperature distribution** is depicted in Figures 6.14–6.16 for various time steps. Here, Figure 6.14 shows the fluid temperature at 4 750 m TVD along the symmetry

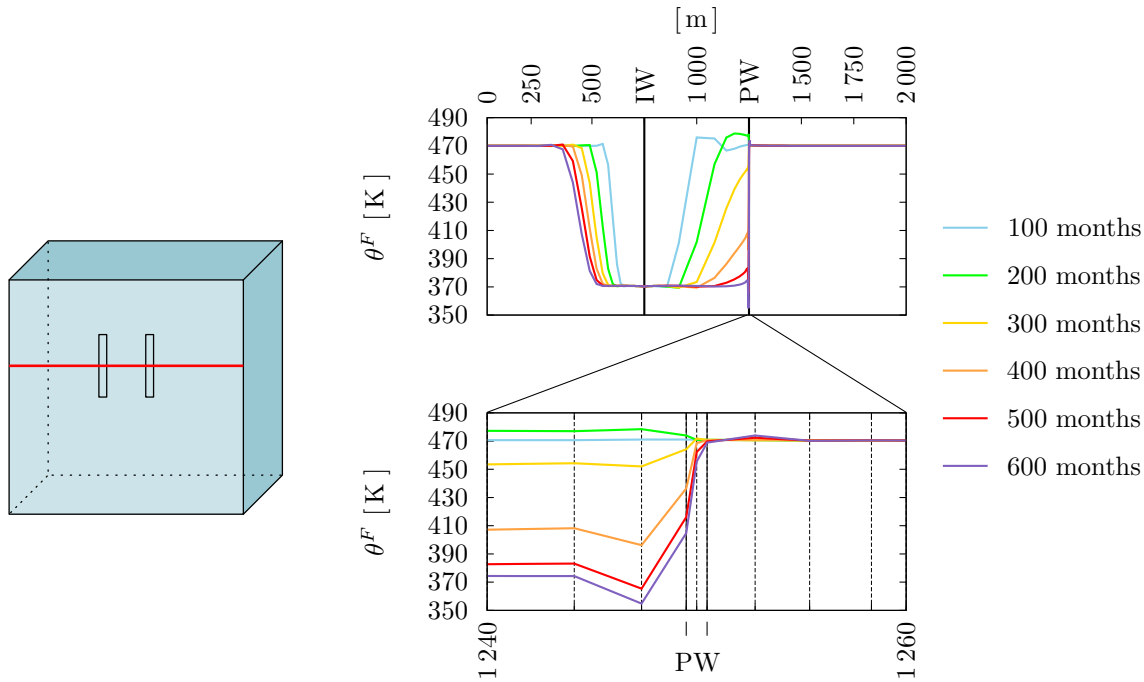


Figure 6.14: Fluid temperature at 4 750 m TVD along the symmetry plane and in the vicinity of the PW with element accurate resolution.

plane for the whole width of the IBVP and in the vicinity of the PW with an element accurate resolution. Moreover, Figure 6.15 and Figure 6.16 show the fluid-temperature distribution for a horizontal cut at 4 750 m TVD and at the plane of symmetry, respectively. It is found that the SUPG stabilisation is actually capable of severely limiting the oscillations. However, in the course of the simulation it becomes apparent that the oscillations can not be completely prevented in the vicinity of the PW. Furthermore, it can be seen that the temperature at the PW firstly decreases in the middle of the open-hole section at 4 750 m TVD. The temporal evolution of the fluid temperature at the PW in this depth is shown in Figure 6.17 for the three points A , B and C , which are also depicted in the figure. These points correspond with the discrete nodes on the left, between and on the right of the elements that discretise the well. It can be seen that for the first 25 years the temperature is almost constant. Afterwards, it decreases rapidly on the left side of the well. However, the right side is almost unchanged for the whole 50 years. This circumstance is a consequence of the idealisation of the problem. It can hardly be assumed that in reality such a large temperature gradient exists within a width of only one metre for the period of several decades. It is rather plausible to expect that the fluid

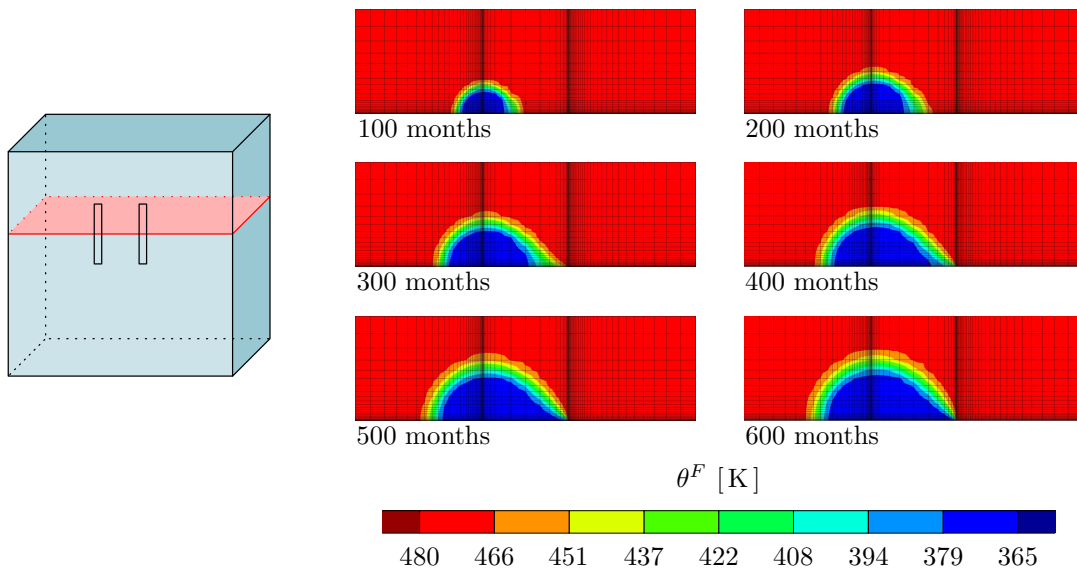


Figure 6.15: Fluid-temperature distribution at 4750 m TVD.

is already mixed and, therefore, has an averaged temperature when it emerges into the well. At this point, a probably permissible conclusion would be that the temperature of the extracted water at the PW decreases after about 25 years. The rapid, but slight

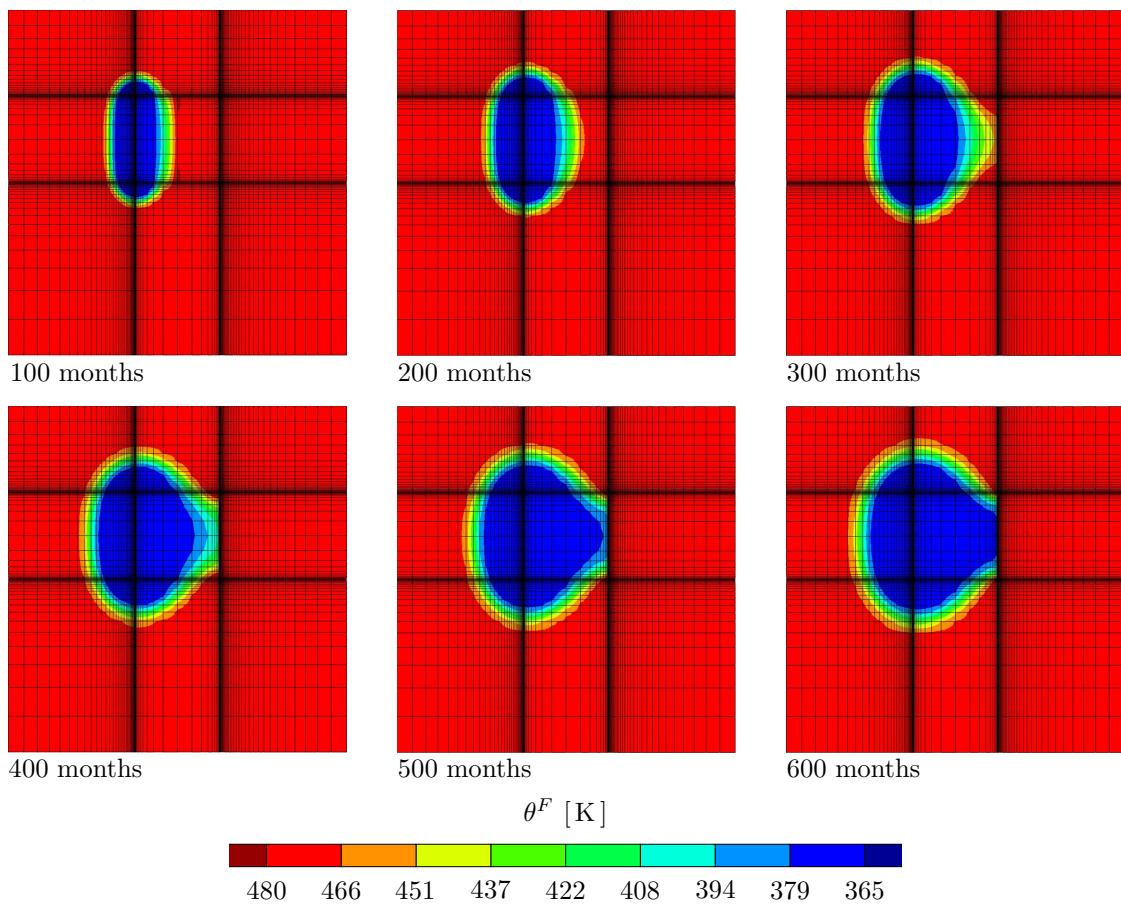


Figure 6.16: Fluid-temperature distribution at the plane of symmetry.

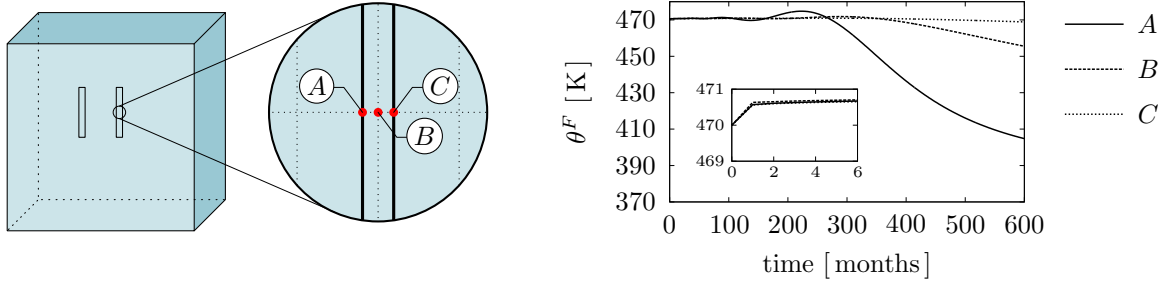


Figure 6.17: Evolution of the fluid temperature at the points A, B and C.

increase in temperature for the first time step of Step 3 is attributed to the fact that during Step 2 the temperature at the PW is held constant. Afterwards, dissipative effects like the friction between the fluid and the solid leads to slightly higher temperatures at the, henceforth, heat-flux-free boundary.

The produced **thermal gross power** P can be calculated based on the results of the simulation via

$$\begin{aligned}
 P &= C_V^F \int_{A_{PW}} \bar{m} (\theta^F - \theta_{IW}^F) da \\
 &= C_V^F \int_{A_{PW}} n^F \rho^{FR} \mathbf{w}_F \cdot \mathbf{n} (\theta^F - \theta_{IW}^F) da.
 \end{aligned} \tag{6.3}$$

Therein, θ_{IW}^F is the temperature of the fluid that is injected into the IW, which is here 370 K. The evolution of the gross power is depicted in Figure 6.18. It can be seen here that at the very beginning, the previously described increase of the fluid temperature at the PW for the first time step also has a small influence on the power production. Afterwards, a plateau follows for about 25 years. Subsequently, the thermal power is steadily declining and loses approximately 20 percent during the next 25 years. Overall, within the first 25 years about 4.1 PJ (petajoules) are produced, whereas throughout the following 25 years the output is only 3.7 PJ.

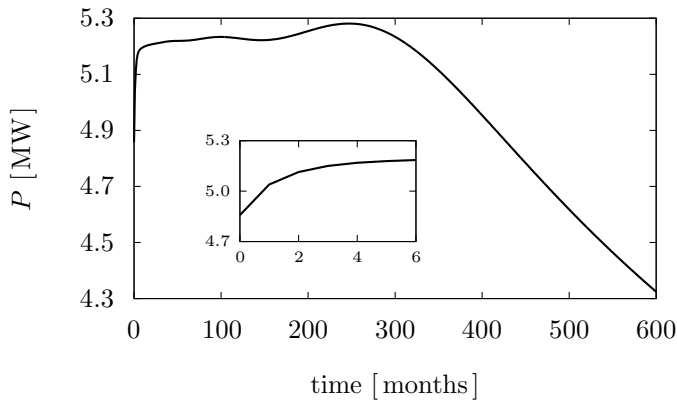


Figure 6.18: Evolution of the produced thermal gross power.

Further aspects

Due to the fact that the temperatures of the constituents are considered separately within this model, an examination of the **temperature difference** ($\theta^S - \theta^F$) is of interest. Therefore, in Figure 6.19, the absolute fluid temperature and the temperature difference between solid and fluid is shown for the point D half way between the wells at 4750 m TVD. It becomes apparent that the temperature difference is very small. For the whole

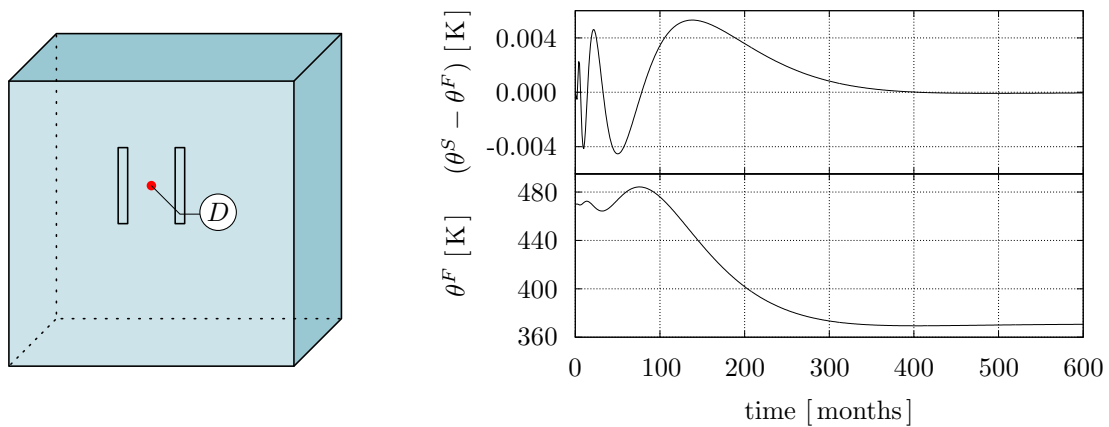


Figure 6.19: Fluid temperature and temperature difference between solid and fluid at point D .

IBVP, even in the areas with the largest remaining oscillation, an absolute value of 5 K is never exceeded. This means that for this IBVP with the given material parameters and boundary conditions, the assumption of a joint temperature is admissible. Nevertheless, it is shown that the physical process of heat exchange can be modelled with the considered governing equations and the including constitutive assumptions.

According to Fourier's law, the **heat flux** follows the negative gradient of the temperature. Thus, for the presented IBVP where the temperature distributions of the constituents are almost identical, the magnitude of heat conduction of the constituents differs only due to the different heat conduction coefficients. Therefore, the magnitude of the conduction within both constituents is composed in Figure 6.20 with the same pictures, but with different scales. The solid temperature at the bottom is held constant at 470 K with the intention of allowing an influx of heat from the outside of the area under consideration into the reservoir. During the evaluation of the simulation results, it turns out that this influx does not occur, since the cooled area has a very limited extend and the surrounding domain is thermally quasi unaffected. Overall, it can be summarised that the heat transport via conduction plays a strongly subordinate role compared to the convection process.

It can be seen through examination of the **solid displacement field** that the local strain caused by the fluid injection is very small. Nevertheless, due to the size of the IBVP, this strain results in a significant displacement. Especially the upper part of the domain is raised by the increase of porosity. In Figure 6.21, the vertical displacement of the upper edge is shown via the representative point E , since this curve looks nearly identical for all

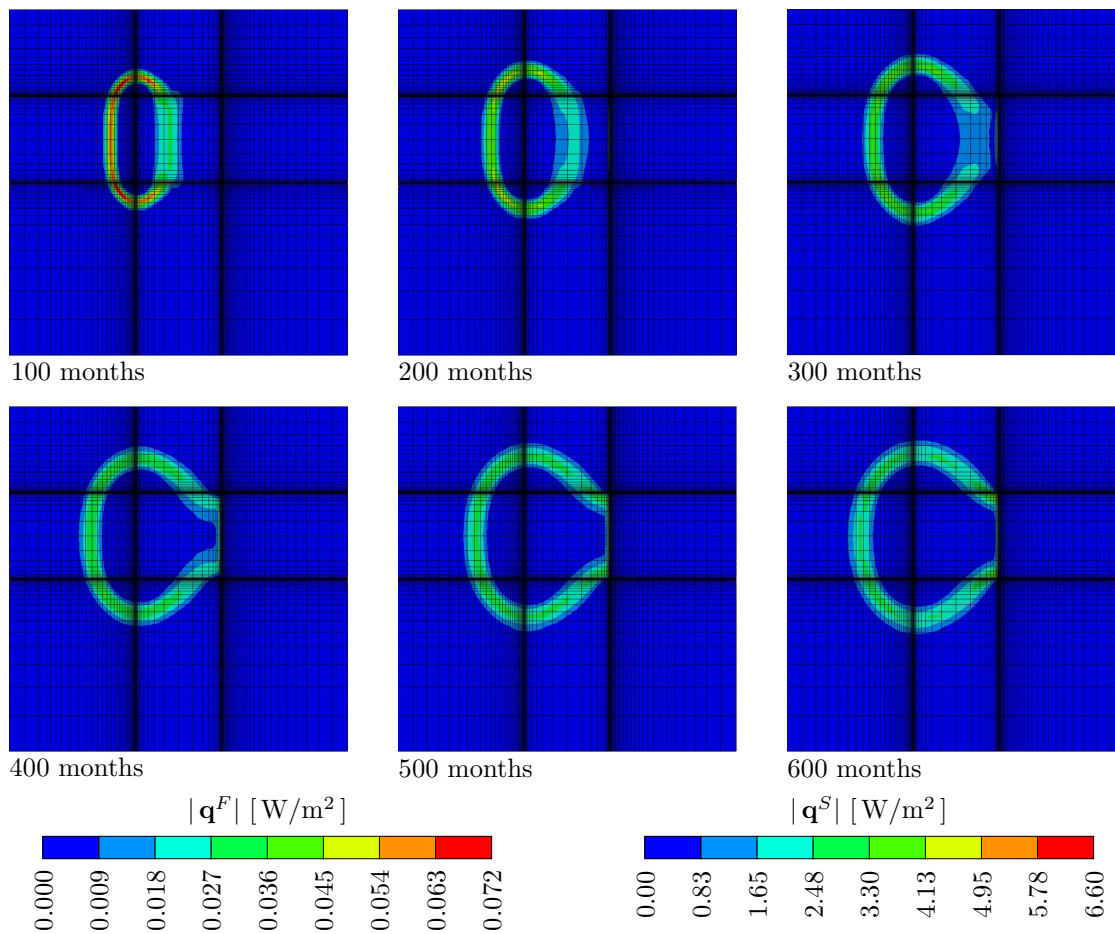


Figure 6.20: Magnitude of heat conduction within the constituents.

points of boundary V . During Step 1, the consolidation phase, the surface sinks by almost 1.5 metres. Afterwards, when the pressure difference for the actual operation is applied at the wells, point E rises again by about 10 cm. In a real application, the consolidation process has already been completed. However, it is found, hereby, that an uplift of the ground above the reservoir due to the fluid injection can not be excluded. Thus, the consideration of the solid deformation is indeed reasonable.

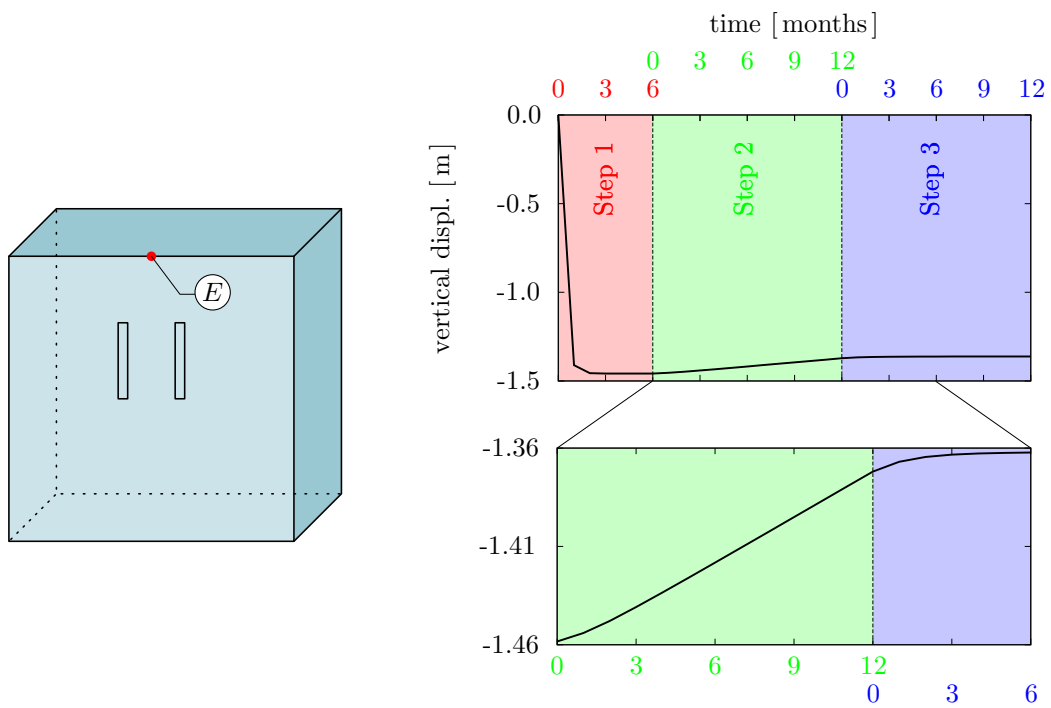


Figure 6.21: Vertical solid displacement of the top at point E .

Chapter 7:

Summary and Outlook

7.1 Summary

The main goal of this work was to develop a model for the simulation of the behaviour of a deep geothermal reservoir during heat extraction for the purposes of energy production. To fulfil this goal, it was firstly set out where this geothermal energy can be found and where it comes from. In addition, various possibilities for an exploitation of this energy source have been presented. In particular, the EGS were introduced and their construction and the physical processes during the operation were explained. These procedures have been exemplarily explained on the basis of the pilot power plant in Soultz-sous-Forêts. Thereby, starting from the description of the geological conditions, the hydraulic and chemical stimulation and the subsequent circulation tests were discussed.

In the frame of the TPM, a continuum-mechanical model has been developed, whose constituents consist of a solid skeleton and a pore fluid. These constituents represent the bedrock and the water that is injected into the subsurface, respectively. In order to explicitly consider the heat exchange between the components, the usual assumption of a uniform temperature was not made. Instead, the energy balance for each constituent has been recognised separately to determine the individual temperatures. Moreover, the linear momentum balance of the overall aggregate was used to identify the quasi-static displacement field of the elastic solid. The fluid flow was induced by a pressure difference between the wells, while the evolution of the pore pressure itself was determined via the mass balance of the fluid. It should be noted that assuming a temperature-dependent fluid density in the model prohibits the transformation of the fluid mass balance to the volume balance, as it is commonly the case. Furthermore, in order to ensure the thermodynamical consistency of the proposed model, an evaluation of the entropy inequality has been accomplished.

Following the idea of the method of weighted residua, the governing equations were transformed into their weak forms. Subsequently, the problem has been discretised in space and time using modified Taylor-Hood elements and the implicit Euler time-integration scheme, respectively. The resulting system of equations was solved in a monolithic manner using the parallel solver in **Abaqus**, whereas, the element-wise contributions to the overall system of equations are calculated by the in-house finite-element solver **PANDAS**.

It was observed that the chosen set of material parameters, boundary conditions and the size of the elements used for the spatial discretisation render the problem strongly convective. The numerical treatment of such a problem leads to oscillations in the computed fluid temperature. In order to overcome this issue, an appropriate numerical stabilisation technique had to be applied. For a better understanding of this phenomenon, at first, a simple one-dimensional example was considered. Following that, based on the idea

of artificial diffusion, three stabilisation approaches for suppressing the oscillations were introduced and their performances were compared.

For the actual simulation of the behaviour of an EGS reservoir over an extended period, the geometry of a three-dimensional IBVP consisting of one injection and one production well was defined. Firstly, in order to obtain a corresponding consolidated subsoil, a preliminary calculation was conducted, where the region of interest has been loaded on top by an adequate weight. The ensuing simulation of the operating EGS observed the development of the reservoir for a period of about 50 years, while hot water was extracted and colder water was re-injected.

The evaluation of the results showed that for this specific example, the temperature of the extracted water for a period of about 25 years remained almost constant. Afterwards, the temperature in the production well continuously decreased and, in accordance with it, the thermal power of the system was diminished. The results indicated that for this application, the distinction between the temperatures of the constituents is not necessarily required. Nevertheless, it was found that the heat exchange can be adequately modelled with the help of the chosen approaches. Moreover, it was also found that the strain of the solid constituent, which has been induced by the fluid injection, has been very small. However, due to the size of the reservoir, the small strain sum up to a significant uplift at the surface.

In summary, it can be said that simulations provide a chance for improving the predictions about the performance of a geothermal reservoirs and, further, allow an assessment concerning the efficiency of a power plant in advance.

7.2 Outlook

The presented work demonstrated successfully that it is possible to basically describe the thermal and mechanical behaviour of an EGS using the TPM. At this point, a next step could be the detailed analysis and, ideally, the removal of current limitations. As there is, for example, the so far constant initial temperatures that does not follow the geothermal gradient. This may be solved via another pre-computation, analogous to that of the consolidation process. Moreover, the influence of gravity and, thus, a resulting hydrostatic pressure profile in the wells could also be taken into account.

Furthermore, it would be interesting to use the model for the treatment of other related applications, like the simulation of hydrothermal systems. For this purpose, solely the initial and boundary conditions as well as the material parameters need to be changed. Potentially, the model could be used in general for the simulation of a porous heat exchanger which is perfused by a liquid.

The most limiting factor in the simulation of EGS was the enormous computational effort and, therefore, the restriction to a relatively coarse spatial discretisation. Hence, various approaches are described in the following in order to reduce the numerical effort.

It was seen that for the modelling of the herein-presented specific IBVP, the distinction of the individual constituent temperatures could be neglected. This would lead to a smaller

number of DOF but, however, would also prevent the consideration of the heat exchange between the constituents.

A further option would be the use of decoupling strategies based on operator-splitting or domain-decomposition techniques. As the name suggests, operator splitting breaks down the differential operator of the problem into several simpler sub-operators. This process leads to a splitting of the problem into a set of sub-problems, which could be integrated individually. As a result, one would be able to integrate the diffusive and convective parts of the problem separately and, thus, overcome the numerical difficulties as were discussed in section 5.2. Nevertheless, the process of splitting may destroy the dissipativity of the problem and, consequently, cause conditional stability. Therefore, a careful stability analysis of the resulting solution scheme would be inevitable, although, due to the complexity of the model, an evaluation of the stability of the solution is a great challenge.

In the domain decomposition, the considered spatial domain of the IBVP is divided into several subdomains. A big advantage here would be that the meshing is significantly easier, which is, however, paid with an increased effort needed for the coupling of the subdomains. Furthermore, also for this method, a stable solution is not guaranteed. More details about decoupling strategies and about the stability analysis of the decoupled solution methods can be found in Zinatbakhsh [124], Zinatbakhsh *et al.* [125] and Ehlers *et al.* [48], respectively.

Another approach might come from the field of model reduction, when, based on a proper orthogonal decomposition (POD) and the discrete empirical interpolation method (DEIM), the number of DOF is reduced, which, of course, corresponds with a reduced computation time. Due to the necessity of a pre-computation, this approach is particularly suitable for applications where calculations must be performed more often, such as in the context of optimisation and sensitivity studies. The utilisation of this method of model reduction to applications concerning the TPM are studied by Fink & Ehlers [56].

In the following, further approaches are described to extend the model in order to consider additional physical effects.

By incorporating the findings from the seismic observations during the stimulation, a heterogeneous permeability could be derived and, thus, the flow field can be simulated more accurately. In addition, by also taking the principal stress directions into account, even conclusions about the anisotropy of the permeability may be made. How a heterogeneous, anisotropic permeability within the TPM can be treated is described, *inter alia*, by Wagner [118].

Moreover, it would also be possible to simulate a system that operates with more wells. This would lead to a variety of possible combinations of IW and PW and it would be worthwhile to optimise the possible configurations in order to maximise the efficiency.

The model could further be extended to incorporate other physical effects. For example, the phenomenon of swelling could be considered which results from a chemical reaction of the subsoil with the infiltrating water. This phenomenon has occurred, among others, during the geothermal drilling in Staufen im Breisgau and has led to strong damage of buildings. One approach for the modelling of this phenomenon is presented by

Acartürk [1].

In the case where the subsurface is only partially saturated, also the gaseous phase must be considered. A TPM-based model for partially saturated soil is described by Avci [3]. To further allow phase change and, therefore, mass transfer between the constituents, the mass production term has to be considered as it is done, among others, by de Boer & Bluhm [19] and Häberle & Ehlers [71].

In order to additionally consider the process of hydraulic stimulation, modelling approaches from the fields of extended finite-element method (XFEM) described by Rempier [102], or the phase-field theory presented by Luo & Ehlers [86], could be used to simulate the initiation and propagation of cracks in the rock.

Bibliography

- [1] Acartürk, A.: *Simulation of Charged Hydrated Porous Materials*. Dissertation Thesis, Report No. II-18 of the Institute of Applied Mechanics (CE), University of Stuttgart, Stuttgart 2009.
- [2] Arihara, N.; Yoshida, H.; Hanano, M. & Ikeuchi, K.: A simulation study on hydrothermal system of the Kakkonda geothermal field. In *Proceedings, World Geothermal Congress*, Florence 1995, pp. 18–31.
- [3] Avci, O.: *Coupled Deformation and Flow Processes of Partially Saturated Soil: Experiments, Model Validation and Numerical Investigations*. Dissertation Thesis, Report No. II-26 of the Institute of Applied Mechanics (CE), University of Stuttgart, Stuttgart 2013.
- [4] Baehr, H. D. & Kabelac, S.: *Thermodynamik: Grundlagen und technische Anwendungen*. Springer Vieweg 2012.
- [5] Baria, R.; Baumgärtner, J.; Gérard, A.; Jung, R. & Garnish, J.: European HDR research programme at Soultz-sous-Forêts (France) 1987–1996. *Geothermics* **28** (1999), 655–669.
- [6] Baria, R.; Michelet, S.; Baumgärtner, J.; Dyer, B.; Gérard, A.; Nicholls, J.; Hettkamp, T.; Teza, D.; Soma, N.; Asanuma, H.; Garnish, J. & Megel, T.: Microseismic monitoring of the world’s largest potential HDR reservoir. In *Proceedings, Twenty-Ninth Workshop on Geothermal Reservoir Engineering, Stanford University*, Stanford 2004, pp. 194–201.
- [7] Bathe, K.-J.: *Finite Element Procedures*. 2nd edn. Prentice Hall, Englewood Cliffs 1996.
- [8] Bathe, K.-J.: *Finite-Elemente-Methoden*. 2nd edn. Springer-Verlag, Berlin 2002.
- [9] Baujard, C. & Bruel, D.: Numerical study of the impact of fluid density on the pressure distribution and stimulated volume in the Soultz HDR reservoir. *Geothermics* **35** (2006), 607–621.
- [10] Baumgärtner, J.; Gérard, A.; Baria, R.; Jung, R.; Tran-Viet, T.; Gandy, T.; Aquilina, L. & Garnish, J.: Circulating the HDR reservoir at Soultz: maintaining production and injection flow in complete balance. In *Proceedings, Twenty-Third Workshop on Geothermal Reservoir Engineering, Stanford University*, Stanford 1998, pp. 11–20.
- [11] Baumgärtner, J.; Jung, R.; Gérard, A.; Baria, R. & Garnish, J.: The european HDR project at Soultz-sous-Forêts: Stimulation of the second deep well and first circulation experiments. In *Proceedings, Twenty-First Workshop on Geothermal Reservoir Engineering, Stanford University*, Stanford 1996, pp. 267–274.

- [12] Belytschko, T.; Liu, W. K. & Moran, B.: *Nonlinear Finite Elements for Continua and Structures*. John Wiley & Sons, Chichester 2000.
- [13] Benson, S.; Daggett, J.; Iglesias, E.; Arellano, V. & Ortiz-Ramirez, J.: Analysis of thermally induced permeability enhancement in geothermal injection wells. In *Proceedings, Twelfth Workshop on Geothermal Reservoir Engineering, Stanford University, Stanford 1987*, pp. 57–65.
- [14] Biot, M. A.: General theory of three-dimensional consolidation. *Journal of Applied Physics* **12** (1941), 155–164.
- [15] Bluhm, J.: Modelling of saturated thermo-elastic porous solids with different phase temperatures. In Ehlers, W. & Bluhm, J. (eds.): *Porous Media: Theory, Experiments and Numerical Applications*. Springer-Verlag, Berlin 2002, pp. 87–118.
- [16] de Boer, R.: *Vektor- und Tensorrechnung für Ingenieure*. Springer-Verlag, Berlin 1982.
- [17] de Boer, R.: *Theory of Porous Media*. Springer-Verlag, Berlin 2000.
- [18] de Boer, R.: *Trends in Continuum Mechanics of Porous Media, Vol. 18*. Theory and applications of transport in porous media, Springer, Dordrecht 2005.
- [19] de Boer, R. & Bluhm, J.: Phase transitions in gas and liquid-saturated porous solids. *Transport in Porous Media* **34** (1999), 249–267.
- [20] de Boer, R. & Ehlers, W.: *Theorie der Mehrkomponentenkontinua mit Anwendungen auf bodenmechanische Probleme*. Forschungsberichte aus dem Fachbereich Bauwesen, Heft 40, Universität-GH-Essen, Essen 1986.
- [21] Bourgeois, O.; Ford, M.; Diraison, M.; Le Carlier de Veslud, C.; Gerbault, M.; Pik, R.; Ruby, N. & Bonnet, S.: Separation of rifting and lithospheric folding signatures in the NW-Alpine foreland. *International Journal of Earth Sciences* **96** (2007), 1003–1031.
- [22] Bowen, R. M.: Theory of mixtures. In Eringen, A. C. (ed.): *Continuum Physics, Vol. 3*. Academic Press, New York 1976, pp. 1–127.
- [23] Bowen, R. M.: Incompressible porous media models by use of the theory of mixtures. *International Journal of Engineering Science* **18** (1980), 1129–1148.
- [24] Bowen, R. M.: Compressible porous media models by use of the theory of mixtures. *International Journal of Engineering Science* **20** (1982), 697–735.
- [25] Brooks, A. N. & Hughes, T. J.: Streamline upwind/Petrov-Galerkin formulations for convection dominated flows with particular emphasis on the incompressible Navier-Stokes equations. *Computer Methods in Applied Mechanics and Engineering* **32** (1982), 199–259.

- [26] Brun, J.; Wenzel, F. & ECORS-DEKORP team: Crustal-scale structure of the southern Rhinegraben from ECORS-DEKORP seismic reflection data. *Geology* **19** (1991), 758–762.
- [27] Chandrasekharam, D. & Bundschuh, J.: *Low-enthalpy geothermal resources for power generation*. CRC Press, Leiden 2008.
- [28] Cheng, P. & Lau, K.: Numerical modelling of Hawaiian geothermal resources. *Geothermics* **2** (1973), 90–93.
- [29] Coleman, B. D. & Noll, W.: The thermodynamics of elastic materials with heat conduction and viscosity. *Archive of Rational Mechanics and Analysis* **13** (1963), 167–178.
- [30] Dezayes, C.; Genter, A.; Homeier, G.; Degouy, M. & Stein, G.: *Geological Study of GPK3 HFR borehole (Soulz-sous-Forêts, France)*. BRGM/RP-52311-FR, Orléans 2003.
- [31] Donea, J.: A Taylor–Galerkin method for convective transport problems. *International Journal for Numerical Methods in Engineering* **20** (1984), 101–119.
- [32] Donea, J. & Huerta, A.: *Finite Element Methods for Flow Problems*. John Wiley & Sons, Chichester 2003.
- [33] Doonechaly, N. G.; Rahman, S. S. & Kotousov, A.: A new approach to hydraulic stimulation of geothermal reservoirs by roughness induced fracture opening. In Bunger, A. P.; McLennan, J. & Jeffrey, R. (eds.): *Effective and Sustainable Hydraulic Fracturing*. InTech, Rijeka 2013, pp. 571–590.
- [34] Dorbath, L.; Cuenot, N.; Genter, A. & Frogneux, M.: Seismic response of the fractured and faulted granite of Soultz-sous-Forêts (France) to 5 km deep massive water injections. *Geophysical Journal International* **177** (2009), 653–675.
- [35] Douglas, J. & Russell, T. F.: Numerical methods for convection-dominated diffusion problems based on combining the method of characteristics with finite element or finite difference procedures. *SIAM Journal on Numerical Analysis* **19** (1982), 871–885.
- [36] Durst, P. & Vuataz, F.-D.: Geochemical modelling of the Soultz-sous-Forêts hot dry rock system. Brine-rock interactions in a deep hot fractured granite reservoir. In *Proceedings, Twenty-Sixth Workshop on Geothermal Reservoir Engineering, Stanford University, Stanford* 2001, pp. 11–20.
- [37] Dziewonski, A. M. & Anderson, D. L.: Preliminary reference earth model. *Physics of the Earth and Planetary Interiors* **25** (1981), 297–356.
- [38] Ehlers, W.: Constitutive equations for granular materials in geomechanical context. In Hutter, K. (ed.): *Continuum Mechanics in Environmental Sciences and Geophysics*. Springer-Verlag, Wien 1993, pp. 313–402.

- [39] Ehlers, W.: *Vector and Tensor Calculus: An Introduction*. Lecture notes, Institute of Applied Mechanics, Chair of Continuum Mechanics, University of Stuttgart 1995–2015.
- [40] Ehlers, W.: Foundations of multiphase and porous materials. In Ehlers, W. & Bluhm, J. (eds.): *Porous Media: Theory, Experiments and Numerical Applications*. Springer-Verlag, Berlin 2002, pp. 3–86.
- [41] Ehlers, W.: Challenges of porous media models in geo- and biomechanical engineering including electro-chemically active polymers and gels. *International Journal of Advances in Engineering Sciences and Applied Mathematics* **1** (2009), 1–24.
- [42] Ehlers, W.: *Poröse Medien – ein kontinuumsmechanisches Modell auf der Basis der Mischungstheorie*. Nachdruck der Habilitationsschrift aus dem Jahre 1989 (Forschungsbericht aus dem Fachbereich Bauwesen der Universität-GH-Essen, Heft 47, Essen 1989), Report No. II-22 of the Institute of Applied Mechanics (CE), University of Stuttgart, Stuttgart 2012.
- [43] Ehlers, W.: Porous media in the light of history. In Stein, E. (ed.): *The History of Theoretical, Material and Computational Mechanics - Mathematics Meets Mechanics and Engineering*. Springer-Verlag, Berlin 2014, pp. 211–227.
- [44] Ehlers, W. & Ellsiepen, P.: PANDAS: Ein FE-System zur Simulation von Sonderproblemen der Bodenmechanik. In Wriggers, P.; Meißner, U.; Stein, E. & Wunderlich, W. (eds.): *Finite Elemente in der Baupraxis - FEM'98*. Ernst & Sohn, Berlin 1998, pp. 391–400.
- [45] Ehlers, W. & Ellsiepen, P.: Theoretical and numerical methods in environmental continuum mechanics based on the Theory of Porous Media. In Schrefler, B. A. (ed.): *Environmental Geomechanics*. Springer-Verlag, Wien 2001, pp. 1–81.
- [46] Ehlers, W.; Ellsiepen, P.; Blome, P.; Mahnkopf, D. & Markert, B.: *Theoretische und numerische Studien zur Lösung von Rand- und Anfangswertproblemen in der Theorie Poröser Medien, Abschlußbericht zum DFG-Forschungsvorhaben Eh 107/6-2*. Report No. 99-II-1 of the Institute of Applied Mechanics (CE), University of Stuttgart, Stuttgart 1999.
- [47] Ehlers, W. & Häberle, K.: Interfacial mass transfer during gas–liquid phase change in deformable porous media with heat transfer. *Transport in Porous Media* **114** (2016), 525–556.
- [48] Ehlers, W.; Zinatbakhsh, S. & Markert, B.: Stability analysis of finite difference schemes revisited: A study of decoupled solution strategies for coupled multifield problems. *International Journal for Numerical Methods in Engineering* **94** (2013), 758–786.
- [49] Eipper, G.: *Theorie und Numerik finiter elastischer Deformationen in fluidgesättigten porösen Festkörpern*. Dissertation Thesis, Report No. II-1 of the Institute of Applied Mechanics (CE), University of Stuttgart, Stuttgart 1998.

- [50] Ellsiepen, P.: *Zeit- und ortsadaptive Verfahren angewandt auf Mehrphasenprobleme poröser Medien*. Dissertation Thesis, Report No. II-3 of the Institute of Applied Mechanics (CE), University of Stuttgart, Stuttgart 1999.
- [51] ENGINE Coordination Action: *Best Practice Handbook for the development of Unconventional Geothermal Resources with a focus on Enhanced Geothermal Systems. Collection Actes*. BRGM Editions, Orléans 2008.
- [52] Evans, K. F.: Permeability creation and damage due to massive fluid injections into granite at 3.5 km at Soultz: 2. critical stress and fracture strength. *Journal of Geophysical Research: Solid Earth* **110** (2005), B04204.
- [53] Evans, K. F.; Genter, A. & Sausse, J.: Permeability creation and damage due to massive fluid injections into granite at 3.5 km at Soultz: 1. borehole observations. *Journal of Geophysical Research: Solid Earth* **110** (2005), B04203.
- [54] Evans, K. F.; Zappone, A.; Kraft, T.; Deichmann, N. & Moia, F.: A survey of the induced seismic responses to fluid injection in geothermal and CO₂ reservoirs in Europe. *Geothermics* **41** (2012), 30–54.
- [55] Finger, J. & Blankenship, D.: *Sandia Report - Handbook of Best Practices for Geothermal Drilling*. Sandia National Laboratories, Albuquerque 2010.
- [56] Fink, D. & Ehlers, W.: Application and modification of the POD method and the POD-DEIM for model reduction in porous-media simulations. *Proceedings in Applied Mathematics and Mechanics* **15** (2015), 385–386.
- [57] Franca, L. P. & Farhat, C.: Bubble functions prompt unusual stabilized finite element methods. *Computer Methods in Applied Mechanics and Engineering* **123** (1995), 299–308.
- [58] Fridleifsson, I. B.; Bertani, R.; Huenges, E.; Lund, J. W.; Ragnarsson, A. & Rybach, L.: The possible role and contribution of geothermal energy to the mitigation of climate change. In Hohmeyer, O. & Trittin, T. (eds.): *IPCC Scoping Meeting on Renewable Energy Sources*, Lübeck 2008, pp. 59–80.
- [59] Garnish, J.; Baria, R.; Baumgärtner, J. & Gérard, A.: The European hot dry rock programme 1994-95. *Geothermal Resources Council Transactions* **18** (1994), 431–438.
- [60] Genter, A.: *EGS Pilot Plant - Publishable Final Activity Report*. GEIE Exploitation Minière de la Chaleur, Kutzenhausen 2009.
- [61] Genter, A.; Cuenot, N.; Goerke, X.; Bernd, M.; Sanjuan, B. & Scheiber, J.: Status of the Soultz geothermal project during exploitation between 2010 and 2012. In *Proceedings, Thirty-Seventh Workshop on Geothermal Reservoir Engineering, Stanford University, Stanford 2012*, SGP-TR-194.

- [62] Genter, A.; Evans, K.; Cuenot, N.; Fritsch, D. & Sanjuan, B.: The Soultz geothermal adventure: 20 years of research and exploration of deep crystalline fractured rocks for EGS development. *Comptes Rendus Geoscience* **342** (2010), 502–516.
- [63] Genter, A. & Traineau, H.: Borehole EPS-1, Alsace, France: preliminary geological results from granite core analyses for hot dry rock research. *Scientific Drilling* **3** (1992), 205–214.
- [64] Genter, A. & Traineau, H.: Analysis of macroscopic fractures in granite in the HDR geothermal well EPS-1, Soultz-sous-Forêts, France. *Journal of Volcanology and Geothermal Research* **72** (1996), 121–141.
- [65] Ghadiani, S. R.: *A multiphasic continuum mechanical model for design investigations of an effusion-cooled rocket thrust chamber*. Dissertation Thesis, Report No. II-13 of the Institute of Applied Mechanics (CE), University of Stuttgart, Stuttgart 2005.
- [66] Giardini, D.: Geothermal quake risks must be faced. *Nature* **462** (2009), 848–849.
- [67] Graf, T.: *Multiphasic flow processes in deformable porous media under consideration of fluid phase transitions*. Dissertation Thesis, Report No. II-17 of the Institute of Applied Mechanics (CE), University of Stuttgart, Stuttgart 2008.
- [68] Gresho, P. M. & Lee, R. L.: Don't suppress the wiggles - they're telling you something! *Computers & Fluids* **9** (1981), 223–253.
- [69] Gérard, A.; Genter, A.; Kohl, T.; Lutz, P.; Rose, P. & Rummel, F.: The deep EGS (enhanced geothermal system) project at Soultz-sous-Forêts (Alsace, France). *Geothermics* **35** (2006), 473–483.
- [70] Gérard, A. & Kappelmeyer, O.: The Soultz-sous-Forêts project. *Geothermics* **16** (1987), 393–399.
- [71] Häberle, K. & Ehlers, W.: Thermodynamically consistent description of mass transfer in porous media by a singular surface. *Proceedings in Applied Mathematics and Mechanics* **15** (2015), 391–392.
- [72] Haenel, R.; Rybach, L. & Stegena, L.: Fundamentals of geothermics. In Haenel, R.; Rybach, L. & Stegena, L. (eds.): *Handbook of Terrestrial Heat-Flow Density Determination*. Kluwer Academic Publishers, Dordrecht 1988, pp. 9–57.
- [73] Heider, Y.: *Saturated porous media dynamics with application to earthquake engineering*. Dissertation Thesis, Report No. II-25 of the Institute of Applied Mechanics (CE), University of Stuttgart, Stuttgart 2012.
- [74] Hooijkaas, G. R.; Genter, A. & Dezayes, C.: Deep-seated geology of the granite intrusions at the Soultz EGS site based on data from 5 km-deep boreholes. *Geothermics* **35** (2006), 484–506.

- [75] Hughes, T. J. R.: Multiscale phenomena: Green's functions, the Dirichlet-to-Neumann formulation, subgrid scale models, bubbles and the origins of stabilized methods. *Computer Methods in Applied Mechanics and Engineering* **127** (1995), 387–401.
- [76] Hughes, T. J. R.: *The Finite Element Method: Linear Static and Dynamic Finite Element Analysis*. Dover Publications, Mineola 2000.
- [77] Hughes, T. J. R.; Franca, L. P. & Hulbert, G. M.: A new finite element formulation for computational fluid dynamics: VIII. the Galerkin/least-squares method for advective-diffusive equations. *Computer Methods in Applied Mechanics and Engineering* **73** (1989), 173–189.
- [78] Ilinca, F.; Héту, J. F. & Pelletier, D.: On stabilized finite element formulations for incompressible advective–diffusive transport and fluid flow problems. *Computer Methods in Applied Mechanics and Engineering* **188** (2000), 235–255.
- [79] International Energy Agency: *Key World Energy Statistics 2013*. PW, Paris 2013.
- [80] John, V. & Knobloch, P.: On spurious oscillations at layers diminishing (SOLD) methods for convection-diffusion equations: Part I - A review. *Computer Methods in Applied Mechanics and Engineering* **196** (2007), 2197–2215.
- [81] Jung, R.: EGS - goodbye or back to the future 95, Effective and sustainable hydraulic fracturing. In Bungler, A. P.; McLennan, J. & Jeffrey, R. (eds.): *Effective and Sustainable Hydraulic Fracturing*. InTech, Rijeka 2013, pp. 95–122.
- [82] Jung, R.; Richard, J. W.; Nicholls, J.; Bertozzi, A. & Heinemann, B.: Evaluation of hydraulic tests at Soultz-sous-Forêts, European HDR-site. In *Proceedings, World Geothermal Congress*, Florence 1995, pp. 2671–2676.
- [83] Kennett, B. L. N. & Engdahl, E. R.: Traveltimes for global earthquake location and phase identification. *Geophysical Journal International* **105** (1991), 429–465.
- [84] Lewis, R. W.; Majorana, C. E. & Schrefler, B. A.: A coupled finite element model for the consolidation of nonisothermal elastoplastic porous media. *Transport in Porous Media* **1** (1986), 155–178.
- [85] Lu, S. & Pister, K.: Decomposition of deformation and representation of the free energy function for isotropic thermoelastic solids. *International Journal of Solids and Structures* **11** (1975), 927–934, ISSN 0020-7683.
- [86] Luo, C. & Ehlers, W.: Hydraulic fracturing based on the theory of porous media. *Proceedings in Applied Mathematics and Mechanics* **15** (2015), 401–402.
- [87] Majer, E. L.; Baria, R.; Stark, M.; Oates, S.; Bommer, J.; Smith, B. & Asanuma, H.: Induced seismicity associated with enhanced geothermal systems. *Geothermics* **36** (2007), 185–222.

- [88] Markert, B.: *Porous Media Viscoelasticity with Application to Polymeric Foams*. Dissertation Thesis, Report No. II-12 of the Institute of Applied Mechanics (CE), University of Stuttgart, Stuttgart 2005.
- [89] Markert, B.: A constitutive approach to 3-d nonlinear fluid flow through finite deformable porous continua. *Transport in Porous Media* **70** (2007), 427–450.
- [90] Mercer Jr., J. & Pinder, G.: Galerkin finite-element simulation of a geothermal reservoir. *Geothermics* **2** (1973), 81–89.
- [91] NACE MR0175/ISO 15156: *International standard: Petroleum and natural gas industries - Materials for use in H₂S-containing Environments in oil and gas production*. International Organization for Standardization (ISO), Geneva; NACE International, Houston 2001.
- [92] Nami, P.; Schellschmidt, R.; Schindler, M. & Tischner, T.: Chemical stimulation operations for reservoir development of the deep crystalline HDR/EGS system at Soultz-sous-Forêts (France). In *Proceedings, Thirty-Second workshop on Geothermal Engineering, Stanford University, Stanford* 2008, SGP-TR-185.
- [93] Nowak, W.; de Barros, F. P. J. & Rubin, Y.: Bayesian geostatistical design: Task-driven optimal site investigation when the geostatistical model is uncertain. *Water Resources Research* **46** (2010), DOI: 10.1029/2009WR008312.
- [94] Oñate, E. & Manzan, M.: Stabilization techniques for finite element analysis of convection-diffusion problems. In Comini, G. & Sunden, B. (eds.): *Computational Analysis of Heat Transfer*. WIT Press, Southampton 2000.
- [95] O’Sullivan, M. J.; Pruess, K. & Lippmann, M. J.: State of the art of geothermal reservoir simulation. *Geothermics* **30** (2001), 395–429.
- [96] Pironneau, O.: On the transport-diffusion algorithm and its applications to the Navier-Stokes equations. *Numerische Mathematik* **38** (1982), 309–332.
- [97] Portier, S.; Vuataz, F.-D.; Nami, P.; Sanjuan, B. & Gérard, A.: Chemical stimulation techniques for geothermal wells: experiments on the three-well EGS system at Soultz-sous-Forêts, France. *Geothermics* **38** (2009), 349–359.
- [98] Pribnow, D. & Schellschmidt, R.: Thermal tracking of upper crustal fluid flow in the Rhine graben. *Geophysical Research Letters* **27** (2000), 1957–1960.
- [99] Pruess, K.: *Mathematical modeling of fluid flow and heat transfer in geothermal systems - an introduction in five lectures*. United Nations University, Geothermal Training Programme, Reykjavik 2002.
- [100] Ravier, G.; Graff, J.-J. & Villadangos, G.: Operating a lineshaft production pump in a small pump chamber under highly aggressive geothermal fluid conditions: Results from the Soultz EGS site. In *Proceedings, World Geothermal Congress, Melbourne* 2015.

- [101] Refsgaard, J. C.; Christensen, S.; Sonnenborg, T. O.; Seifert, D.; Højberg, A. L. & Troldborg, L.: Review of strategies for handling geological uncertainty in ground-water flow and transport modeling. *Advances in Water Resources* **36** (2012), 36 – 50.
- [102] Rempler, H.-U.: *Damage in Multi-Phasic Materials Computed with the Extended Finite-Element Method*. Dissertation Thesis, Report No. II-23 of the Institute of Applied Mechanics (CE), University of Stuttgart, Stuttgart 2012.
- [103] Sanjuan, B.; Pinault, J.-L.; Rose, P.; Gérard, A.; Brach, M.; Braibant, G.; Crouzet, C.; Foucher, J.-C.; Gautier, A. & Touzelet, S.: Geochemical fluid characteristics and main achievements about tracer tests at Soultz-sous-Forêts (France). In *EHDRA Scientific Conference*, Soultz-sous-Forêts 2006.
- [104] Sanjuan, B.; Pinault, J.-L.; Rose, P.; Gérard, A.; Brach, M.; Braibant, G.; Crouzet, C.; Foucher, J.-C.; Gautier, A. & Touzelet, S.: Tracer testing of the geothermal heat exchanger at Soultz-sous-Forêts (France) between 2000 and 2005. *Geothermics* **35** (2006), 622–653.
- [105] Schenke, M.: *Development of an interface between Abaqus and Pandas*. Master Thesis, Report No. 08-II-12 of the Institute of Applied Mechanics (CE), University of Stuttgart, Stuttgart 2008.
- [106] Schenke, M. & Ehlers, W.: On the analysis of soils using an Abaqus-Pandas interface. *Proceedings in Applied Mathematics and Mechanics* **11** (2011), 431–432.
- [107] Simo, J. & Pister, K.: Remarks on rate constitutive equations for finite deformation problems: computational implications. *Computer Methods in Applied Mechanics and Engineering* **46** (1984), 201–215.
- [108] Smith, M.; Aamodt, R. L.; Potter, R. M. & Brown, D.: *Man-made geothermal reservoirs*. Report of the Los Alamos Scientific Laboratory, Los Alamos 1975.
- [109] Surma, F. & Géraud, Y.: Porosity and thermal conductivity of the Soultz-sous-Forêts granite. *Pure and Applied Geophysics* **160** (2003), 1125–1136.
- [110] Terzaghi, K.: Die Berechnung der Durchlässigkeitsziffer des Tonen aus dem Verlauf der hydrodynamischen Spannungserscheinungen. *Sitzungsberichte der Akademie der Wissenschaften in Wien, Mathematisch-Naturwissenschaftliche Klasse, Abteilung IIa* **132** (1923), 125–138.
- [111] Tischner, T.; Pfender, M. & Teza, D.: *Hot Dry Rock Projekt Soultz: Erste Phase der Erstellung einer wissenschaftlichen Pilotanlage - Abschlussbericht zum Vorhaben 0327097*. Bundesministerium für Umwelt, Naturschutz und Reaktorsicherheit, Berlin 2006.
- [112] Tischner, T.; Schindler, M.; Jung, R. & Nami, P.: HDR project Soultz: Hydraulic and seismic observations during stimulation of the 3 deep wells by massive water injections. In *Proceedings, Thirty-Second workshop on Geothermal Engineering, Stanford University*, Stanford 2007, SGP-TR-183.

- [113] Truesdell, C.: *Rational Thermodynamics*. 2nd edn. Springer-Verlag, New York 1984.
- [114] Truesdell, C. & Noll, W.: The nonlinear field theories of mechanics. In Flügge, S. (ed.): *Handbuch der Physik, Vol. III/3*. Springer-Verlag, Berlin 1965.
- [115] Truesdell, C. & Toupin, R. A.: The classical field theories. In Flügge, S. (ed.): *Handbuch der Physik, Vol. III/1*. Springer-Verlag, Berlin 1960, pp. 226–902.
- [116] Truesdell, C. A.: Sulle basi della termomeccanica. *Rendiconti Lincei* **22** (1957), 33–38.
- [117] Valley, B. C.: *The relation between natural fracturing and stress heterogeneities in deep-seated crystalline rocks at Soultz-sous-Forêts (France)*. Dissertation Thesis, ETH Number 17385, Institute of Geology, Swiss Federal Institute of Technology (ETH) Zurich 2007.
- [118] Wagner, A.: *Extended Modelling of the Multiphasic Human Brain Tissue with Application to Drug-Infusion Processes*. Dissertation Thesis, Report No. II-27 of the Institute of Applied Mechanics (CE), University of Stuttgart, Stuttgart 2014.
- [119] Weidler, R.; Gérard, A.; Baria, R.; Baumgärtner, J. & Jung, R.: Hydraulic and micro-seismic results of a massive stimulation test at 5 km depth at the European hot-dry-rock test site Soultz, France. In *Proceedings, Twenty-Seventh Workshop on Geothermal Engineering, Stanford University*, Stanford 2002, SGP-TR-171.
- [120] Williamson, K.: Reservoir simulation of the geysers geothermal field. In *Proceedings, Fifteenth Workshop on Geothermal Reservoir Engineering, Stanford University*, Stanford 1990, pp. 113–123.
- [121] Ziegler, P. A.: European cenozoic rift system. *Tectonophysics* **208** (1992), 91–111.
- [122] Zienkiewicz, O. C.; Taylor, R. L. & Nithiarasu, P.: *The Finite Element Method for Fluid Dynamics*. Butterworth Heinemann, Oxford 2005, sixth edn.
- [123] Zienkiewicz, O. C.; Taylor, R. L. & Zhu, J. Z.: *The Finite Element Method: Its Basis and Fundamentals*. Butterworth Heinemann, Oxford 2005, sixth edn.
- [124] Zinatbakhsh, S.: *Coupled Problems in the Mechanics of Multi-Physics and Multi-Phase Materials*. Dissertation Thesis, Report No. II-30 of the Institute of Applied Mechanics (CE), University of Stuttgart, Stuttgart 2015.
- [125] Zinatbakhsh, S.; Koch, D.; Park, K. C.; Markert, B. & Ehlers, W.: Partitioned formulation and stability analysis of a fluid interacting with a saturated porous medium by localised lagrange multipliers. *International Journal for Numerical Methods in Engineering* (2015), DOI: 10.1002/nme.5148.

List of Figures

2.1	The inner structure of the Earth.	10
2.2	Schematic illustration of a mechanical heat pump.	11
2.3	The most common configurations of near-surface ground heat exchanger: a geothermal collector (left), a geothermal probe (middle) and a GRD (right).	12
2.4	Functional principle of an EGS power plant with <i>A</i> : impermeable rock, <i>B</i> : geothermal reservoir, <i>C</i> : IW, <i>D</i> : PW, <i>E</i> : heat exchanger, <i>F</i> : turbine hall, <i>G</i> : cooling tower, <i>H</i> : output for district heating, <i>I</i> : electricity output, <i>J</i> : water reservoir.	14
2.5	Map of the Upper Rhine Graben, Central Europe.	17
3.1	A REV of the real structure, an exemplary microscale model with two phases in separated volumes and a homogenised model of superimposed continua.	24
3.2	Motion of a binary aggregate.	25
4.1	Pressure–temperature phase diagram of water.	36
5.1	Extended hexahedral Taylor-Hood element.	54
5.2	Analytical solution of a 1-d convection-diffusion equation considering different convection-diffusion ratios.	57
5.3	Discrete solution of a 1-d convection-diffusion equation for different numbers of elements with a convection-diffusion relation $v/d = 50$	58
6.1	Example 1: Quasi 1-d IBVP.	67
6.2	Example 1: The Fluid temperature of the quasi 1-d IBVP with 10, 20, 32 and 40 elements.	68
6.3	Example 1: Comparison between the fluid temperature obtained by the stabilised solution using 10, 20 and 32 elements and the non-stabilised reference solution using 40 elements.	68
6.4	Example 2: IBVP, here illustrated with a mesh consisting of 376 elements.	69
6.5	Example 2: Fluid temperature distribution after $1.5 \cdot 10^7$ seconds obtained from the non-stabilised simulation using 6 256 elements. [-1mm]	69
6.6	Example 2: Comparison of the fluid-temperature distribution after $1.5 \cdot 10^7$ seconds of (a) the non-stabilised calculation and the stabilised calculations with an (b) IAD, (c) SU and (d) SUPG stabilisation approach using 376 cube-shaped elements.	70

6.7	Example 2: Fluid-temperature profile between the points <i>A</i> and <i>B</i>	70
6.8	Example 3: IBVP.	71
6.9	Example 3: Fluid-temperature distribution after $2 \cdot 10^6$ seconds for a calculation with 36 elements (a) without stabilisation, stabilised via (b) IAD, (c) SU, (d) SUPG, and (e) a non-stabilised overkill solution using 3600 elements.	71
6.10	Example 3: Fluid-temperature profile and deviation between the stabilised and non-stabilised calculations with the coarse mesh (36 elements) and the fine mesh (3600 elements) overkill solution after $2 \cdot 10^6$ seconds between the points <i>A</i> and <i>B</i>	71
6.11	Geometry and the boundary numbering of the IBVP representing the EGS.	73
6.12	The resulting outward oriented part of the seepage velocity at the PW depending on the depth for different permeabilities.	76
6.13	Evolution of the maximum and the minimum Péclet number of all nodes at every time step of Step 3.	77
6.14	Fluid temperature at 4750 m TVD along the symmetry plane and in the vicinity of the PW with element accurate resolution. [1mm]	78
6.15	Fluid-temperature distribution at 4750 m TVD.	79
6.16	Fluid-temperature distribution at the plane of symmetry.	79
6.17	Evolution of the fluid temperature at the points <i>A</i> , <i>B</i> and <i>C</i>	80
6.18	Evolution of the produced thermal gross power. [2mm]	80
6.19	Fluid temperature and temperature difference between solid and fluid at point <i>D</i> . [-2mm]	81
6.20	Magnitude of heat conduction within the constituents.	82
6.21	Vertical solid displacement of the top at point <i>E</i>	83

List of Tables

2.1	Chronological overview of the chemical stimulation at Soultz (cf. Nami <i>et al.</i> [92]). Herein, OCA consists of 5–10 % $C_6H_8O_7$ + 0.1–1 % HF + 0.5–1.5 % HBF_4 + 1–5 % NH_4Cl	21
6.1	Material parameters and initial values.	66
6.2	Example 1: Péclet numbers after $2 \cdot 10^7$ seconds and the required calculation time for different numbers of elements.	68
6.3	Step 1: Boundary conditions for the mass balance of the fluid (MF), the three directions of the momentum balance of the mixture (MM_i), as well as the energy balances of the fluid (EF) and the solid (ES).	74
6.4	Step 2: Boundary conditions for the mass balance of the fluid (MF), the three directions of the momentum balance of the mixture (MM_i), as well as the energy balances of the fluid (EF) and the solid (ES).	75
6.5	Step 3: Boundary conditions for the mass balance of the fluid (MF), the three directions of the momentum balance of the mixture (MM_i), as well as the energy balances of the fluid (EF) and the solid (ES).	75

Curriculum Vitae

Personal data:

Name: David Koch
Date of birth: August 27, 1982
Place of birth: Göppingen, Germany
Parents: Gudrun and Michael Koch
Siblings: Isabell Rößiger, Anne Koch, Bertram Koch, Simon Koch
Marital status: married with Jessica Koch
Children: Jana, Felix and Lisa Koch

Education:

09/1989 – 07/2001 elementary/secondary/high school
“Freie Waldorfschule Engelberg”
09/2001 – 06/2003 high school “Firstwaldgymnasium Mössingen”
06/2003 degree: “Allgemeine Hochschulreife” (high school diploma)
09/2003 – 01/2009 studies in civil engineering
at the University of Stuttgart
major subject: “Modellierungs- und Simulationenmethoden”
01/2009 degree: “Diplom-Ingenieur (Dipl.-Ing.) Bauingenieurwesen”

Professional occupation:

03/2009 – 06/2015 teaching assistant and research associate at the
Institute of Applied Mechanics (Civil Engineering) at the
University of Stuttgart
since 12/2015 computational engineer at DYNAmore GmbH, Stuttgart

Presently published contributions in this report series

- II-1 Gernot Eipper: *Theorie und Numerik finiter elastischer Deformationen in fluid-gesättigten porösen Festkörpern*, 1998.
- II-2 Wolfram Volk: *Untersuchung des Lokalisierungsverhaltens mikropolarer poröser Medien mit Hilfe der Cosserat-Theorie*, 1999.
- II-3 Peter Ellsiepen: *Zeit- und ortsadaptive Verfahren angewandt auf Mehrphasenprobleme poröser Medien*, 1999.
- II-4 Stefan Diebels: *Mikropolare Zweiphasenmodelle: Formulierung auf der Basis der Theorie Poröser Medien*, 2000.
- II-5 Dirk Mahnkopf: *Lokalisierung fluidgesättigter poröser Festkörper bei finiten elasto-plastischen Deformationen*, 2000.
- II-6 Heiner Müllerschön: *Spannungs-Verformungsverhalten granularer Materialien am Beispiel von Berliner Sand*, 2000.
- II-7 Stefan Diebels (Ed.): *Zur Beschreibung komplexen Materialverhaltens: Beiträge anlässlich des 50. Geburtstages von Herrn Prof. Dr.-Ing. Wolfgang Ehlers*, 2001.
- II-8 Jack Widjajakusuma: *Quantitative Prediction of Effective Material Parameters of Heterogeneous Materials*, 2002.
- II-9 Alexander Droste: *Beschreibung und Anwendung eines elastisch-plastischen Materialmodells mit Schädigung für hochporöse Metallschäume*, 2002.
- II-10 Peter Blome: *Ein Mehrphasen-Stoffmodell für Böden mit Übergang auf Interface-Gesetze*, 2003.
- II-11 Martin Ammann: *Parallel Finite Element Simulations of Localization Phenomena in Porous Media*, 2005.
- II-12 Bernd Markert: *Porous Media Viscoelasticity with Application to Polymeric Foams*, 2005.
- II-13 Saeed Reza Ghadiani: *A Multiphasic Continuum Mechanical Model for Design Investigations of an Effusion-Cooled Rocket Thrust Chamber*, 2005.
- II-14 Wolfgang Ehlers & Bernd Markert (Eds.): *Proceedings of the 1st GAMM Seminar on Continuum Biomechanics*, 2005.
- II-15 Bernd Scholz: *Application of a Micropolar Model to the Localization Phenomena in Granular Materials: General Model, Sensitivity Analysis and Parameter Optimization*, 2007.

- II-16** Wolfgang Ehlers & Nils Karajan (Eds.): *Proceedings of the 2nd GAMM Seminar on Continuum Biomechanics*, 2007.
- II-17** Tobias Graf: *Multiphasic Flow Processes in Deformable Porous Media under Consideration of Fluid Phase Transitions*, 2008.
- II-18** Ayhan Acartürk: *Simulation of Charged Hydrated Porous Materials*, 2009.
- II-19** Nils Karajan: *An Extended Biphasic Description of the Inhomogeneous and Anisotropic Intervertebral Disc*, 2009.
- II-20** Bernd Markert: *Weak or Strong – On Coupled Problems In Continuum Mechanics*, 2010.
- II-21** Wolfgang Ehlers & Bernd Markert (Eds.): *Proceedings of the 3rd GAMM Seminar on Continuum Biomechanics*, 2012.
- II-22** Wolfgang Ehlers: *Poröse Medien – ein kontinuumsmechanisches Modell auf der Basis der Mischungstheorie*, 2012. Nachdruck der Habilitationsschrift aus dem Jahr 1989 (Forschungsberichte aus dem Fachbereich Bauwesen der Universität-GH-Essen 47, Essen 1989).
- II-23** Hans-Uwe Rempler: *Damage in multi-phasic Materials Computed with the Extended Finite-Element Method*, 2012.
- II-24** Irina Komarova: *Carbon-Dioxide Storage in the Subsurface: A Fully Coupled Analysis of Transport Phenomena and Solid Deformation*, 2012.
- II-25** Yousef Heider: *Saturated Porous Media Dynamics with Application to Earthquake Engineering*, 2012.
- II-26** Okan Avci: *Coupled Deformation and Flow Processes of Partial Saturated Soil: Experiments, Model Validation and Numerical Investigations*, 2013.
- II-27** Arndt Wagner: *Extended Modelling of the Multiphasic Human Brain Tissue with Application to Drug-Infusion Processes*, 2014.
- II-28** Joffrey Mabuma: *Multi-Field Modelling and Simulation of the Human Hip Joint*, 2014.
- II-29** Robert Friedrich Krause: *Growth, Modelling and Remodelling of Biological Tissue*, 2014.
- II-30** Seyedmohammad Zinatbakhsh: *Coupled Problems in the Mechanics of Multi-Physics and Multi-Phase Materials*, 2015.
- II-31** David Koch: *Thermomechanical Modelling of Non-isothermal Porous Materials with Application to Enhanced Geothermal Systems*, 2016.